UNIVERSITÀ DEGLI STUDI DI PADOVA

Dipartimento di Fisica e Astronomia “Galileo Galilei”

Laurea Magistrale in Fisica

Dosimetric characterization of a new plastic scintillator and other detectors in standard and small field photon beams from a medical linear accelerator

Relatore interno

Prof.ssa Laura De Nardo

Relatore esterno

Dott.ssa Sonia Reccanello

Laureando

Gabriele Sattier

Anno Accademico 2024/2025

Contents

Introduction

Radiotherapy consists in the use of ionizing radiation beams of various nature (usually photons, electrons, or protons/heavy ions) to treat tumor diseases. That is achieved by killing tumor cells while sparing as much as possible the surrounding healthy tissues.

Focusing on photon beams, over the years, their clinical production shifted from the use of γ sources, i.e. ^{60}Co, to the usage of medical Linear Accelerators (LINAC) that generates an electron beam of different energies, then producing a photon beam through bremsstrahlung emission. Recently, research has advanced considerably regarding the tools and techniques adopted in radiotherapy. For instance, it is now possible to account for irregular shapes of a tumor with the help of a Multi-Leaf Collimator (MLC), and furthermore to modulate the beam intensity to perform advanced treatment techniques like Intensity Modulated Radiation Therapy (IMRT) or Volumetric Modulated Arc Therapy (VMAT). Those techniques are enabled also thanks to the optimization of algorithms used in Treatment Planning Systems (TPS) which permit to precisely determine the dose delivered to each irradiated voxel and thus to optimize the beam intensity dispensed during treatments.

To be ready for clinical use, it is then necessary to construct a model of the LINAC machine to be uploaded into the TPS, so that the software can simulate the beam delivery, allowing the algorithms previously cited to work properly. This is part of a complex process called commissioning, which encompasses a series of dosimetric measures to collect enough data to characterize the LINAC behaviour during ordinary therapeutic activity [1]. Those measures must be taken following the international regulations written by the International Atomic Energy Agency (IAEA), particularly the IAEA TRS-398 Code of Practice [2]. The main measures to be collected are some sets about the Percentage Depth Dose (PDD) and the Off Axis Ratio (OAR) distributions, followed by Field Output Factors (FOF) values.

These measurements can be performed with different types of detectors, such as solid-state detectors, scintillators, ionization chambers, etc. Different sets of measurements must be collected for all the allowed field sizes, which usually vary from large field dimensions (tenths of centimeters per side) to the so called small field sizes (some millimeters). Small fields are characterized by some issues that larger fields dimensions don't show [3] [4]. For this reason, other international protocols and instructions, listed in the IAEA TRS-483 Code of Practice [5], report specific procedures and correction factors [6] [7] [8] for dealing with small fields.

The main goal of this thesis work is to evaluate the performances of different detectors during the commissioning of the VERSA HD LINAC [1] recently installed at the Radiotherapy Department of AULSS 3 "Ospedale dell'Angelo" located in Mestre (Venice) by using two different photon energies (6 MV WFF and 6 MV FFF)[1]. To this purpose, PDDs, OARs, and FOFs have been subject of comparison with suitable detectors such as PTW microdiamond [9], IBA Razor diode, IBA EFD3G unshielded-diode [10] and the new Blue Physics Plastic Scintillator Detector (BP-PSD) [11] [12]. In particular, the features and properties of the BP-PSD were deeply investigated, as well as challenges and issues about dosimetry in small fields.

The thesis is structured in the following way:

Chapter 1 serves as an introduction to the radiotherapy and dosimetry fields, reviewing the preliminary quantities and concepts that will be encountered along the subsequent chapters.

In **Chapter 2** the measurement apparatus is described, as well as the acquisition procedures adopted.

Chapter 3 contains the data analysis, encompassing the raw data analysis procedures, the results comparisons and the discussion about the measurement uncertainties.

Finally, the Chapter *Discussion and Conclusions* provides some closing considerations about the obtained results.

---

[1] WFF: With Flattening Filter. FFF: Flattening Filter Free.

Chapter 1

Radiotherapy and dosimetry generalities

1.1 Radiotherapy

Radiotherapy is a type of treatment whose main goal is to treat tumor diseases by killing tumor cells using ionizing radiation of various nature, while trying to preserve as much as possible the surrounding healthy tissues.

There is a distinction between internal and external radiotherapy: the former consists in the application of radiation sources in the proximity or directly onto the tumoral mass, using sealed sources that will not enter the patient's metabolism (Brachytherapy) or radiopharmaceuticals that are delivered to the tumor area by nuclear medicine procedures; the latter is the conventional radiotherapy where the radiation source is positioned outside the patient's body and consists in Linear Accelerators (LINAC, for x-rays and electron sources) or Cyclotrons/Synchrotrons accelerators (for protons and heavy ions sources).

Below we will focus on external radiotherapy. In this case, radiation is collimated directly onto the tumoral mass so that cancerous cells lose the ability to grow and replicate, and the tumor starts to progressively reduce its dimensions.

Radiotherapy is a localized, noninvasive, and painless therapy that represents a valid alternative to traditional surgery when dealing with particular tumors that would be difficult to operate due to their location (for example, prostate or nasopharynx tumors).

There exist various subcategories of radiotherapy, depending on the clinical goals and the treated tumor [13]:

- Curative/radical therapy, which consists in completely removing the tumor.
- Pre-operatory neo-adjuvant therapy, which is executed before a tumor removal surgical intervention to reduce the tumoral mass dimension and make the operation easier to be performed.
- Post-operatory adjuvant therapy, which is prescribed after a tumor surgical removal to kill any leftover cancerous cell and to prevent future reformation.

- Intraoperative RadioTherapy (IORT), in which a radiation dose is administered during the surgical intervention for tumor removal.
- Palliative radiotherapy, to slow down tumor growth and relieve symptoms in the patient.
- Total body radiotherapy, in which the whole organism is irradiated to deal with tumors that affect the blood cells and the lymphatic system. Dead cells will successively be replaced with healthy ones by a bone marrow or stem cells transplant.
- Stereotactic radiotherapy, where elevated amounts of dose are administered on small-size tumors with high-precision techniques.

Over the years, the technology and the techniques exploited for radiotherapy have advanced a lot, in particular regarding the tools dedicated to external radiotherapy, such as the introduction of Multi-Leaf Collimators (MLC) for linear accelerators. These are collimators, made of several metal leaves that can slide orderly to obtain a specific collimated shape, now permits to perform advanced treatment techniques like Intensity Modulated Radiation Therapy (IMRT) and Volumetric Modulated Arc Therapy (VMAT).
IMRT consists in varying the dose distribution as a function of the tumor shape targeted so that the dose delivery can be more focused on the tumoral mass and it becomes easier to spare the surrounding healthy tissues. From here it is clear the importance of Computed Tomography (TC) or Magnetic Resonance Imaging (MRI) acquired for the patient prior to the creation of a treatment plan, to perform an analysis of the targeted tumor area and to determine the dose delivery model that fits it the best.
VMAT is a more advanced technique where the LINAC continuously rotates around the patient while simultaneously modifying the radiation field shape, the dispensed dose and the rotation velocity (the dose delivery distribution follows an arc, from which the name of *Arc Therapy*) so that the dose distribution is even more focused on the tumor area then in the IMRT case. In addition, VMAT is faster and thus minimizes the errors due to patient's movement, while improving patient's comfort in the meantime.

For the scope of this thesis, we will consider only external x-ray photon beams generated by linear accelerators. Actually, as previously mentioned, photon beams do not cover the whole range of possibilities regarding external beam radiotherapy, besides being the most widespread method over the world. Electron beams, proton beams and heavy ions beams represent valid alternatives when dealing with tumors of different natures, and each of them has its pros and cons.

Each particle choice presents its own advantages and disadvantages.

- X-rays γ beams are the most common and best fit for treating medium depths tumors in "standard" locations such as lungs, breasts, or prostate. They are a well known affirmed technique that have a relative moderate cost and good versatility, but they are not suited for very deep tumors or located in the proximity of delicate organs, since the dose tends to be delivered even in tissues before and after the target area.

- Electrons are another widespread option in various radiotherapy centers, and are used mainly to treat superficial tumors due to their low penetration capability. Examples of tumors for which electrons are exploited are skin carcinomas and superficial lymphomas (for instance, armpit lymphoma). They have the advantage to cause very little damage to deeper healthy tissues since they release most of their dose superficially, but on the other hand this also represents a disadvantage since they are not suited to treat deep tumors.

- Protons are a very efficient choice when dealing with deeper tumors or cancerous areas located in the proximity of delicate organs (such as the brain, the heart or the spinal cord) since their dose distribution (named Bragg distribution) is characterized by the Bragg peak, so the dose gets deposited in a narrow area. This facilitates to confine the treated zone, sparing all the tissues after the tumor and imparting a very low dose to the ones before it. This also allows to lower the risks of future side effects, making proton beams particularly suitable for children's and pediatric tumors. Their major drawbacks are the cost and the low availability, since they require more sophisticated accelerators and instrumentation.

- Heavy ions (mainly ^{12}C) are similar to protons since they deposit their dose following the Bragg distribution too, having an even narrower Bragg peak. Thus, they are a perfect choice for tumors located deep in the body or near sensible organs, such as those that develop at the base of the skull. Moreover, they are characterized by a particularly high biological efficiency, so they are really effective even against radioresistant tumors. Nevertheless, they are extremely expensive and there exist only few centers with the possibility to use them.

The following image represents the distribution of radiotherapy machines in the world, expressed as number per million people.

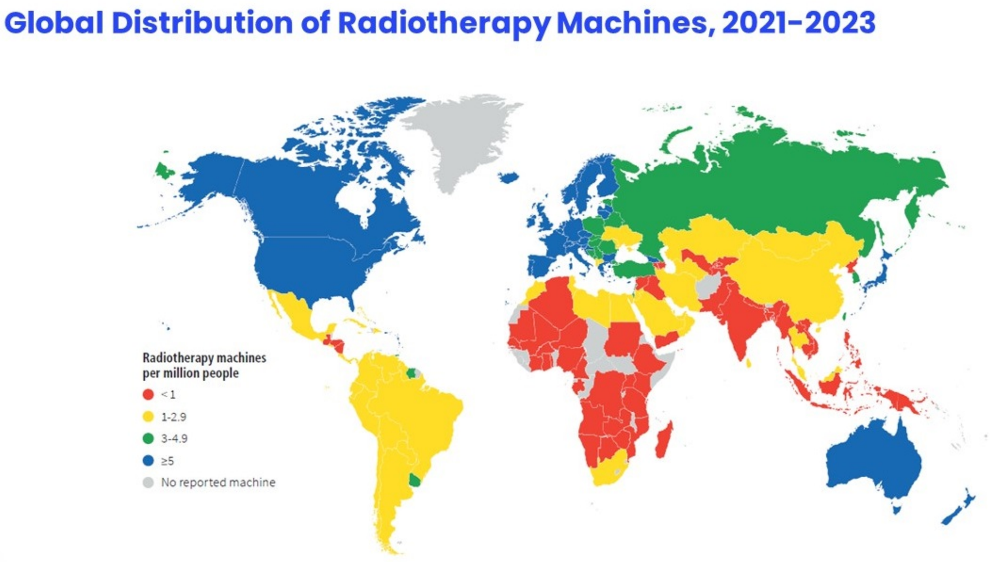

Figure 1.1: Radiotherapy machines distributions by IAEA data, expressed in number per million people.

In the next section, we will focus on the description of Linear Accelerators used for photon external beam radiotherapy, with a particular focus on the features of the new VERSA HD LINAC installed at the Radiotherapy Department of AULSS 3 "Ospedale dell'Angelo" in Mestre (Venice).

1.2 LINAC description

There exist three main types of accelerators that are used in radiotherapy centers: Linear Accelerators (LINAC), Synchrotron and Cyclotron accelerators. The last two are used for accelerating protons or heavy ions like the ^{12}C, and their functioning is based on a combination of electric fields to increase the energy of the particles and magnetic fields to bend their trajectories and keep them in circular motion. The main difference between the two types is that in Cyclotrons the bending magnetic field is fixed and the radius of the particles orbit increases gradually by the effect of the electric field, while in Synchrotrons the radius is fixed and the magnetic field is increased synchronously with the revolution of the particles.
Those types of accelerators are really expensive and not so widespread in centers around the world. The main technique used in radiotherapy involves, indeed, the use of photon beams generated by Linear Accelerators, which actually accelerates electrons that will then undergo bremsstrahlung emission.
Currently, there are two main manufacturers that produce LINAC for medical uses worldwide, and they are *Varian Medical Systems* [14] and *Elekta* [1] [15].

The former is an American radiotherapy machines and softwares maker with headquarter in Palo Alto, California. The latter is a Swedish company specialized in oncology medical devices production located in Stockholm.
Linear Accelerators produced by those two societies have some peculiar features that differentiate between them. However, LINACs have some basic features that are common among all typologies. The main components of a medical Linear Accelerator are: the stand, the gantry and the patient couch [16].
Figures 1.2 and 1.3 represent two medical Linear Accelerators produced by Elekta and Varian respectively.

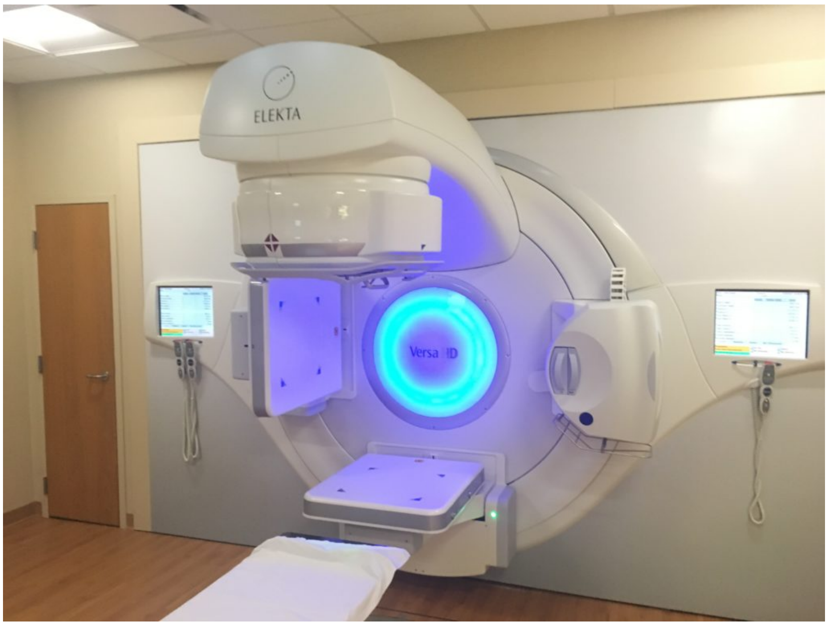

Figure 1.2: Elekta Versa HD LINAC system.

Figure 1.3: Varian TrueBeam LINAC system.

1.2.1 Beam production

The beam production starts in the stand. Here, an electron beam is produced by a thermionic emitter using *magnetron* modules, which are depicted in the following image.

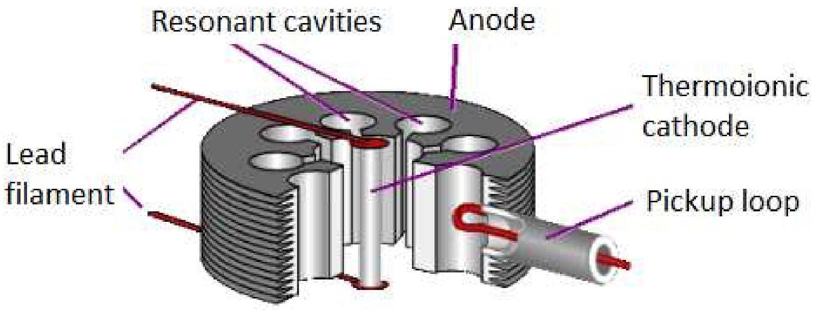

Figure 1.4: Magnetron module scheme.

Electrons emitted by the cathode are affected by an electrostatic force given by the potential difference between anode and cathode (which imparts a radial movement) and a magnetic force given by an external magnet (which imparts an azimuthal movement). The functioning of the magnetron is based on the LC oscillating circuit model: each cavity acts as a tiny LC circuit (where the inductance and the capacity are disposed in parallel), so when an electron produced by the cathode passes near a resonant cavity, it induces a positive charge on the virtual capacitor plate of that cavity, then approaching the next one it again induces a charge that creates a current pulse around the cavity. This current pulse is sustained by the LC configuration of the cavity, and tends to continue oscillating with a frequency that depends on the system geometry. The first oscillation is then held up by the next electrons emitted.
The electron beam generated in this way is then collected and focused into an accelerating waveguide, which is composed of a series of hollow metal tubes of increasing length. In these, an accelerating voltage is applied oscillating with a fixed frequency, so that the electron traveling through the tubes always encounters the wave ridge, and thus always increases in energy. This also explains why the tubes have to increase in length, since otherwise the beam motion would not be synchronized with the potential oscillation. Here a sketch of the accelerating system is provided.

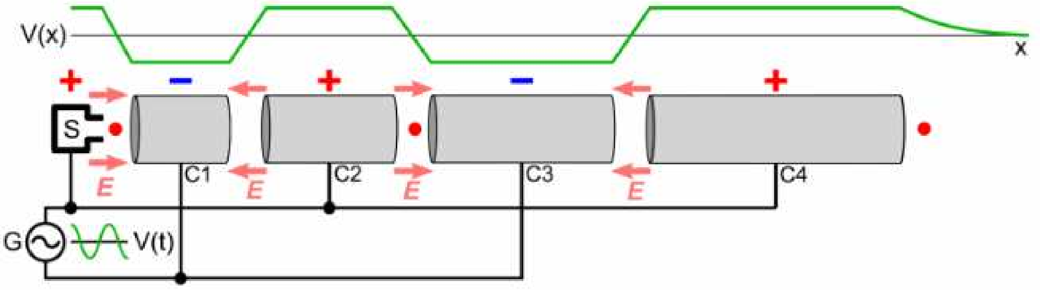

Figure 1.5: Accelerating waveguide functioning scheme.

Exiting the accelerating waveguide, the beam is transported to the gantry by the use of a series of bending magnets. Usually, three pairs of magnets positioned in succession (this is called *fly tube*) focus the electron beam on a diameter of approximately 1 mm. This focalises the beam to properly hit the target. Moreover, the bending magnets are positioned in order to form an achromatic multiplet, allowing electrons of slightly different energies to be focused on the same target point. Image 1.6 portraits a classic achromatic triplet fly tube.

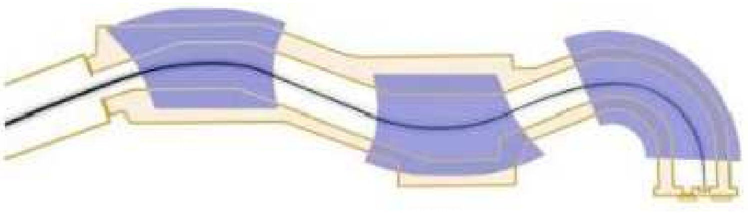

Figure 1.6: Fly tube example with three bending magnets.

In the gantry, there is the possibility to convert the electron beam into a photon beam with the usage of a tungsten target plate: the electrons hit the target and produce photons by bremsstrahlung emission. So, by inserting or removing the tungsten plate, the LINAC can be switched between electrons mode and photons mode.
The last important component that is present in the gantry is the so-called *flattening filter*, which is a device used in photon mode to flatten the forward-peaked photon beam obtained by bremsstrahlung [17]. In fact, it modifies the narrow and center-uniform photon beam in a clinically useful one through a combination of attenuation at the center and scatter at the external border. It is typically made of high Z materials (such as iron, tungsten, copper or a combination of those) and can be removed if necessary to obtain Flattening Filter Free (FFF) beams, which are characterized by a peculiar profile of Off Axis Ratio (OAR) distributions and by some parameters that differ from the usual beams With Flattening Filter (WFF), such as the depth of the maximum of Percentage Depth Dose (PDD) distributions (for more details, consult Section 1.3). The following image exemplifies the effect of the flattening filter on clinical beams.

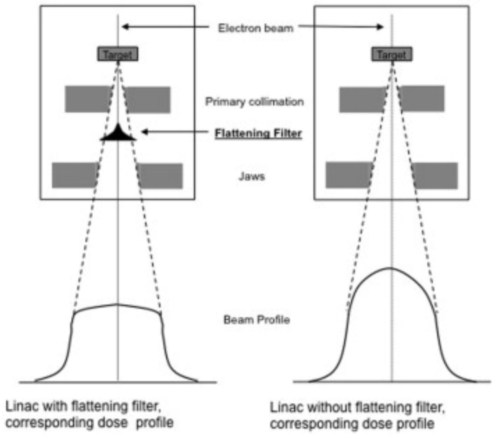

Figure 1.7: Flattening filter effect on a photon beam. On the right, a typical Off Axis Ratio profile FFF; on the left, the same profile WFF.

The energies of photon beams and electron beams that the investigated VERSA HD LINAC is able to produce are respectively: 6, 10 MV for photons and 6, 8, 10, 12, 15 MeV for electrons.

1.2.2 The gantry

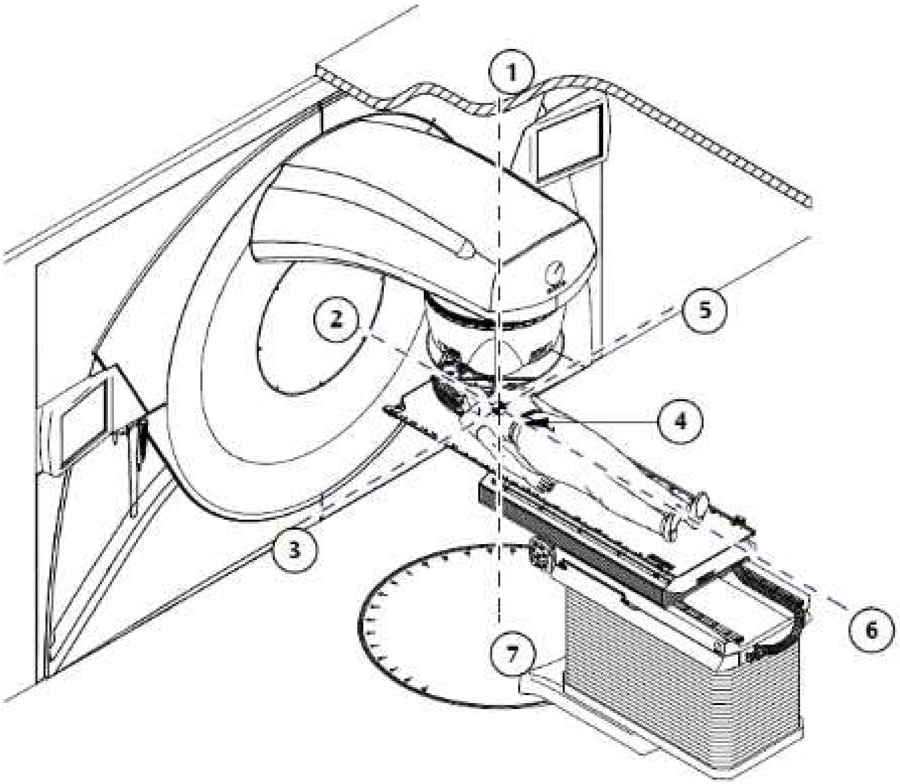

Figure 1.8: Elekta Versa HD gantry's reference frame [16].

The gantry constitutes the reference frame of the system. The center of this frame is called *isocenter* (number 4 in Figure 1.8) and represents the central point of the isoplane, which is the surface on which the patient lays. The axis directions are called inline ("y" direction, from 2 to 6 in Figure 1.8), crossline ("x", 3 to 5 in Figure1.8) and depth ("z", 1 to 7 in Figure 1.8). During VMAT treatments, the gantry will rotate around the isocenter in order to deliver the estimated dose distribution along the arcs.

The main component of the gantry is the head that contains the beam collimator structure. Nowadays the most widespread collimator type for LINACs is the Multi-Leaf Collimator (MLC). For the scope of this thesis we will consider the Agility head multi-leaf collimator [16], since it is the type mounted onto the Versa HD LINAC and used during measurements [15].

The Agility head MLC comprehends 160 paired leaves with a thickness of 9 cm and a projected leaf width of 5 mm at the isocenter. Their movement is guided by the carriage system that overall can reach a speed of 6.5 cm/s. The accuracy of the positioning of the leaves is guaranteed by the Rubicon optical tracking system. Leaves have an interleaf gap less than 0.1 mm and are defocused from the source (assuming a trapezoidal shape) to prevent interleaf radiation leakage.

Because of that, no backup collimator is needed [16].
The MLC structure is present only in the crossline (x) direction, while for the inline (y) direction there exists a block collimator composed by two metal jaws that limit the field extension. Along this direction is thus not possible to manipulate the field shape, besides enlarging or shrinking it.
The main difference between the Agility head MLC and a standard MLC is that the former presents the possibility of leaves interdigitation, which means that the leaves can extend over the symmetry axis of the collimator structure, whereas in a classic MLC the leaves are limited to their half of the structure. The comparison of the two possibilities is shown in the following figure.

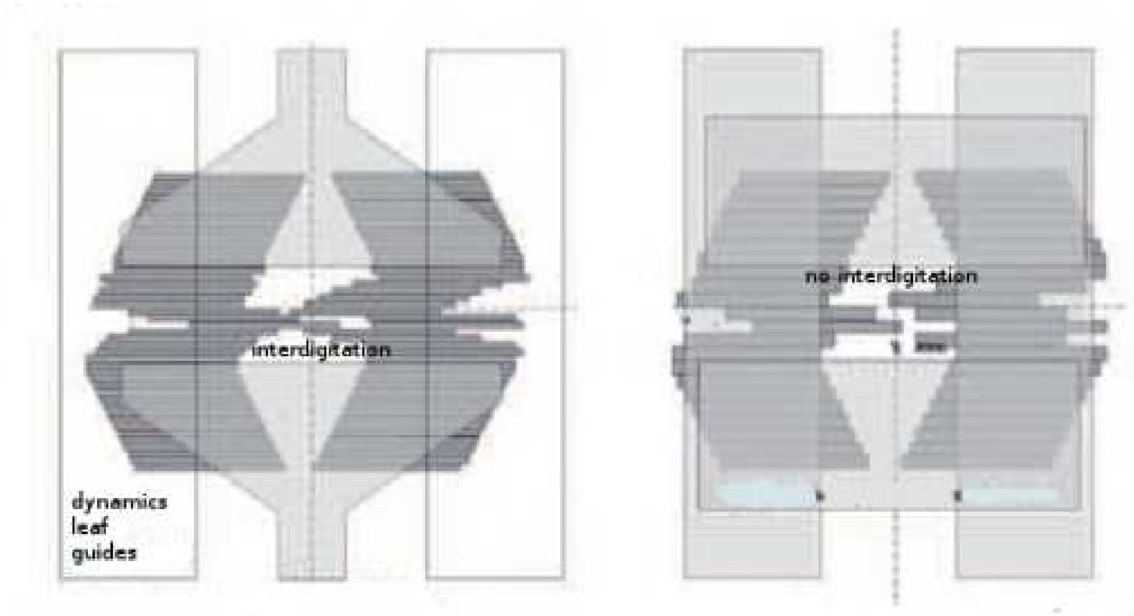

Figure 1.9: Agility MLC structure (left) versus a conventional MLC (right) [16]. As can be seen, leaves interdigitation is allowed for the Agility head while the classic MLC leaves movement is restricted to half the whole lenght of the collimator structure. The horizontal blocks depicted in grey in both pictures are the jaw collimators, while the vertical ones (only present in the conventional MLC sketch on the right) are backup collimators, which are aligned with the most backward leaves.

The collimator structure allows to create various field dimensions, reaching a maximum side length of 40 cm. In principle many shapes are possible, but in this thesis we will focus on square fields.
A screenshot of the software controlling the collimator structure is shown in the following figure.

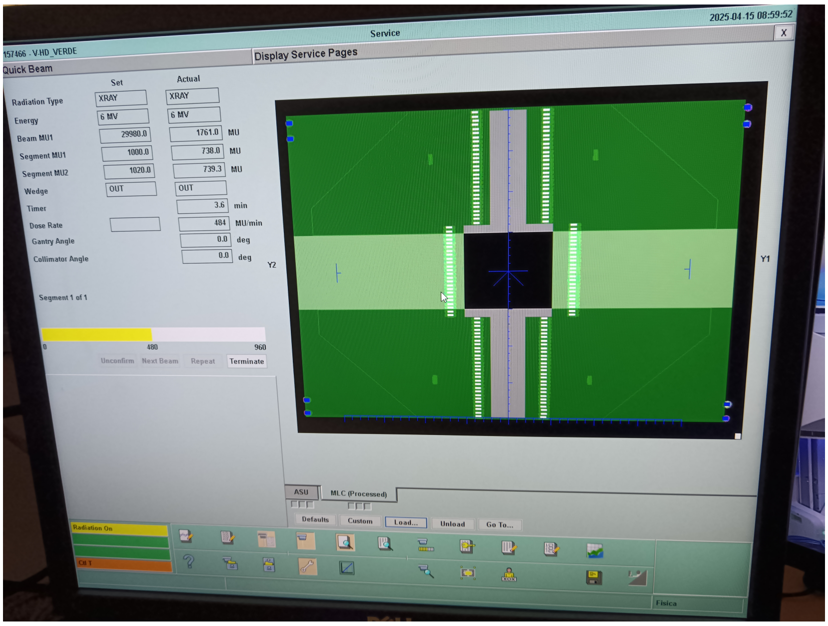

157466 - V-HD_VERDE

Quick Beam

	Set	Actual	
Radiation Type	XRAY	XRAY	
Energy	6 MV	6 MV	
Beam MU1	29980.0	1761.0	MU
Segment MU1	1000.0	738.0	MU
Segment MU2	1020.0	739.3	MU
Wedge	OUT	OUT	
Timer		3.6	min
Dose Rate		484	MU/min
Gantry Angle		0.0	deg
Collimator Angle		0.0	deg

Segment 1 of 1

Figure 1.10: Screen of the collimator-control software.

From the software, it is possible to change various parameters regarding the beam delivery. Here are listed the main ones used during this thesis work:

- The **delivered dose**, measured in Monitor Units (MU). This is an arbitrary unit of measurement of radiotherapy machines that must be converted to Gray (Gy) or Sievert (Sv) when performing absolute dose measurements through conversion factors. The usual conversion ratio is 100 MU to 100 cGy.
  The Agility head is equipped with two control cameras (called "Segment MU1" and "Segment MU2" in Figure 1.10) that monitor the dose delivery and stop the beam when the delivered dose reaches the value set by the operator. The control panel presents the possibility to switch to "control-T mode", allowing the beam dose delivery to become basically unbound (it actually still has a maximum dose delivery value, which is fixed at 29980 MU).

- The **dose rate**, which is the amount of dose delivered by the LINAC in a certain amount of time (it is measured in monitor units over minutes, MU/min). It is a very important parameter because it determines how quickly the dose is delivered to the target.
  There is a substantial difference between the dose rates of the WFF and FFF beams. In fact, the latter present a significantly higher dose rate compared to the former: the maximum values lay around 600 MU/min for WFF and 1400 MU/min for FFF.
  In the case of VERSA HD LINAC, if left unbound, the dose rate is automatically set to ∼470 MU/min for WFF and to ∼1360 MU/min for FFF. Since the dose delivery of the LINAC works by "dose packets" of a predetermined size, only a small set of dose rate values is available and the system rounds the effective dose rate to the nearest possible value.
  Actually, there is a delivery mode (called "always-on" mode) that uses finer dose rate steps, leading to a larger range of achievable values.

- The **field dimensions**, which can be set up to a maximum side of 40 cm.

Finally, for the photon beams there is the possibility of inserting a 60°*wedge filter* in the beamline at the head of the gantry. Its purpose is to manipulate the beam intensity over the field extension, thus modifying the dose distribution; however, it will not be used throughout our measurements.

1.2.3 The patient couch and other attachments

In general, the gantry may be provided with some imaging attachments, which are useful for in-vivo imaging or beam control measurements. In particular, the VERSA HD LINAC is equipped with two accessories called *iView* and *XVI* [15] [16].

iView consists in a silicon diodes array connected to a scintillator plate. Its surface can be irradiated for a maximum area of 26×26 cm^2, so as not to affect the surrounding electronics. However, the detector plate can be moved freely around a 40×40 cm^2 area, so that the full field width can be scanned by the union of various 26×26 cm^2 images [16].
This device is useful to obtain megavolt (MV) setup images or for patient's alignment, as well as for beam control scans (for instance regarding the geometry and the orientation of the beam).

XVI consists of an x-ray tube and its own image acquisition panel. This panel has dimensions of 40.96×40.96 cm^2 and can be placed in three different positions depending on the Field Of View (FOV), which in turn can be *small*, *medium* or *large*. In the *small* configuration the maximum FOV diameter is 270 mm, which allows volumetric acquisitions to be performed with a minimum rotation of 200°. On the other hand, the maximum diameters for the *medium* and *large* configurations are respectively 410 mm and 500 mm, which need a full rotation in order to perform a volumetric acquisition [16].
This system has various uses:

- It can acquire 2D static planar kilovolt (kV) images, or a sequence of them taken with fixed/rotating gantry.
- It can perform volumetric acquisitions (*cone beam*) that can be then compared with Computed Tomography (CT) images acquired for the treatment planning.
- It can register a respiratory cycle of the patient in order to perform a respiratory gating, which consists in switching on/off the beam delivery in synchrony with the patient's movements due to breathing. To do this, it is necessary to perform a 4D acquisition where a CT is slowly acquired. During reconstruction, the patient's respiratory cycle is recreated thanks to an analysis of the patient's diaphragm positions through the observation of different gray-tone gradients. The standard procedure requires a 200°rotation at 50°/minute speed, in order to obtain 1400 images to be subdivided into 10 respiratory phases. Those images are registered as 2D projections so that one collects some series of ordered projections referring to each breathing

phase. These series are then reconstructed using an algorithm into CT 3D cone beam images series which are finally chained into a CT 4D cone beam image.

All these functions are essential for the correct positioning of the patient, which is thus adjusted by a software connected to the XVI, using a coordinate system analogous to the LINAC's one.

The last component of a radiotherapy accelerator clinical system is the patient couch, which is the place where the patient is positioned during treatments. For the VERSA HD LINAC, the couch is called *Hexapod* and it comprehends two main components: the *HexaPOD evo Couchtop* and the *iGuide* system [16]. Figure 1.11 represents a picture of the Elekta Hexapod.

Figure 1.11: Elekta Hexapod patient couch.

1. The HexaPOD evo Couchtop is the main planar table where the patient will be positioned, and can be maneuvered with translations and rotations around three axis, thus reaching six degrees of freedom. It is made of a carbon fiber material and its physical dimensions are depicted in Figure 1.12.

2. The iGuide system controls the couch position through a radiopaque holder and an infrared camera which can transmit to a software spatial data in order to obtain the necessary displacements.

Figure 1.12: Scheme of the couchtop dimensions (frontal view) [16].

The hexapod has a reference frame too, which must be integrated with the linear accelerator's one.

1.3 Dosimetry

Dosimetry is a discipline that consists in the study of the energy dose absorbed by a material when exposed to ionizing radiations. It founds various applications in medical physics, for example among radiotherapy, radiodiagnostic, nuclear medicine and radioprotection fields. In particular, we will focus on the main aspects about dosimetry when considered by the radiotherapy point of view, which will be useful for the successive analysis carried out in Chapter 3.

In radiotherapy, dosimetry gets involved principally when dealing with a procedure called *commissioning*: it is a complex process with the goal of setting up the LINAC machine in order to be ready for clinical use [1]. Indeed, a linear accelerator needs to be modeled into a so called *treatment planning system*, which is a software used to plan the radiotherapy treatment that will be administered to the patient. The treatment plan is constructed using a modeling of the radiotherapy machine that emulates the LINAC's behavior, so that, starting from a computed tomography of the patient the operator can construct the best fitting plan for the case of interest, exploiting the various radiotherapy techniques (such as IMRT or VMAT). To do that, a series of dosimetric measures about the LINAC beam have to be performed. We can distinguish between relative dosimetry measures (such as PDD, OAR or Field Output Factors) and absolute dosimetry measures (so absolute dose deposition measures). All those measurements follow international regulations written by the International Atomic Energy Agency (IAEA), in particular in the IAEA TRS-398 Code of Practice [2].

In the next Sections some useful concepts about dosimetry and dosimetric measures will be introduced, followed by the description of the TRS-483 formalism [5].

1.3.1 Dosimetric quantities

The main dosimetric quantities that are encountered in radiotherapy are the absorbed dose (D) and the kerma (K).

The absorbed dose at a point P due to ionizing radiation is defined as the mean energy deposition divided by the mass element positioned in P [18]:

$$D = \frac{d\bar{E}}{dm} \tag{1.1}$$

$\bar{E}$ is the mean deposited energy and it is calculated as [18]:

$$\bar{E} = \overline{\sum_i \varepsilon_i} = \overline{\sum_i (\varepsilon_{in} - \varepsilon_{ex} + Q)} \tag{1.2}$$

that is a sum of the energy deposits of various interactions (i is the interaction index) inside the considered volume V. Each interaction takes into account the radiant energy[1] of the incident ionizing particle (ε_{in}) entering the volume, the

---

[1] The radiant energy is the energy possessed by the particle, excluding its rest energy.

sum of the radiant energies of all the charged or neutral ionizing particles emerging from the interaction (ε_{ex}) and the Q-value of the reaction (Q). The "average" calculation derives from the fact that energy deposition by a ionizing particle crossing a material is intrinsically a stochastic phenomenon. E is thus a random variable and follows a distribution that mainly depends on the volume and the mass considered. In fact, increasing the mass also increases the number of interactions and as a consequence the variability in the total energy deposition becomes smaller (on the contrary, the smaller the volume the easier it is to observe considerable fluctuations on deposited energy for repeated measurements). From its definition, we can also write the $\bar{E}$ expression as:

$$\bar{E} = \bar{E}_{in} - \bar{E}_{out} + \bar{Q} \tag{1.3}$$

where $\bar{E}_{in}$ and $\bar{E}_{out}$ are the average sum of the radiant energies of all the ionizing radiation particles (both charged and neutral) respectively entering and leaving V.

The unit of measure of the absorbed dose is the Gray (Gy) that corresponds to one Joule per Kilogram (1 Gy = 1 J/Kg).

The kerma (K) is a quantity defined only for indirectly ionizing radiation, that is neutral radiation (photons and neutrons) that does not directly transfer its energy to matter, but first transfers it to some particles (called secondary charged particles) which then perform ionization and energy deposition. K is defined as [18]:

$$K = \frac{d\bar{E}_{tr}}{dm} \tag{1.4}$$

with $d\bar{E}_{tr}$ the average energy transferred to the volume V having mass dm. E_{tr} is a quantity calculated as [18]:

$$E_{tr} = E_{in,ind} - E_{out,ind}^{non\,rad} + Q \tag{1.5}$$

where $E_{in,ind}$ denotes the total radiant energy of the indirectly ionizing radiation entering V and $E_{out,ind}^{non\,rad}$ includes the total radiant energy of the indirectly ionizing radiation leaving V that does not come from radiative energy loss processes of the secondary charged particles liberated in V (so for instance it does not count for bremsstrahlung radiation). Q is again the Q-value of all processes that occur in V.

In this way, K embodies the sum (over the volume mass) of the kinetic energy of all secondary charged particles generated in the volume by the primary radiation interaction with the medium. Those particles can lose their kinetic energy through processes of ionization and excitation of the crossed medium atoms or can undergo radiative processes such as bremsstrahlung and in flight positron-electron annihilation. The kerma can thus be distinguished into two components: the collisional kerma (K_{coll}, referring to ionization/excitation processes) and the radiative kerma (K_{rad}, referring to radiative processes).

$$K = K_{coll} + K_{rad} \tag{1.6}$$

Another important dosimetry concept is the Charged Particles Equilibrium (CPE). In a certain irradiated volume V, CPE is verified if each charged particle of a given type and energy leaving V is replaced by an identical particle of the same energy entering V and expending its kinetic energy inside V (in terms of expectation values):

$$\sum_i T_i^{in} = \sum_i T_i^{out} \tag{1.7}$$

where T_i^{in} denotes the kinetic energy of the i-th particle entering the volume, while T_i^{out} is the one exiting. Briefly, CPE condition ensures that all energy released in V is actually absorbed in V [18].

The main condition that has to happen in order for CPE to occur is that the volume V considered is enclosed inside another larger volume V', such that V' borders have a distance from V borders that is larger than the range of any secondary charged particle generated inside V' from the primary radiation. Furthermore, the attenuation of the indirectly ionizing primary beam during its passage through the medium must be negligible.

Finally it is possible to demonstrate that, in the presence of charged particles equilibrium [18]:

$$D \overset{CPE}{=} K_{coll} \tag{1.8}$$

This is a very important relationship in dosimetry, because it allows to calculate the absorbed dose under CPE from knowledge of the photon energy fluence and mass-absorption coefficient of the material.

The last dosimetry-related parameter that we encounter is the beam quality, Q. This is an indicator that is mainly connected to the penetration capability of the considered beam, together with its particle type composition. Q provides a quantitative indication of the penetration power of a certain radiation beam. Although it is correlated with the energy spectrum of the radiation of interest, it is easier and quicker to measure with respect to a direct measurement of the radiation energy. Relying on these properties, Q is used in place of quantitative energy information about a radiation beam. In Sections 1.3.3 and 1.4 all the parameters depending on the energy of the beam are expressed as a function of Q, as indicated in international Codes of Practice (such as the TPR-398 document) [2], where the experimental procedures and conditions for the determination of the Q parameters are explained, too.

Regarding photon beams produced by linear accelerators, the two possible quality indicators are the $TPR_{20,10}$ and the $\%dd(10)_x$.

$TPR_{20,10}$ is known as Tissue-Phantom Ratio, and it is calculated as the ratio between the dose absorbed in water at a depth of 20 cm and 10 cm respectively, with a fixed SDD (Source to Detector Distance) of 100 cm and with a field size of 10×10 cm^2 (the detector must be placed on the central axis of the field) [18].

$$TPR_{20,10} = \frac{D_w(20)}{D_w(10)} \tag{1.9}$$

$\%dd(10)_x$ is an alternative quality indicator that was introduced by the American Medical Physics Association (AAPM) and it is defined as the percentage depth dose (PDD, here called %dd) determined 10 cm deep in water on the central axis of a 10×10 cm^2 field and with a SDD of 100 cm [18].

There are pros and cons in the choice of using either quality indicator, but overall it is preferable to use the $TPR_{20,10}$, since it presents more advantages than disadvantages with respect to the $\%dd(10)_x$.

1.3.2 Relative measurements

A key branch of dosimetry measurements is represented by relative measures. Those are a kind of measure where we do not care about absolute values (so for instance the effective value of the deposited dose in Gy) but we only consider normalized values or measurements ratios over some references.
The three main categories are Percentage Depth Dose distributions (PDD), Off Axis Ratio distributions (OAR) and Field Output Factors (FOF).

PDDs consist in the energy dose deposition distribution along the z direction (in the reference frame of the LINAC), that is going deep into the crossed material, away from the source (the gantry head). Depending on the radiation considered, the PDD takes a well specific shape:

- Protons and heavy ions show the so called *Bragg distribution*, which is a consequence of the interaction that heavy charged particles (such as hadrons) have with matter. This interaction is described by the Bethe-Bloch equation, which is an expression for the *linear stopping power* (S) of the material on the radiation:

  $$S = \left|\frac{dE}{dx}\right| \propto \frac{z^2}{\beta^2} \cdot \frac{Z}{A} \cdot f\left(\beta\right) \tag{1.10}$$

  The stopping power represents the amount of energy that the ionizing particle (the projectile) loses for each unit length traveled in the material (the medium). It depends on the projectile characteristics (z and β which are respectively the charge, in multiples of the electron charge, of the ionizing particle and its velocity normalized to c), on the medium characteristics (Z and A which are the crossed material atomic number and mass number) and a function $f(\beta)$ that takes into account other effects (for instance, relativistic effects).
  The Bragg distribution is characterized by the Bragg peak, which is a narrow area near the endpoint of the curve where the particle will release most of its energy.

- Electrons behavior and their PDD shape is driven by Coulomb interactions with charged subatomic particles. This leads to high surface dose and a rapid fall-off.

- Photons are an example of indirectly ionizing radiation, and the shape of their PDD distribution is deeply connected with this fact, because of Equation 1.8. Indeed, K is proportional to the fluence of the primary photon beam, and for this reason its depth profile has the form of a falling exponential, while the dose depends on the energy that is actually deposited in the medium by the secondary charged particles. Near the surface of the medium CPE is not yet achieved, and so the PDD profile presents a first rise to "catch up" with the kerma, until a large enough depth is reached

and the dose starts behaving like the collisional kerma, thus falling down with a sort of exponential tail [19] [20].
The photons PDD is characterized by its maximum, in particular by the depth at which its maximum is reached, called d_{max}. This parameter depends on the endpoint energy (so the penetration capability) of the beam and also on the filter applied. In fact, FFF beams present an higher d_{max} value for the same endpoint energy of the primary beam [19] [20].

Here is a graph depicting the three PDDs just described at comparison.

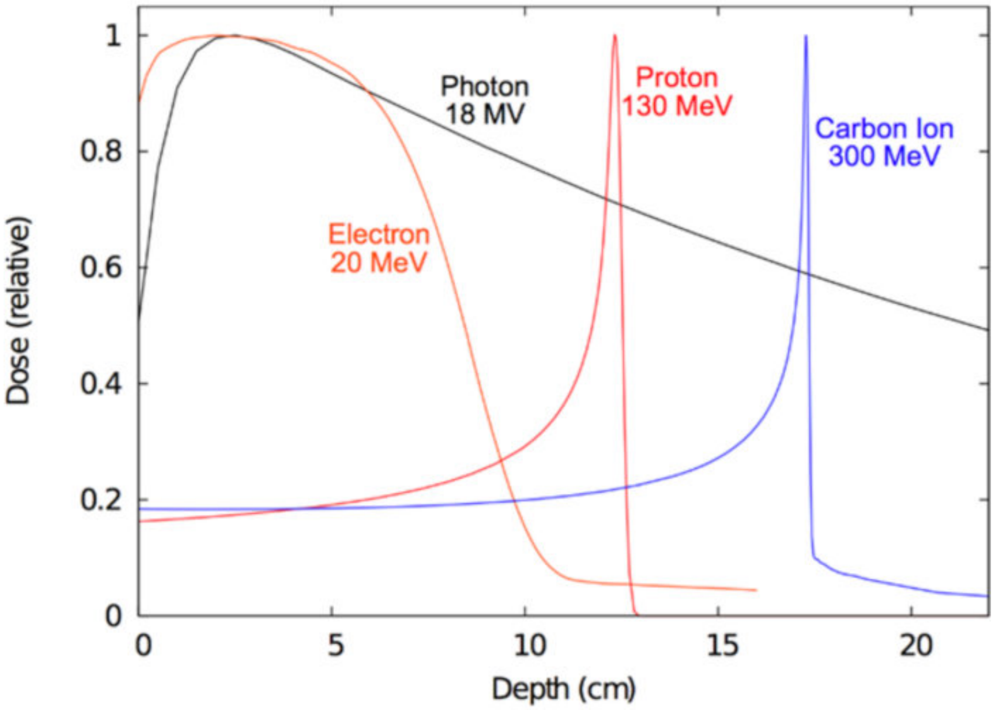

Figure 1.13: PDD comparison of photons (18 MV energy) with electrons (20 MeV), protons (130 MeV) and ^{12}C ions (300 MeV). It is easy to notice how the distributions varies with the depth among the radiation types.

Usually, PDDs are normalized as a percentage (%) to the maximum value of the distribution. Alternatively, it is also a common choice to normalize them to the value corresponding to a depth of 10 cm.

OARs consist in the energy dose deposition distribution along the x or y direction in LINAC's reference frame, so scanning transversely with respect to the beam propagation direction. Usually these kind of measurements are performed keeping one of the two horizontal coordinates fixed at 0 while the other will be scanned. z is fixed too, and its value depends on the reference conditions adopted.
Regarding the photons OAR, which is our case of interest, they take the shape of a "square box" with penumbrae falls and prominent shoulders (this last characteristic is more evident for larger field sizes). An example of the shape follows.

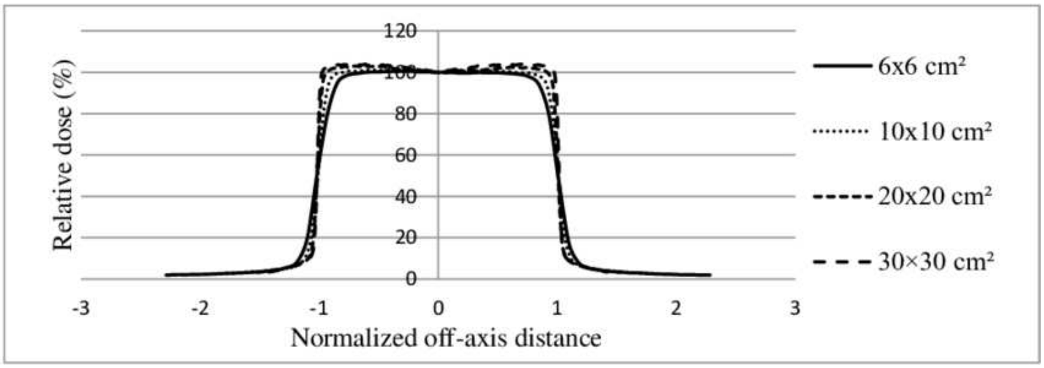

Figure 1.14: OAR profile shape example. On the right the field dimensions are noted, and the x coordinate is normalized with respect to half the field dimension in each case.

The main parameters of an OAR distribution are the central value and the penumbrae width. The reason why penumbrae appear is that the photons interacting with the medium produce a cascade of secondary electrons that may extend over the geometrical limits dictated by the field dimensions. The real dimensions of the field can be deduced by the OAR calculating its Full Width at Half Maximum (FWHM). Actually, as will be explained in Section 1.4, for small fields (sides of few millimeters order or less) a square field width is calculated as the geometrical mean between the FWHM of the inline OAR and the crossline one.
OAR distributions change shape when using FFF beams [21] [17]. In fact, flattening filters are exploited to obtain a uniform intensity profile along the treatment field, which otherwise would have a bell shape with the highest intensity at the center due to its production by bremsstrahlung emission. A FFF beam has thus the shape of a bell with again falling penumbrae, as can be seen in the following image.

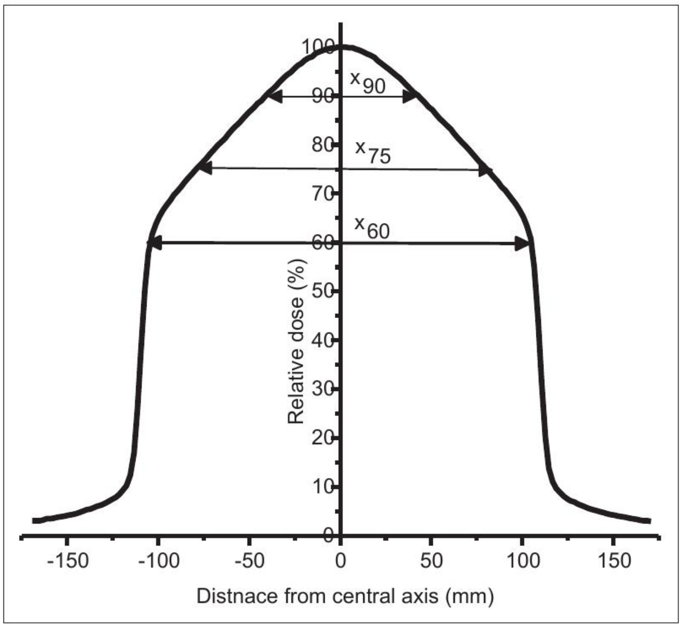

Figure 1.15: OAR distribution by an FFF photon beam.

Normally OAR are normalized to the value of the central point, both in the WFF and FFF cases.

FOF are pointwise measurements and are constructed as the ratio between the measured dose at one point in space obtained by using a certain field size over the dose at the same point obtained by using the reference field size, that is 10×10 cm^2 for conventional radiotherapy machines. The ratio is performed between two dosimeter signals, since it is not important to include absolute dose "conversion" factors as they will just get canceled out in the fraction. This is why FOF are considered relative measurements.

Regarding PDDs and OARs, the reference value taken to turn them into relative measurements is the one obtained from a reference detector. It consists in a dosimeter attached near the gantry exit of the beam. In this way, its reading is unaffected by the placement of the main detector and represents an almost constant value for all the acquisitions. It can be useful even to become aware of some malfunctions that may affect the principal detector. The final signal will be the ratio between the main detector and the reference one, so that the effect of the variations in the accelerator output is eliminated.
Being placed very close to the source, the reference detector projects a "shadow" onto the clinical radiation field on the isoplane. This does not constitute a problem for relatively large fields (of the order of 5 cm side or above) but can become really error-prone when used with smaller fields, since the reference detector body may cover a large amount of the radiation field. To avoid this, it is possible to use a *stealth camera* as a reference dosimeter, which is a sort of "detector mask" that is mounted directly onto the gantry head and does not interfere significantly with the beam delivery to the isoplane. Alternatively, one can simply not use any reference detector and just proceed to normalize the PDD/OAR distribution to its own desired point.

1.3.3 TRS-398 formalism

TRS-398 establishes that the reference medium for dosimetry measurements aimed at external photon beam radiotherapy is water [2]. This choice is made relying on some considerations:

- Water is one of the best tissue-equivalent materials available, since its effective atomic number is very similar to the one of biological tissues, in particular soft tissues. The human body is indeed composed by a large fraction of water (approximately 70%).
- Water is easily obtainable and usable in phantoms, due to its characteristics (it is transparent and homogeneous, adapts to the container, easy to use at standard conditions).
- Radiation interaction with water is well known and also affordable to be modeled to perform simulations (as Monte Carlo simulations).

Because of this, all dosimetry measurements have to be performed using water phantoms.

Regarding absolute dose measures, in particular considering reference conditions (*reference dosimetry*), the dose deposited in water at a reference depth z_0 for a reference beam quality Q_0 can be calculated as [2] [18]:

$$D_{w,Q_0} = M_{Q_0} N_{D,w,Q_0} \tag{1.11}$$

where M_{Q_0} is the reading of the dosimeter under the reference conditions used in the standards laboratory and N_{D,w,Q_0} is the calibration factor in terms of absorbed dose to water of the dosimeter obtained from a standards laboratory.
Reference conditions are described by a set of values which influence the measurement and for which the calibration factor is valid without further correction. For example, reference conditions take into consideration: the ambient temperature, pressure and humidity; the distance of the detector from the source (SDD, Source to Detector Distance) and the depth into the medium; the field size; the dimensions and the material of the phantom. The standard detector choice for absolute measurements are ionization chambers.
Since usually clinical conditions do not match the reference ones, one has to correct for all the discrepancies between standard and real conditions. In addition, there are some influencing quantities that must be taken into consideration when calculating the final absolute dose. For instance, to account for the temperature and the pressure of the water phantom one has to multiply its ionization chamber's reading by k_{tp}, which is the temperature-pressure correction factor, in order to obtain the term M_{Q_0} in Equation 1.11. The corrections to apply to the chamber's reading when dealing with medium voltage photons (MV) in external beam radiotherapy regard: temperature, pressure, polarity, electrometer calibration [2] [18].
Moreover, if the radiation quality is not the one of reference (Q_0) it is necessary to introduce a parameter that accounts for this difference [2] [18]:

$$D_{w,Q} = M_Q N_{D,w,Q_0} k_{Q,Q_0} \tag{1.12}$$

where k_{Q,Q_0} is the factor "converting" the measure from the used quality Q to the reference quality Q_0. It is defined as the ratio of the calibration factors (in terms of absorbed dose to water) of the ionization chamber at the qualities Q and Q_0 [2] [18]:

$$k_{Q,Q_0} = \frac{N_{D,w,Q}}{N_{D,w,Q_0}} = \frac{D_{w,Q}/M_Q}{D_{w,Q_0}/M_{Q_0}} \tag{1.13}$$

The most used reference quality for external beam photon radiotherapy, regarding the calibration of ionization chambers for absolute dosimetry, is the ^{60}Co gamma radiation [2] [18].
Those correction factors can in principle be calculated theoretically using Bragg-Grey theory. However, it is more convenient to rely on experimentally measured k_{Q,Q_0} values tabulated in the Codes of Practice literature. A summary of the reference conditions for dose determination in medium energy photon beams is displayed in the following table [2].

MV photons reference conditions	
Influencing quantity	**Reference value/characteristic**
Phantom material	Water
Chamber type	Cylindrical
Measurement depth	2 g/cm^2
Chamber's reference point	On the central axis at the center of the cavity volume
Position of chamber's reference point	At measurement depth
Source to Surface (of water) Distance (SSD)	Usual treatment distance
Field size	10×10 cm^2

Table 1.1: Summary of all reference conditions for absolute dosimetry with MV photons. The measurement depth is measured in g/cm^2 since it is calculated as the *thickness* of the medium, which is found multiplying the classical depth (in cm) by the medium mass density (in g/cm^3).

1.4 Small fields dosimetry

Dosimetry poses a considerable challenge when dealing with small-fields [3] [4]. The reasons for this are various and all of them relate to the reduced extension of the radiation field with respect to the dimensions of the detector or the range of the secondary charged particles created.

Despite the lack of a proper definition of "small-field", we can identify three main aspects to be taken into consideration to determine whether a field can be thought as small or not:

- The absence of lateral charged particles equilibrium;
- The partial occlusion of the primary radiation source through the collimator;
- The size of the detector being bigger than the field extension.

1.4.1 Lateral charged particles equilibrium

Lateral charged particles equilibrium (LCPE) consists in obtaining CPE conditions at the edges of the radiation field. We already know that the smaller the volume, the harder it is to reach CPE conditions, since the secondary charges range has to be lower than the typical length of the system. Then, a photon field can be considered as "small" when the distance between the field edge and its central axis is smaller than the lateral charged particle equilibrium range, r_{LCPE}, defined as the minimum radius of a circular photon field for which K_{coll} in water and D to water are equal at the center of the field. r_{LCPE} depends on the quality of the radiation and can be found following the formulas listed in the IAEA-483 protocol [5]:

$$r_{LCPE}(cm) = 8.369 \times TPR_{20,10} - 4.392 \tag{1.14}$$

$$r_{LCPE}(cm) = 77.97 \times 10^{-3} \times \%dd(10)_x - 4.112 \tag{1.15}$$

In conclusion, since our volume of interest is the detector volume, small field conditions can be assumed to exist when the external edge of the detector volume is at a distance from the field edge smaller than the rLCPE in the medium. Therefore, we consider as small field any field having a size lower than 2 LCPE ranges and the detector dimension:

$$FWHM \leq 2r_{LCPE} + d_{DET} \tag{1.16}$$

where $FWHM$ is the field size measured as the width of the dose distribution at half its maximum.

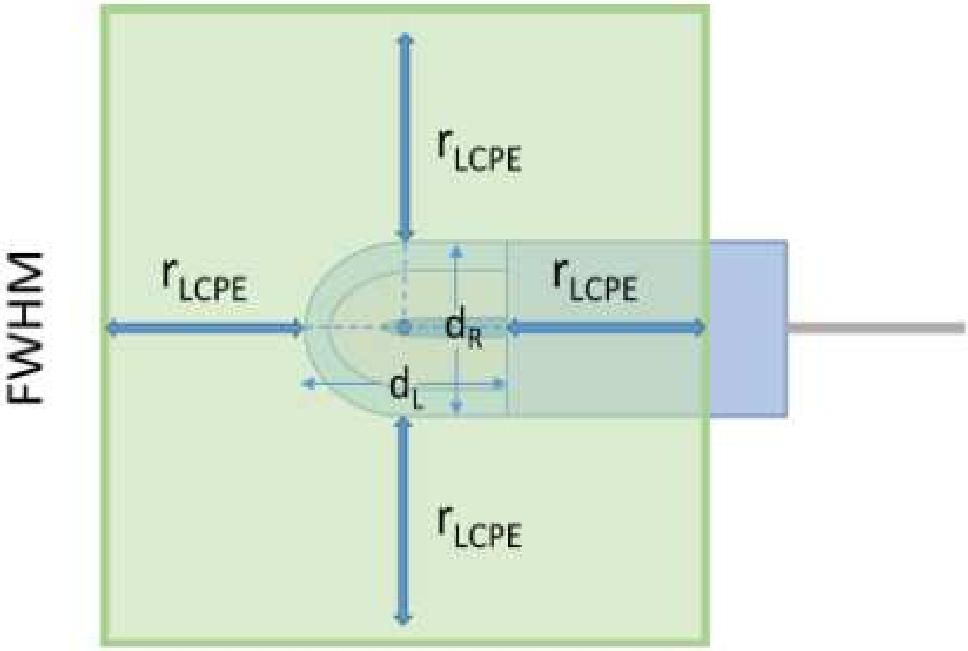

Figure 1.16: Visual scheme of the conditions for small fields based on r$_{LCPE}$.

1.4.2 Radiation source partial occlusion

The field dimension is set thanks to the combined action of the MLC in the crossline direction and the jaws in the inline direction. Those collimators effectively occlude the source in order to obtain the desired side length. Due to border effects, the field profile is not a perfect "square box" but presents the so called penumbrae at its edges. For usual large fields this does not represent an issue and the field width is calculated as the Full Width Half Maximum (FWHM) of an OAR distribution. For smaller fields however, left and right penumbra regions start to overlap. This causes the profile FWHM not to coincide with the real width, since the OAR distribution would be mostly made of penumbrae, which are located under the 50% level of the profile and thus have a larger width.

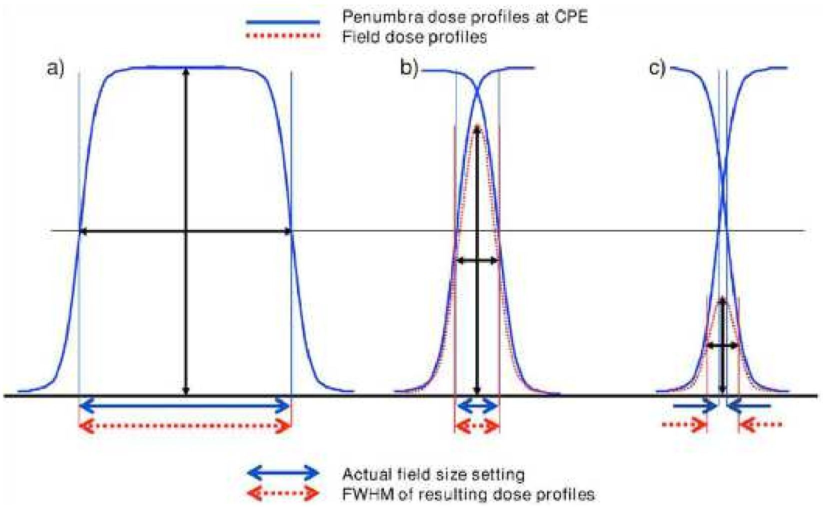

Figure 1.17: Small field penumbra overlapping. The rigth-most profile (c) clearly shows how the resulting OAR FWHM is actually higher than the real one.

Then, OAR FWHM is different from the nominal field width, and for this reason it is indicated with a proper name, S_{clin} [4], that is a quantity calculated for each field as the geometric mean between inline and crossline OAR FWHM. For large fields, S_{clin} coincides with the nominal field width.

Partial source occlusion also results in a reduction of the beam fluence. The radiation flux and consequently the absorbed dose will be lower (for example, at the center of the distribution) in comparison to the dose deposited with a larger field, for the same dose rate at the LINAC exit.

All these effects start to occur when the field sizes goes down to 3×3 cm^2 or less, and so we can consider this as a sort of dividing limit between large and small fields.

1.4.3 Detector size and field extension

As previously seen, the detector size influences the reaching of lateral charge particles equilibrium, and therefore we already know that it is a key factor in the categorization of small fields.

Beyond this, detector size and characteristics result in another important issue regarding small field dosimetry, which are the volume averaging effects.

In Section 1.4.2 we saw that a small field is characterized by overlapping penumbrae, leading to a nonuniform lateral dose distribution profile. As the detector produces a signal that is proportional to the mean absorbed dose over its sensitive volume, this signal will be affected by the homogeneity of the absorbed dose over the detection volume (volume averaging). This effect is particularly impacting for FFF beams [21].

Flattening filter free beams present another issue compared to WFF ones, that is the reduced scatter component at the reference depth, which makes the equivalent square field size smaller than that defined by the beam penumbrae.

In general, the detector size and other characteristics really influence its performances when dealing with small fields, so it is convenient to use specific detectors that are appropriate for small field dosimetry.

Chapter 2

Materials and methods

The measurement apparatus exploited for this thesis work mainly consists of the water phantom, where the movement system is mounted, the detectors and the reading electronics.
The detectors that have been used are:

- The Blue Physics Plastic Scintillator Detector (BP-PSD), which is the latest dosimeter developed, and we are particularly interested in studying its dosimetric properties and performances.
- The PTW microdiamond detector.
- The IBA Razor diode.
- The IBA EFD3G unshielded diode.

The last three detectors listed above are own by the AULSS 3 hospital, and thus are already integrated with the movement system and the acquisition electronics. This apparatus is managed by software, installed on a computer positioned outside the radiotherapy bunker (which in turn contains the whole accelerator complex), with which the operator has the possibility to move the detector, start acquisitions or even perform predetermined operations such as axis alignment.
The BP PSD is not yet integrated with the acquisition system. In fact, as will be seen in Section 2.2.1, it has its own acquisition and electronics apparatus which will be exploited in order to acquire the desired measures, in synchrony with the water phantom movement system.
Before actually acquiring the measurements, some initial tests and procedures have been performed: an alignment procedure, an Adjacent Channel Ratio (ACR) calibration, a dispensed dose linearity test and a dose rate stability test. The first two processes are discussed in Sections 2.3.1 and 2.3.2 of this Chapter, while the results for the dose linearity and dose rate stability tests will be presented in Section 3.1 of Chapter 3.

2.1 Water phantom

Figure 2.1: IBA Blue Phantom 2 water tank.

The water phantom used is an IBA Blue Phantom 2 water tank [10]. It has a total volume of $67.5 \times 64.5 \times 56.0$ cm^3 and a scanning volume of $48.0 \times 48.0 \times 41.0$ cm^3. Walls are made of acrylic and have a thickness of 15 mm [22].
It presents a detector holder installed on a mechanical arm that moves the former using a movement apparatus. This system allows for a position resolution of 0.1 mm and a consequent position accuracy of ± 0.1 mm. It can reach a scanning speed of 50 mm/s [22].
The phantom is integrated with a software which allows to control and perform all the required data acquisitions. The information regarding the holder's position and the actual signal of the detector are transmitted to the *My QA-accept* software throughout an electrometer. This device has two reading channels, since the second one is assigned to the reference field detector, which is mounted on a designated movable arm. It performs reference measurements in air and it is used along with the actual detector to obtain the PDD and OAR profiles for the PTW microdiamond detector, the IBA Razor diode, and the IBA EFD3G unshielded diode (since the Blue Physics Plastic Scintillator Detector, BP-PSD, is not yet integrated with the acquisition software and the whole phantom apparatus, it will not have a reference). The reference detector is placed at the edge of the field in order not to interfere with the reading of the other detector.
The whole system has some environmental functioning requirements: it needs a temperature in the range of 18-25°C; a relative humidity of 55-75% without condensation and a pressure in the 700-1100 hPa range (these values are the most strict between the requirements regarding the electronics and the phantom itself) [22].
The phantom is also equipped with an electrical lift table (where it is positioned) that permits to adjust the height of the system, and a water reservoir from which the water is pumped (in and out for filling and emptying).
Concerning Field Output Factors (FOF) acquisition, an external IBA Dose 1

electrometer has been used in order to collect pointwise measures [10].

2.2 Detectors overview

2.2.1 Blue Physics Plastic Scintillator Detector

BP-PSD is a plastic scintillator detector that collects the scintillation light throughout an optical fiber and sends it as a signal to the reading electronics.
It is made up of various parts [11]:

- The plastic scintillator detector.
- The transport optical fiber.
- A removable cartridge.
- An acquisition unit box.
- A computer with the Blue Physics software (BlueSoft) installed for the acquisition.

The following figure shows the main parts of the acquisition unit of the BP PSD.

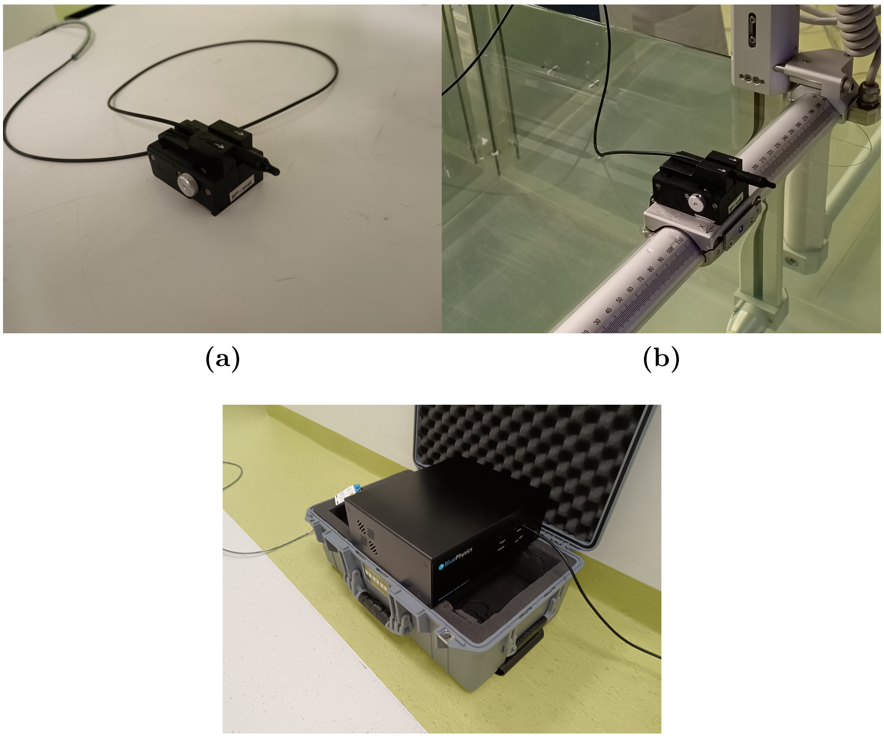

(a) (b)

(c)

Figure 2.2: Plastic scintillator detector mounted on the phantom holder outside (a) and inside (b) the phantom, with the transport optical fiber attached in the back. Figure (c) shows the acquisition unit box with the readout cartridge inserted.

The plastic scintillator is composed of a cylindrical active volume of 0.5 mm radius and 1 mm height, that leads to a total effective volume of 0.785 mm^3 [11]. Then it is coupled to the transport optical fiber that has a radius of 0.125 mm and a length of 20 m [11]. It connects the PSD with the acquisition box, sending the scintillation light to the removable cartridge, where a transducer coupled with the fiber converts this light into an electric signal. The rest of the acquisition unit will then integrate that signal by charging a capacitor for a certain integration time, after which the stored charge is read by the acquisition unit, the capacitor gets cleaned up and the charge information is converted into a digital signal using an Analog-to-Digital Converter. Ultimately, this signal is sent to the computer, where it is plotted in real time by the BlueSoft software.
A scheme of the plastic scintillator with its main components and attachments is shown in the following image [11].

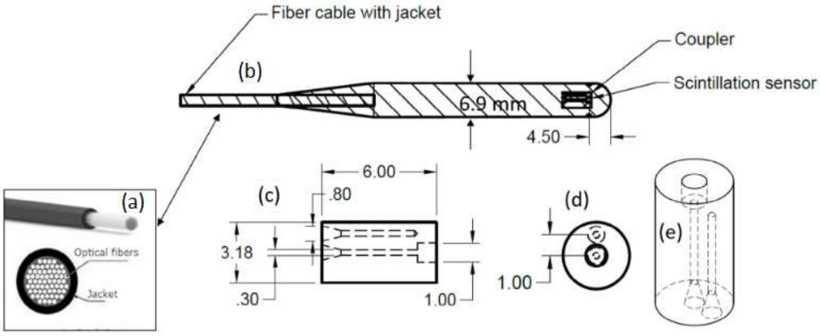

Figure 2.3: (a) Fiber optic casing. (b) PSD scheme. (c) Longitudinal cross section of the detector and the two fibers (signal and Cerenkov). Transversal (d) and longitudinal (e) view of the detector and the two fibers.

The main channel is placed side by side to another channel dedicated to Cerenkov radiation. Indeed, radiation fields can generate Cerenkov radiation in optical fibers [11] [23] [24]. This Cerenkov light represents a spurious signal that has to be subtracted from the PSD one. Cerenkov subtraction details and procedures are treated in Section 2.3.2.
This channel system is identical to the main one with the exception that it does not have an active volume, given that in this case the fiber directly collects the Cerenkov light. The two channels scheme is shown below [11].

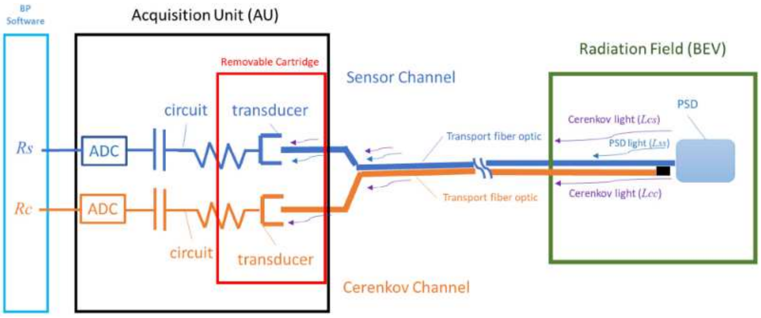

Figure 2.4: Double channel scheme of BP-PSD. The signals received by the BlueSoft software on the computer are labeled with R$_s$ and R$_c$ for "sensor" (the actual PSD signal) and Cerenkov respectively.

2.2.2 PTW microdiamond detector

Figure 2.5: PTW microdiamond detector.

The PTW[1] microdiamond detector (Figure 2.5) is a Single Crystal (synthetic) Diamond Detector (SCDD) that combines features from natural diamond detectors and silicon diode detectors.
It has a nominal sensitive volume of 0.004 mm^3, having a cylindrical shape with a radius of 1.1 mm and a thickness of 1 μm [25]. Its nominal response is 1 nC/Gy and does not require a bias voltage [9].
This type of detector shows some useful properties, such as [9]:

- A very high radiation hardness, which translates into higher stability and longer lifetime.
- Very low temperature dependence (<0.08%/K).
- Very low directional dependence (<1% for ± 40°).
- Low energy dependence.

Its operating principle is explained in the figure below.

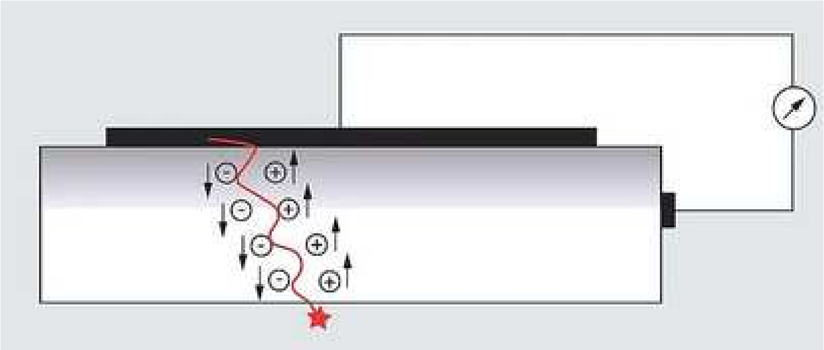

Figure 2.6: Functioning scheme of the PTW microdiamond detector [9]: a Schottky junction develops below the top metal contact. When passing through the active volume, the incident radiation produces positive and negative charges which are successively collected by the junction electric field, generating a current signal that can be measured with an electrometer.

---

[1] Its manufacturing house is *PTW-Freiburg*, a German company among the most prominent houses for projecting and production of medical physics equipments in the world.

The PTW microdiamond is suitable for small-field dosimetry too, having:

- Minimal dose per pulse or pulse repetition frequency dependence, so low dose rate dependence.
- Small response deviations in absorbed dose in water for fields up to 5 mm side.
- Good spatial resolution, which permits for instance to accurately measure OAR profiles, in particular regarding the penumbra regions.

2.2.3 IBA Razor diode

Figure 2.7: IBA Razor diode.

The IBA Razor diode (Figure 2.7) is a silicon detector based on a p-type silicon diode chip. Because of its characteristics, it is well suited for small-field dosimetry [3] [6] [7] [8] [21] [26].
The stem is made out of stainless steel, while the cap enclosing the detector is made of acrylonitrile butadiene styrene (ABS) plastic and epoxy resin [10] [26].
The silicon chip has a size of $0.95\times0.95\times0.4$ mm^3, with an active volume diameter of 0.6 mm and a thickness of 0.02 mm, which leads to a total active volume of approximately 0.006 mm^3. The head's diameter is 4 mm and it has a length of 15 mm. The stem has the same diameter but a length of 45 mm (for a total detector length of 60 mm). The actual detector measurement point does not stand on the top of the cap, but is located 0.8 ± 0.2 mm from the "surface" [10] [26].
Regarding the detector's performances, the IBA Razor diode presents the following features:

- It has a sensitivity of 4.1 nC/Gy (referring to the reference energy quality of ^{60}Co) [10] [26].
- Sensitivity varies with the total irradiation history of the detector depending on the energy quality. For our purposes, 6 MV photons lead to a sensitivity variation of 1%/KGy irradiated [10].
- The absolute deviation of a dose linearity fit from its endpoint remains in the $\pm0.2\%$ range, for a maximum of $\pm0.5\%$ (computed in a dose range between 0.02 and 40 Gy and referring again to ^{60}Co energy quality) [10] [26].

- The dose-per-pulse dependence typical range is ±0.5% for a maximum of ±1% (computed between 0.1 and 2.3 mGy/pulse, normalized at 0.4 mGy/pulse) [10] [21] [26].
- For energy dependence, absolute deviations in PDD measures compared with CC08 ionization chambers yield a typical deviation of 0.5% and a maximum of 1% (those measures are performed for a 5×5 cm^2 square field, 6 MV photon energy and 30 cm depth underwater) [10] [26].
- Sensitivity temperature dependence lies at 0.05%/°C for 15/40°C range [10] [26].
- The expected lifetime (measured in total dose to absorb before expiring) is $\geq$200 kGy (computed using 10 MeV electrons) [10] [26].

2.2.4 IBA EFD3G unshielded diode

Figure 2.8: IBA EFD3G unshielded diode.

IBA EFD3G (Figure 2.8) is an electron diode field detector that is normally used for measurements about electron beams in the 4-25 MeV energy range. Since the secondary charge particles produced during photon interaction with matter are actually electrons, this type of diode is also suitable for photon beam measurements.

Similarly to the IBA Razor detector, the stem of the EFD3G diode is made out of stainless steel, and the cap is made of ABS and epoxy resin. Moreover, even in this case the detector part is based on a p-doped silicon chip [10].

It has a chip size of $2.1\times2.1\times0.4$ mm^3, with an active volume diameter of 1.6 mm and a thickness of 0.08 mm, that gives a total volume of 0.16 mm^3. The actual detector measurement point is located 1.2±0.2 mm from the "surface" [10].

It is waterproof for underwater measurements and it doesn't need an operating voltage.

IBA EFD3G diode presents the following performance characteristics:

- Its sensitivity varies with the total irradiation history depending on the energy quality. In particular, for the 6 MV energy it presents a sensitivity variation $<$1%/250 Gy irradiated [10].
- Sensitivity has a typical variation with temperature of 0.25%/°C [10].
- Dose rate linearity goes up to 1% deviation in the 0.1-0.6 mGy/pulse range for WFF beams, while it rises to 3% at 1.0 mGy/pulse and 7% at 2.3 mGy/pulse for FFF beams [10].

2.2.5 Detectors summary

Here a summarizing table about the most important characteristics of the considered detectors is shown.

Detectors summary				
Characteristic	**BP PSD**	**PTW microdiamond**	**Razor diode**	**EFD3G diode**
Type	plastic scintillator	diamond	unshielded diode	unshielded diode
Active volume (mm^3)	0.785	0.004	0.006	0.16
Temperature dependence (%/°C)	n/a	<0.08	0.05	0.25
Dose per pulse dependence (%)	n/a	minimal	±0.5 to ±1	±1 WFF, ±3 to ±7 FFF
Application	any field size	any field size	small fields (<5×5 cm^2)	any field size

Table 2.1: Used detectors characteristics. Some BP PSD features regarding its dosimetric performances are yet unknown (indicated as "not available", n/a). Some pre-measure tests have been performed and discussed in Section 3.1.

2.3 Blue Physics PSD acquisition

BP-PSD dosimeter is not yet integrated with the water phantom acquisition system, so it was necessary to separately mount its instrumentation.

The plastic scintillator detector has been mounted onto the Blue Phantom 2 detector holder, and it was connected with the cartridge in the acquisition box through the transport optical fiber. The acquisition box was placed in the outer part of the radiotherapy bunker's maze in order not to risk irradiating the electronics. The cartridge was then connected to the computer with the BlueSoft software.

BP-PSD is sensible to light, and even visible-spectrum wavelengths could interfere with the measurements. It was then necessary to perform all measurements in darkness.

2.3.1 Detector alignment

Normally, the *My QA-accept* software that controls the water phantom system has an automatic program that aligns the isocenter (given by the detector (0,0) position) with the reference frame of the LINAC. This procedure is called CAX and consists in a series of four OARs distributions: two pairs of inline and crossline at two different depths. This way, calculating the center of the distributions it is possible to find the "detector isocenter" to then shift it back to the LINAC center, or even detect a possible tilt in the beamline direction and correct it by manually adjusting the angles of the water phantom movement system.

The BP-PSD detector has no way to be aligned through the usual procedure since it is not integrated with the phantom and thus the CAX protocol is not easily applicable. Therefore, for the alignment we resorted to a manual procedure that utilizes the BlueSoft software. For the crossline direction, the protocol was the following:

1. The detector is placed at (0,0,10) coordinates ((x,y,z) in cm, with the depth being positive because the z axis points down for positive values) and from the software live interface the corresponding signal value is marked with a cursor;
2. The detector is then moved in the crossline direction until a point having a measured signal almost equal to half the previous signal is reached. The signal value in this position is then marked with a cursor and the x coordinate is registered;
3. The detector is moved along the same direction but towards the opposite side in order to reach the specular point where the signal is equal to the value marked by the second cursor. Again, the x value of this point is registered;
4. The midpoint value between the two x coordinates is calculated, and it indicates the shift that has to be applied to the isocenter frame to coincide with the detector displacement.

This procedure was performed identically for the inline direction (obviously replacing x movements with y movements) and the center was then shifted of the found quantity.

This method works with a good accuracy even if the sought value is not precisely the half of the central value, but it brings in various sources of uncertainties, which will be discussed in Section 3.6.

2.3.2 ACR calibration

One of the major problems that arises when operating with plastic scintillator detectors coupled with optical fibers is the Cerenkov light. In fact, an optical fiber immersed in a radiation field produces a spurious signal that has to be subtracted from the effective signal.

The Cerenkov signal is modulated by a parameter called Adjacent Channel Ratio (ACR), which represents the ratio between the two adjacent channels: the total signal and the Cerenkov signal.

Cerenkov subraction follows the formula [11]:

$$S = R_s - ACR \times R_c \tag{2.1}$$

where S is the effective signal (proportional to the absorbed dose), R_s is the reading of the total signal channel and R_c is the reading of the Cerenkov channel.

To use Equation 2.1 for Cerenkov subtraction we need to have a method to calculate the ACR value.

In this work, we have adopted the FOF$_3$ method, which makes use of the field output factor for the 3×3 cm^2 field. Exploiting Equation 2.1 and the definition of FOF (Equation 3.5), it is indeed possible to construct an equation which gives the ACR value by knowing the field output factor:

$$FOF_3 = \frac{S_3}{S_{10}} = \frac{R_{s,3} - ACR \times R_{c,3}}{R_{s,10} - ACR \times R_{c,10}} \tag{2.2}$$

where all the instances denoted by the subscript "$_3$" refer to the 3×3 cm^2 square field, and the ones with "$_{10}$" to the 10×10 cm^2 square field.
Solving Equation 2.2 for ACR one obtains [11]:

$$ACR = \frac{FOF_3 \times R_{s,10} - R_{s,3}}{FOF_3 \times R_{c,10} - R_{c,3}} \tag{2.3}$$

2.3.3 Measurement procedure

For the PDDs and OARs acquisitions with the BP-PSD, the detector movement and the actual data registration are separated. The operator has thus to perform the following actions, in sequence:

1. Start the time acquisition of the scintillator from the BlueSoft software.
2. Turn on LINAC beam delivery.
3. Start the movement of the water phantom holder.

To stop the measurement, the components are shut off in the opposite order. This whole process brings in some spurious signals, in conjunction with some measurement uncertainties. The formers will be removed during raw data analysis (Section 3.2) while the latter are discussed in Section 3.6.
The acquisition of the various distributions is performed with a scanning speed of 10 mm/s with the continuous modality, so the detector holder smoothly moves across the phantom in the predetermined direction with fixed speed while the acquisition system collects the data. This fact will be used for the time-space conversion of the PDD and OAR raw data during the analysis.
For FOF measures, the process is the following:

1. The detector is placed at the right position using the water phantom movement system.
2. The acquisition gets started from the BlueSoft software.
3. Beam delivery is turned on.
4. After the predetermined dose has been dispensed, the LINAC automatically turns off the beam.

At this point, a new measure can be taken by repeating the process after changing the field size, without having to reset the BP-PSD acquisition. This way, all the FOF data are collected into the same BlueSoft file. The effective data value is calculated directly by the software as the integral of the obtained time distributions.

The following images depict the "paths" that the detector follows while acquiring a PDD or an OAR measurement, and also provide an idea of the localization of the measurements point for FOF acquisitions. These considerations are valid also for the other detectors acquisitions.

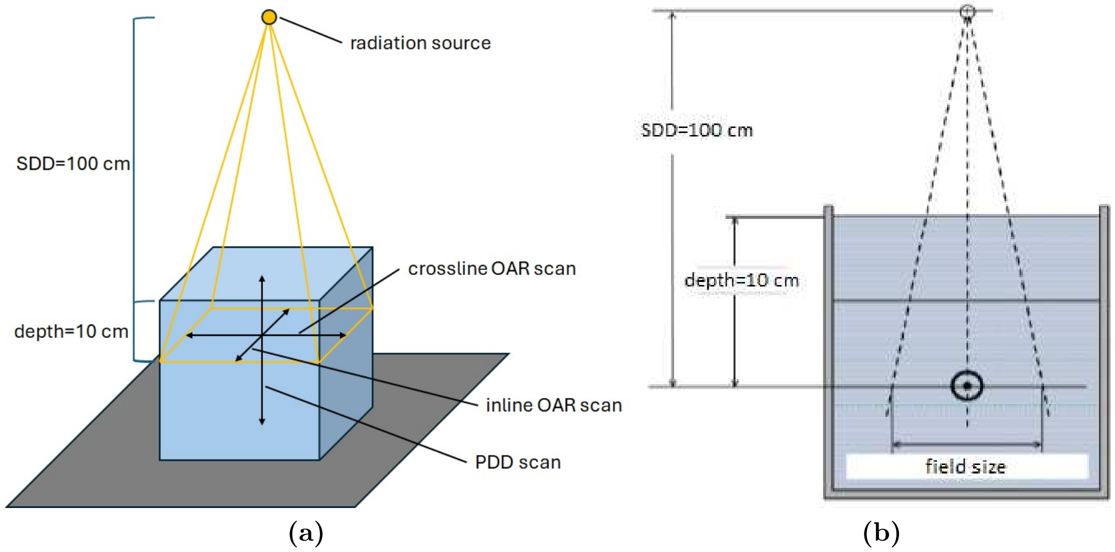

(a) (b)

Figure 2.9: Figure (a) shows the scan directions for PDD and OAR acquisitions, while Figure (b) shows the FOF acquisition point position (the marked circle). The depicted setups refer to our reference conditions.

2.4 Other detectors acquisition

2.4.1 Detectors alignment

The measurements setup for all the detectors but the BP-PSD follows a simpler scheme. As previously mentioned, those detectors acquire data leaning on the water phantom acquisition and movement system, which is connected to the acquisition *My QA-accept* software outside the radiotherapy bunker. For this reason the setup of these three detectors is similar, and consists of two main passages:

1. The chosen detector is placed onto the water phantom holder, and a first alignment is performed. x/y centering cannot be done rigorously in this phase, while for the z alignment a cap signed at the sensible volume level is used: the cap is placed to cover the detector head, and the detector holder is then lifted up or down until the mark is seen to match the water level. Then, with the "set isocenter" command the operator fixes that point as the z=0 position.

2. The crossline/inline alignment exploits the CAX premade protocol: a set of two inline and two crossline OAR measurements at different depths is collected, then the program computes the centroids of those distributions. From these points it suggests the necessary (x,y) shift to align the (0,0) central point with the isocenter, as well as the tilt angles that should be applied to the water phantom movement rail in the two planar directions. Once the operator corrects for these factors, a new CAX is performed, until

the correction values for the centroid and the angles are found to be within a confidence range.

2.5 Measurement procedure

The scan measures acquired with the microdiamond detector follow the same modality as the BP-PSD ones, so they are collected using a continuous movement modality at a fixed acquisition rate.
For the IBA Razor diode and the EFD3G unshielded diode, a "step-and-shoot" modality has been chosen instead. The detector holder moves one step at a time, and after each displacement the detector acquires a measurement point. In this way, it is also possible to change the density of points depending on the distribution zone, so that the regions of interest contain more points than the others.
Regarding the two diodes and the microdiamond detector there is no need to manually start both the acquisition and the holder movement, since the phantom software integrates all these functionalities together, so starting the acquisition automatically starts the detector movement too. Anyway, the beam delivery must be manually turned on and off before and after the acquisition time window.
FOF measurements for these three latter detectors is done using an external electrometer. The water phantom software does not come into play for these measures, as the acquisition is started and stopped directly from the electrometer. Each time, the beam delivery is manually turned on, and after the specified dose gets dispensed and the beam turns off the collected charge is registered onto a separate file, then the electrometer gets reset and the next measure can be performed.

2.6 Measures list

The list of measures acquired is subdivided into the following three tables, categorized by the used detector, the energy of the beam, the field size and other specific parameters.

PDD measures list		
Detector	**Energies (MV)**	**Field sizes (cm×cm^2)**
BP PSD	6 WFF, 6 FFF	small: 0.6×0.6, 1×1, 2×2, 3×3 standard: 5×5, 10×10, 30×30
PTW microdiamond	6 WFF, 6 FFF	small: 0.6×0.6, 1×1, 2×2, 3×3 standard: 5×5, 10×10, 30×30
Razor diode	6 WFF, 6 FFF	small: 0.6×0.6, 1×1, 2×2, 3×3 standard: 10×10
EFD3G diode	6 WFF, 6 FFF	small: 0.6×0.6, 1×1, 2×2, 3×3 standard: 5×5, 10×10

Table 2.2: PDDs measures list. These measurements have been performed keeping x and y coordinates equal to 0 (so on the central axis of the radiation beam) and with a SSD of 90 cm.

OAR measures list			
Detector	**Energies (MV)**	**Direction**	**Field sizes (cm×cm^2)**
BP PSD	6 WFF, 6 FFF	Crossline, inline	small: 0.6×0.6, 1×1, 2×2, 3×3 standard: 5×5, 10×10, 30×30
PTW microdiamond	6 WFF, 6 FFF	Crossline, inline	small: 0.6×0.6, 1×1, 2×2, 3×3 standard: 5×5, 10×10, 30×30
Razor diode	6 WFF, 6 FFF	Crossline, inline	small: 0.6×0.6, 1×1, 2×2, 3×3
EFD3G diode	6 WFF, 6 FFF	Crossline, inline	small: 0.6×0.6, 1×1, 2×2, 3×3

Table 2.3: OARs measures list. Crossline OARs have x varying and y set to 0, and viceversa for inline ones. The depth for the acquisition is 10 cm. SSD is set to 90 cm.

FOF measures list		
Detector	**Energies (MV)**	**Field sizes (cm×cm^2)**
BP PSD	6 WFF, 6 FFF	small: 0.6×0.6, 1×1, 2×2, 3×3 standard: 5×5
PTW microdiamond	6 WFF, 6 FFF	small: 0.6×0.6, 1×1, 2×2, 3×3 standard: 5×5
Razor diode	6 WFF, 6 FFF	small: 0.6×0.6, 1×1, 2×2, 3×3 standard: 5×5
EFD3G diode	6 WFF, 6 FFF	small: 0.6×0.6, 1×1, 2×2, 3×3 standard: 5×5

Table 2.4: FOFs measures list. To acquire them, the detector has been positioned at x=y=0 and 10 cm underwater. The SSD is 90 cm. The delivered dose is 100 MU. Each measure has been repeated four times, and their arithmetic mean has been kept as the result.

The choice made for the field sizes in each case reflects the suitability of the detectors to be used with small fields. In facts, the PTW microdiamond and the IBA Razor diode are particularly befitting for small field dosimetry. Notably, field size has been kept small for each of the Razor diode measure.

We point out that the BP-PSD datasets about the PDD of the 30×30 cm^2 field FFF and the inline OAR of the same field size WFF had to be discarded, so are not going to be presented. Indeed, the former had a problem of saturation due to FFF beam higher dose rate, while for the latter an issue about background subtraction has been encountered. Those two problems will be discussed in Section 3.4 and in the conclusions.

Chapter 3

Data analysis and results

In this Chapter we will discuss about the results obtained by the analysis conducted for each considered detector, and the comparisons between them. In particular, the BP-PSD analysis follows a different route with respect to the other detectors' one, since the acquisition apparatus is not integrated with the water phantom system and thus it is impossible to perform the same refinements using the *My QA-accept* analysis software integrated with the water phantom.
Before the actual analysis, for BP-PSD some preliminary tests have been conducted.

3.1 BP-PSD dose linearity and dose rate stability

A dose linearity test and a dose rate stability test have been carried out for both 6 MV WFF and 6 MV FFF beam energies.
For the dose linearity test, the detector was placed along the central axis of the field (through the alignment procedure described in Section 2.3.1), at a depth of 10 cm and with an SSD of 90 cm. Then, the detector was exposed to increasingly higher dose by modifying the total MU parameter in the beam delivery control system. The chosen MU values delivered are: 1, 2, 3, 4, 5, 10, 20, 30, 50, 100, 200, 300, 500, 700, 800, 1000, 2000 MU.
The ACR value for those measurements was calculated with the FOF_3 procedure described in Section 2.3.2 and it was found to be equal to 0.845 for the WFF energy and 0.844 for the FFF energy.
Dose rate was left unbounded, so 476 MU/min for WFF energy and 1359 MU/min for FFF energy.
Results are represented in Figures 3.1 and 3.2, respectively for the WFF and FFF beam energies. For each energy a linear fit was performed, and to test the goodness of the fit an R^2 value was calculated. For both energies, values very close to 1 were found (equal to 1 up to a difference of the order of 10^{-5}), so we can conclude that the response of the detector with respect to the delivered dose is indeed linear.

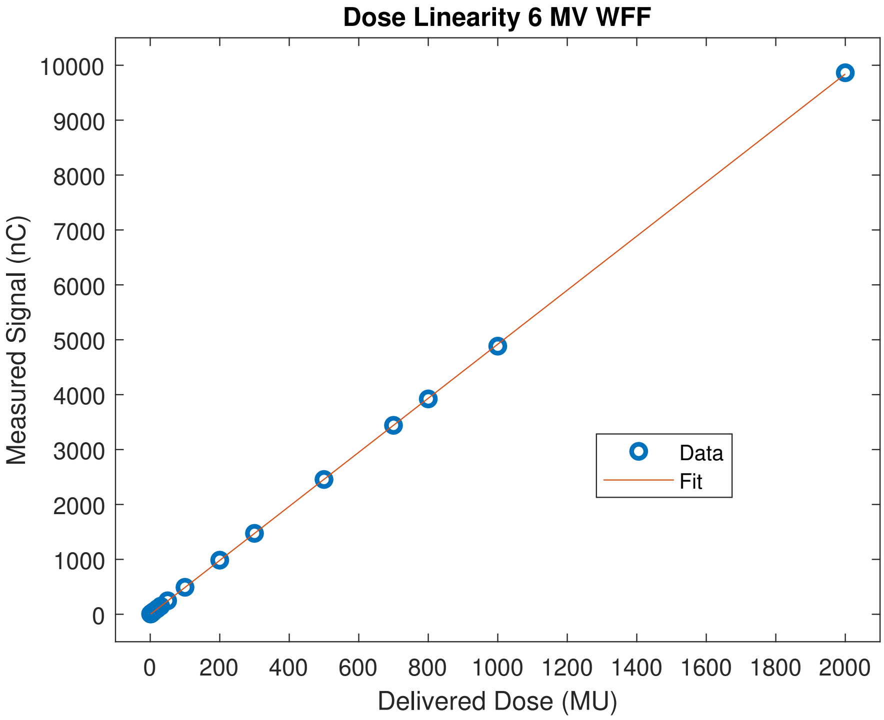

Figure 3.1: Signal measured with the BP-PSD detector, as a function of the delivered MU, and linear fit for 6 MV WFF beam energy.

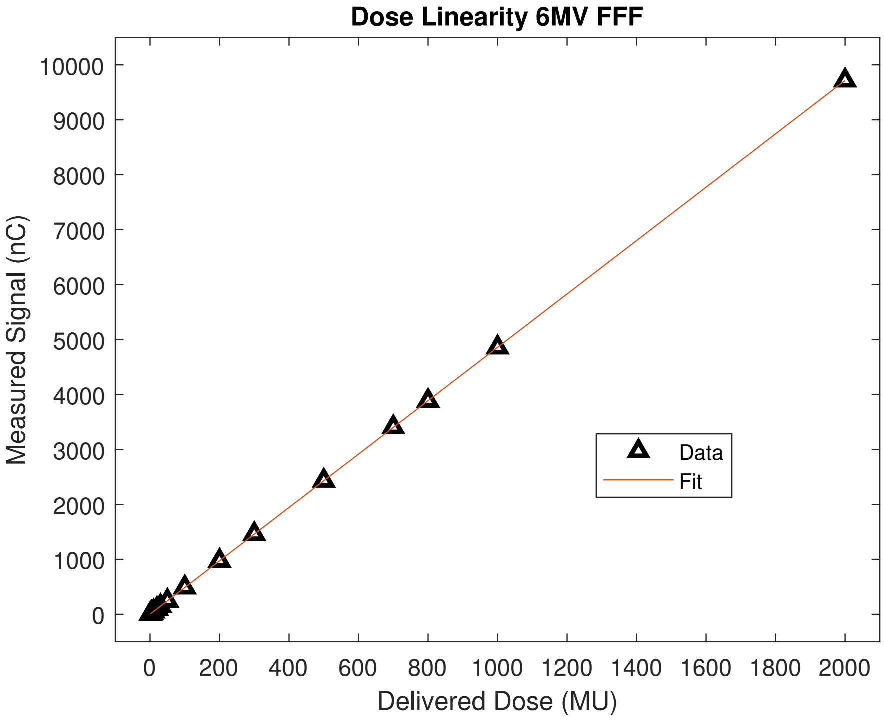

Figure 3.2: Signal measured with the BP-PSD detector, as a function of the delivered MU, and linear fit for 6 MV FFF beam energy.

Also, to obtain a comparison with the preexisting literature [11] [12], the signal of each point has been normalized at the corresponding MU value, and then the obtained data has been further normalized to the value corresponding to 100 MU. The results are plotted in Figure 3.3.

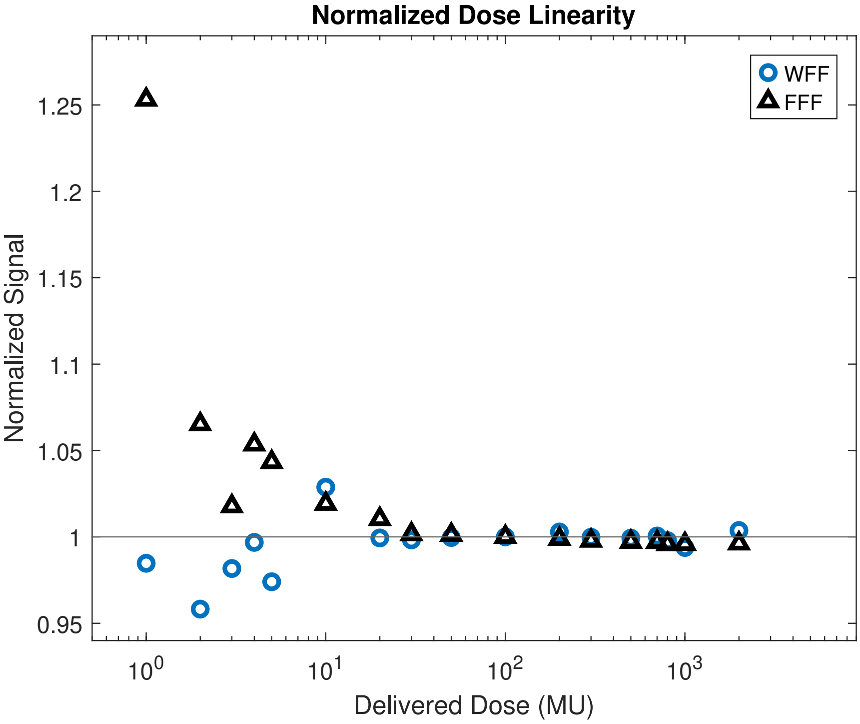

Figure 3.3: Normalized dose signals. The marked gray line corresponds to the height of the point at 100 MU. The abscissa scale is logarithmic.

As can be seen, the results are in agreement with what was obtained by *I.Das et al.* [11] reflecting in particular the behavior at lower delivered dose. In fact, the left-most part of the graph presents the largest deviations, with an average of the order of 1.04-1.05 times the reference value. FFF beam is the most divergent one of the two, with its lowest MU point being particularly far away from the others.

For the dose rate stability test, the detector was again placed along the central axis of the field exploiting the alignment procedure described in Section 2.3.1, at a depth of 10 cm and with a SSD of 90 cm. A fixed dose of 100 MU has been administered, progressively increasing the dose rate. Considering how the LINAC beam control system works, there is no way to precisely choose some specific dose rate values, since the LINAC is able to output only discrete "packets" of dose. Some nominal values have then been set, ranging from the minimum acceptable (around 50 MU/min for WFF and 100 MU/min for FFF) to the maximum supported (around 500 MU/min for WFF and 1400 MU/min for FFF). The effective values that the system was able to deliver are: 46, 93, 138, 183, 231, 281, 333, 383, 430, 473 MU/min for 6 MV WFF energy; 90, 190, 280, 380, 480, 680, 960, 1150, 1380 MU/min for 6 MV FFF energy.
The ACR was the same used for the dose linearity test, so 0.845 and 0.844 for 6 MV WFF and FFF respectively.
The obtained signals (in nC) have been normalized to the signals coming from the maximum dose rate of each beam energy, which in our case are 500 MU/min for WFF beam and 1400 MU/min for FFF beam (those are the nominal values, while

the effective values are respectively 473 MU/min and 1380 MU/min). Figure 3.4 shows the results.

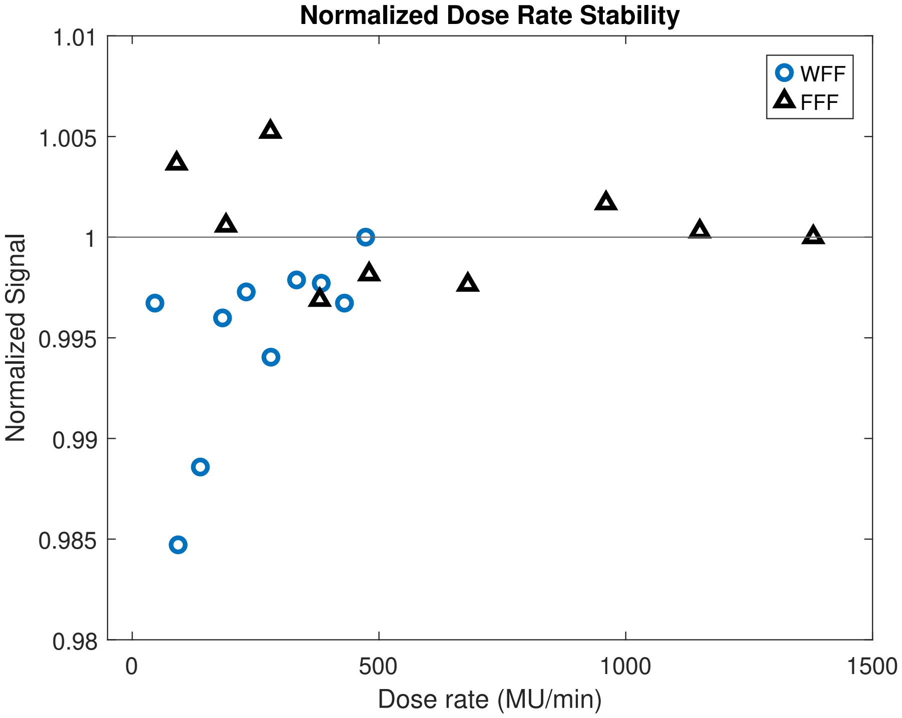

Figure 3.4: Normalized dose signal obtained with different dose rates. The marked gray line corresponds to the height of the points at 500 MU/min for WFF beam and 1400 MU/min for FFF beam (nominal values).

Even for the dose rate stability test, our data were similar to the ones reported in the literature, with a dispersion within a 1.5% range [11] [12]. The major deviations were found for WFF beam at lower dose rates, but, on the contrary of what was obtained by *I.Das et al.* [11], the bias tends to negative differences with respect to the references.

3.2 BP-PSD post processing

BP-PSD is not yet integrated with the *My QA-accept* software, but it is equipped with the BlueSoft software. However, at the moment it is not available in a certified version capable of running a precise analysis of the raw data, besides the FOF and the ACR calculations. Then, within the scope of this thesis, a dedicated software was designed to reconstruct and analyze all the PDDs and OARs distributions from the collected data. To do that, a MATLAB script has been developed. This program consists in a series of steps that follow a list of operations to overcome some issues about the initial data and reconstruct the PDDs or the OARs. The main demands can be resumed as follows:

- **Data integration.** The time resolution of the scintillator is really high, up to being able to distinguish the single pulses of the LINAC. An example is depicted in Figure 3.5. This feature is useful to collect a large amount of information, but on the other hand it is also very prone to collect noise and background spurious signal. Therefore, without a rebinning it is impossible to properly recognize the real shape of the dosimetric distributions acquired. Data integration is thus advisable.

- **Time-space domain conversion**. BP-PSD registers data in the time domain, while the dosimetry distributions are expected to be functions of the space coordinates (in fact, PDDs consist in the energy dose deposition distribution along the z direction, while OAR along the x or y directions). A coordinate transformation is necessary.

- **Interval definition.** Since BP-PSD is not yet integrated with the water phantom system, the measurements acquisitions have to be started and stopped manually, without an automatic mechanism. In this way, the acquisition includes a time window which is larger than the effective scanning time window of the movement apparatus. From the resulting curve is then necessary to crop the real data, removing the undesired ones.

- **Smoothing and normalization.** To be able to compare the curves between the detectors, a normalization is needed. Moreover, to further refine the shape of those curves, a smoothing algorithm can be applied.

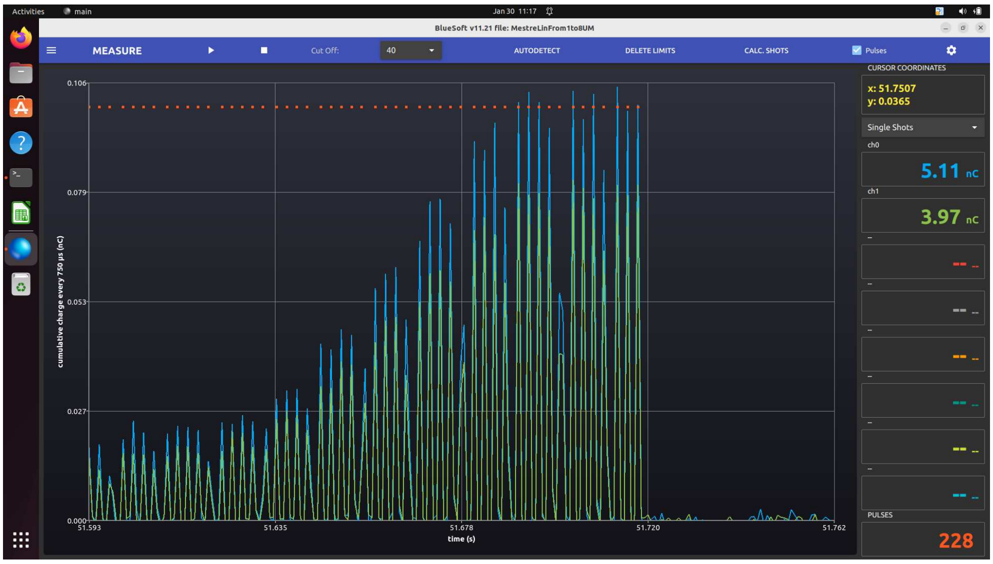

Cut Off: 40

CURSOR COORDINATES
x: 51.7507
y: 0.0365

Single Shots

ch0 5.11 nC

ch1 3.97 nC

PULSES 228

Figure 3.5: Screenshot of the acquisition software (BlueSoft) on the computer. Here a single MU is detected, which is the minimum unit dose that a LINAC can deliver. The scintillator is even able to recognize the pulses which the accelerator builds up the MU with. The different colors in the graph represent the two channels (signal and Cerenkov, respectively in blue and green).

We will go into deep details about all the steps executed by the program, leading to PDD/OAR extraction. We will first describe the procedure for PDD; the one for OAR is similar, with small differences that will be highlighted later.

3.2.1 Integration

The raw PDD data coming directly from the acquisition software appear as in Figure 3.6. The first "descending phase" of that curve is a spurious signal coming from the detector holder movement to get in place to start the acquisition, and as previously mentioned the time window of the acquisition has to include those kind of signals that will eventually be removed.

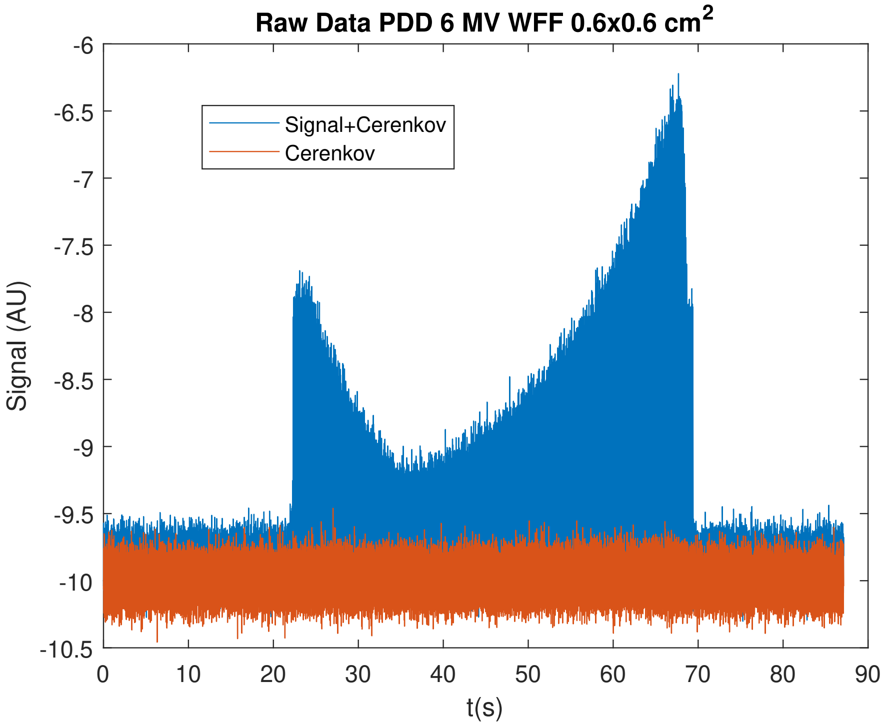

Figure 3.6: Raw data from a PDD acquisition with 0.6×0.6 cm^2 field and 6 MV WFF energy. The colors represent the total signal (real signal+Cerenkov) and the Cerenkov signal. The curves appear as "filled" since there isn't enough graphical resolution to see all the pulses.

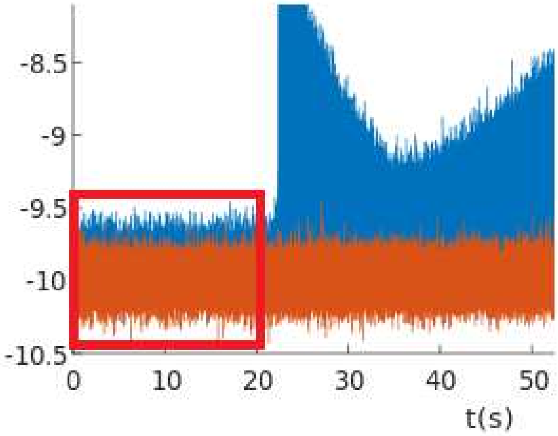

Figure 3.7: Background detail for the same data of Figure 3.6. The time window chosen is located before the irradiation to avoid any leftover noise.

The first step to be performed by the software is the background subtraction. The acquisition unit registers the signals starting from a basal negative value in voltage (which depends on the settings of the acquisition unit capacitors) and goes up or down, up to a maximum and a minimum voltage. In order to be able to rescale and normalize the distribution properly we need to set the baseline value. To do that, we consider a time window where the main signal is not present (for example the one highlighted in Figure 3.7); we calculate the real signal using Equation 2.1; we sum all of those values performing an average over the selected time interval. By doing this we obtain a good approximation of the acquisition unit baseline. Each raw data point is then calibrated using the ACR and shifted by the calculated baseline.
Now we can integrate the whole dataset to obtain the curve shape. The integration is guided by an algorithm that works as follows:

1. The total time interval is subdivided into three main integration windows, which cover the tail of the PDD, the hill around its maximum and the steep rise at low depths. This is done since the number of points differs from zone to zone, in the sense that, in the end, the steeper parts of the graph will have a lower "density" of points compared to flatter ones. This happens because the scanning speed of the phantom detector holder is kept constant during the acquisitions with the BP PSD, with a value of 10 mm/s. This effect is counterbalanced by choosing a different integration step for each window.

2. For each window, an integration width w and an integration step s are chosen. Each of them is counted in i units, which is the index on the raw data vector corresponding to each point in the raw curve. The conversion between the i index and the time coordinate is performed using the simple formula:
$$t_i = 776 \cdot i \ \mu s \tag{3.1}$$
where 776 μs is the used time resolution step of the BP-PSD.

3. The algorithm starts at a point p having an index i equal to $i_0 = w/2$ and is programmed to stop after reaching a point having an index equal at least to $i_T - w/2$, where i_T is the i index value corresponding to the last acquired point. At each step, the algorithm sums all the ordinate values having an index i included in the interval $[i_0 - w/2;\ i_0 + w/2]$, divides the result by $w + 1$ (to account for the central point, too) and then assigns the result to a bin centered at i_0 (and its corresponding time). Then, shifts the i_0 value to $i_0 + s$ and computes a new integrated point, restarting the cycle.
In this way, there is the possibility to modify both the width of the integral windows and the step between them accordingly to the zone of the distribution. If s is chosen to be $< w$, the windows actually overlap. This is the choice that has been made, because thanks to this we are able to preserve a large enough number of points without the need of a small integration window. In fact, performing an integration having $s = w$ (so the integration windows are exactly adjacent and cover each point just once) we wouldn't have overlapping windows, but the resulting number of points would be connected with w (the higher w, the smaller the number of points)

and sometimes the integration width would need to be too large in order to obtain an adequate damping of the oscillations collected by the BP PSD (due to its high time resolution) resulting in very few points in the final PDD/OAR. This problem is present in particular with the OARs of smaller fields, since their distribution is already composed by a small amount of points, and it is characterized by steep rises and falls (as seen in Section 1.4 the plateau in the middle of the profile disappears).
Anyway, the choice of keeping $s < w$ links each final point with its neighbors in term of information, but does not lose it.

After this process, the dataset takes the appearance of the following graph.

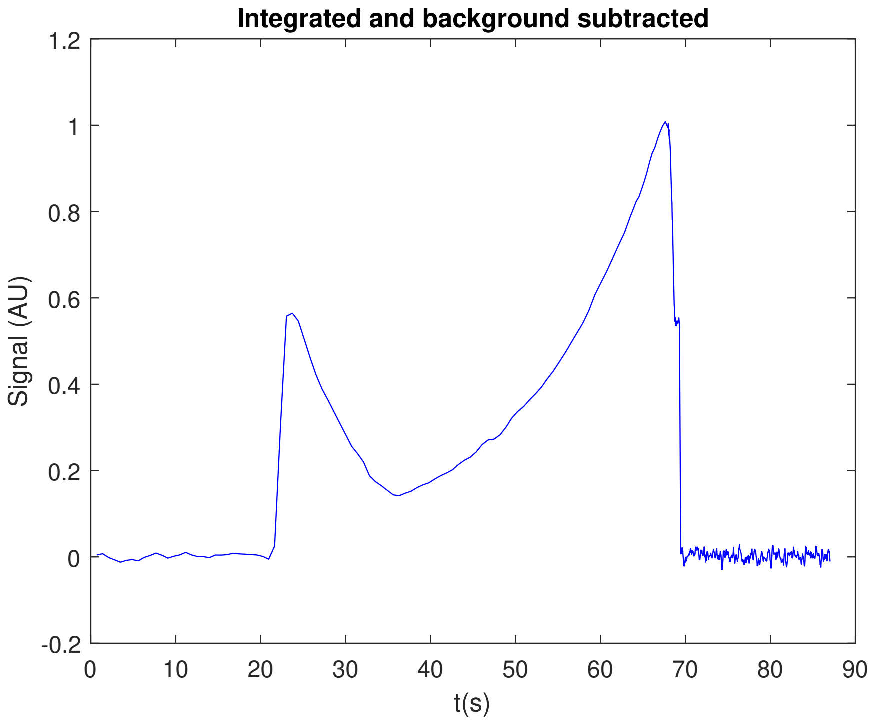

Figure 3.8: Integrated and background subtracted data from a PDD acquisition with 0.6×0.6 cm^2 field and 6 MV WFF energy.

3.2.2 Time-space domain conversion and interval definition

The next passage consists in extracting the real curve and converting it to the space domain. Moreover, since the acquisition system starts the scanning from the bottom of the phantom and goes upwards, the resulting PDD is reversed with respect to the z coordinate, so it has to be mirrored.
The reference point that is used as the start of the distribution (having z=0) is the tilt that appears at the last fall of the curve (see the detail in Figure 3.9). That happens because at the end of the acquisition run the detector holder slightly emerges from the water surface, producing a spurious signal before the irradiation gets shut off. That does not represent a rigorous reference point, but it is the only point that we can base on to reconstruct the acquisition time window, other than the d_{max} point.

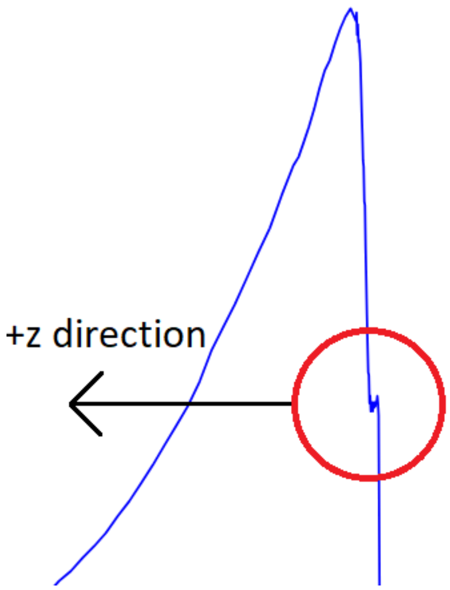

Figure 3.9: Tilt detail from the integrated curve. Starting from there, the spatial curve is reconstructed by having the positive depth direction running as indicated.

A post-alignment can be performed referring to the maximum point, trying to align the BP-PSD PDD d_{max} with the microdiamond one. Actually, the method that has been chosen to improve the starting point alignment is the trial of various z=0 points in the tilt area marked in Figure 3.9. Among the found z values, we kept the one that leads to a smaller percent difference with microdiamond in the rise region, since it is the region which is the most affected by abscissa misalignment (see Section 3.4).

Setting to 0 the abscissa value z_0 of this point before the tilt, the new abscissa z_t of a point that previously had a time abscissa t is found using the formula:

$$z_t = 10 \cdot (t_0 - t) \quad [mm] \tag{3.2}$$

where t_0 is the time abscissa corresponding to the z_0 point and 10 mm/s is the scanning speed. Since from the water phantom movement system we know that the total scan length is L ~320 mm, the curve is cut between $[t_0 - L/10;\ t_0]$ and converted into a new curve having borders $[0;\ L]$.

The result after this step is shown in Figure 3.10.

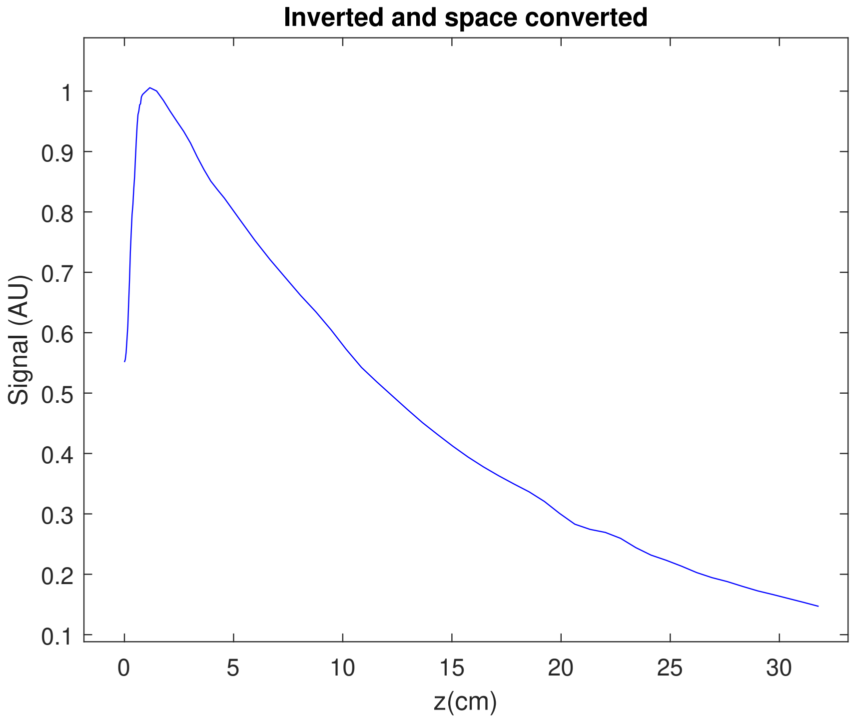

Figure 3.10: Inverted and space converted data from a PDD acquisition with 0.6×0.6 cm^2 field and 6 MV WFF energy.

3.2.3 Smoothing and normalization

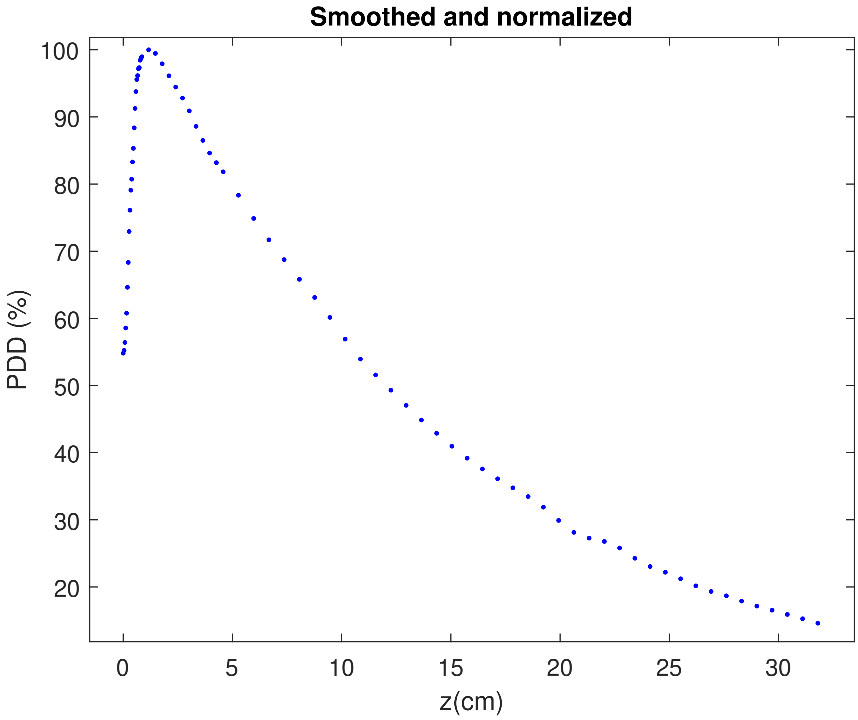

Figure 3.11: Final PDD data (after smoothing and normalization) from an acquisition with 6×6 mm^2 field and 6 MV WFF energy.

The last procedures to be performed are the smooth and the normalization.
The smoothing follows a local least square algorithm and can be tuned to fit locally to a polynomial of various degrees. In our case, a two degree polynomial is found to be effective. Smoothing helps removing leftover "oscillations" and permits to reach a distribution shape that can be compared with the other detectors' data.
The normalization step is performed setting the maximum value at 100% and all other points in percentage with respect to it.
The final result is shown in Figure 3.11.

The raw analysis process followed for OARs is very similar to the one just described for PDDs, but in this case space inversion is not necessary and the reference point for both space conversion and normalization is the central point of the distribution. Moreover, five integration windows instead of three are set, which correspond to: the left tails, the left rise, the plateau, the right fall and the right tails. Actually, the integration parameters of the baseline zones are chosen the same for both left and right, and this is also true for the left rise and the right fall zones.

3.3 Other detectors post processing

In the case of the microdiamond detector, the IBA Razor diode and the IBA EFD3G unshielded diode, the post processing data refinement can be executed with the support of the *My QA-accept* analysis software, leading to a much simpler procedure. The following two operations[1] have been carried out:

1. The curve gets smoothed by an algorithm present in the *My QA-accept* software;
2. The final distribution is obtained with a normalization (to the maximum point for PDD and to the central one for OAR).

3.4 Detectors PDD and OAR comparison

3.4.1 Percentage Depth Doses results

Here are reported some examples of comparisons between the four detectors' results for PDD distributions. The ones depicted are just illustrative to some properties that are found to be common to all the PDDs analyzed. Those three cases (1×1, 3×3, 10×10 cm^2 fields) are taken as they are representatives of very small fields, small fields and standard fields.
To have a deeper understanding of the differences that are present among the PDDs measured by the different detectors, a graph of percent gaps has been plotted for each case too, keeping the microdiamond curve as the reference, since it is considered as the most reliable detector in every analyzed situation.

---

[1] For microdiamond only, more than one set of measurements was available, since multiple sets have been acquired for other purposes. Then, as an additional passage, the mean among the curves of each set has been performed.

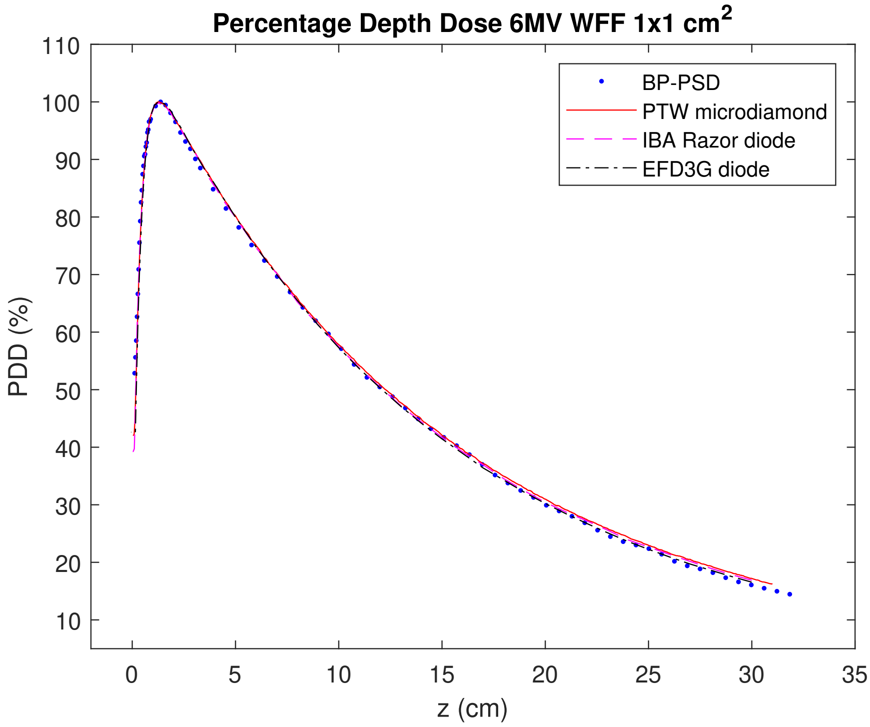

Figure 3.12: PDD comparison of the four detectors for a 1×1 cm^2 square field, with 6 MV WFF energy.

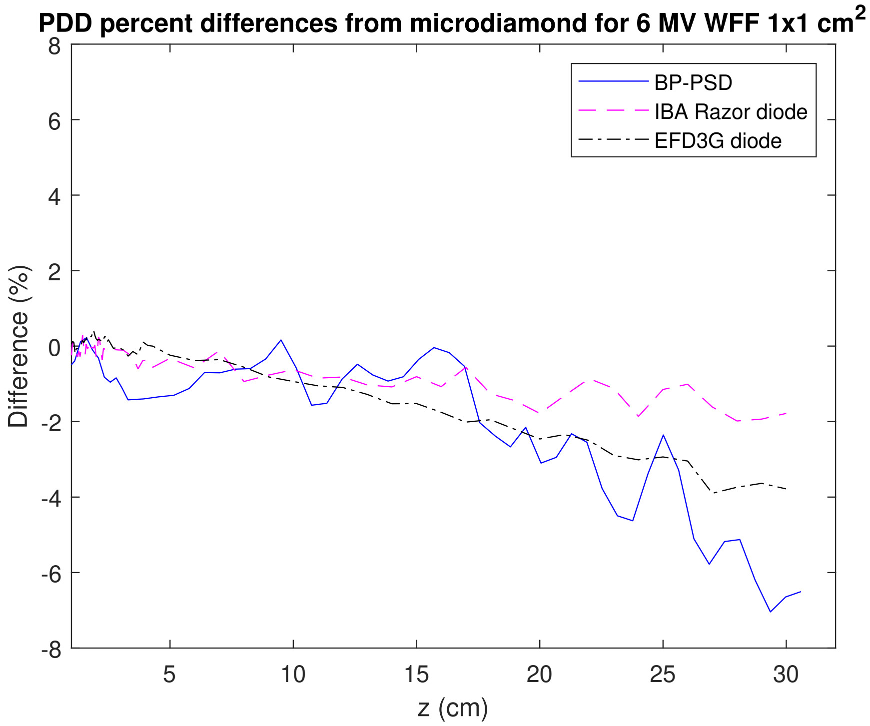

Figure 3.13: Percent differences between each detector PDD output and the microdiamond detector for a 1×1 cm^2 square field, with 6 MV WFF energy.

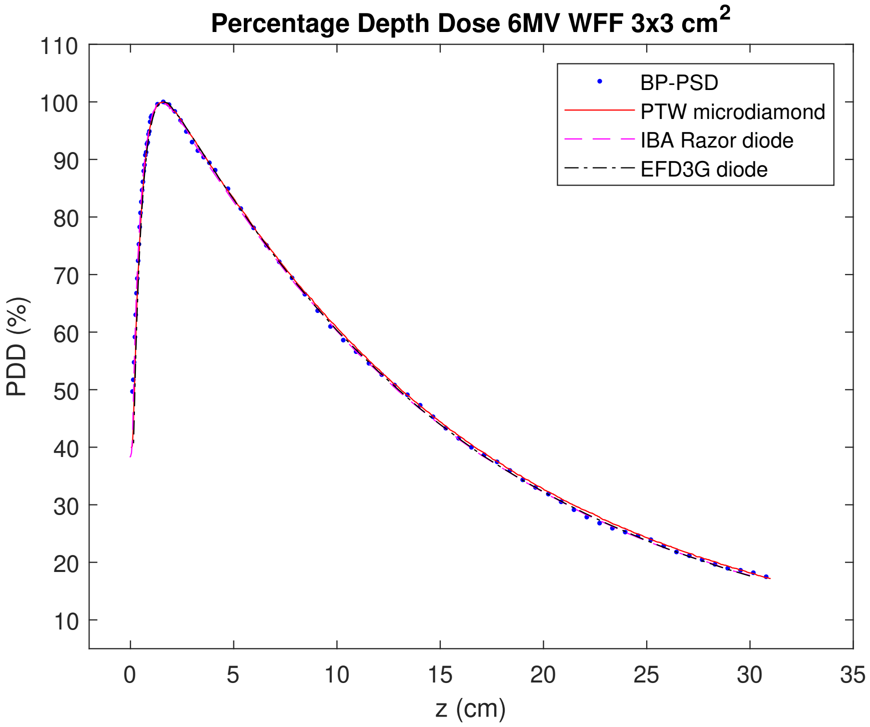

Figure 3.14: PDD comparison of the four detectors for a 3×3 cm^2 square field, with 6 MV WFF energy.

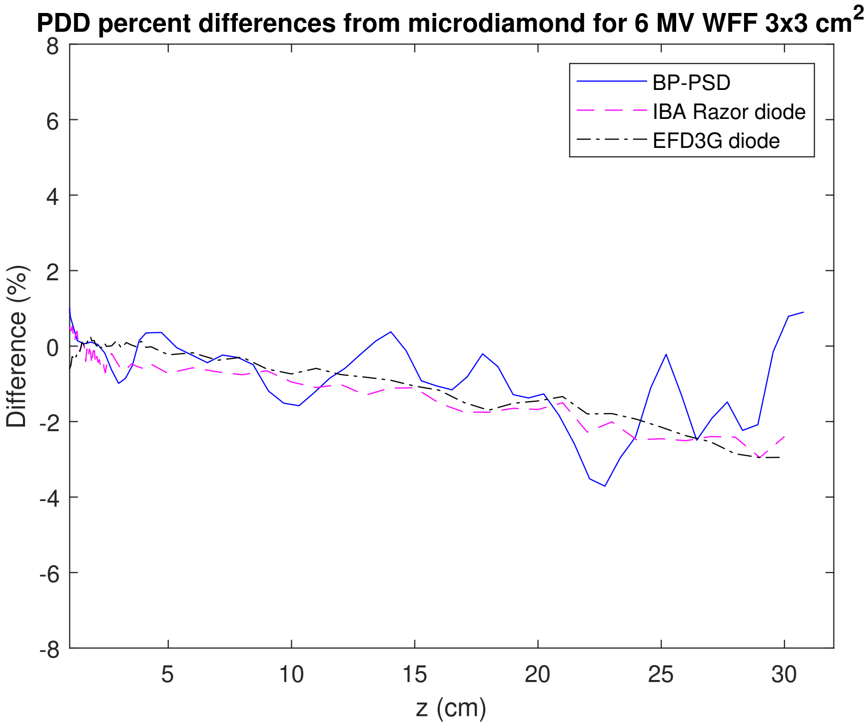

Figure 3.15: Percent differences between each detector PDD output and the microdiamond detector for a 3×3 cm^2 square field, with 6 MV WFF energy.

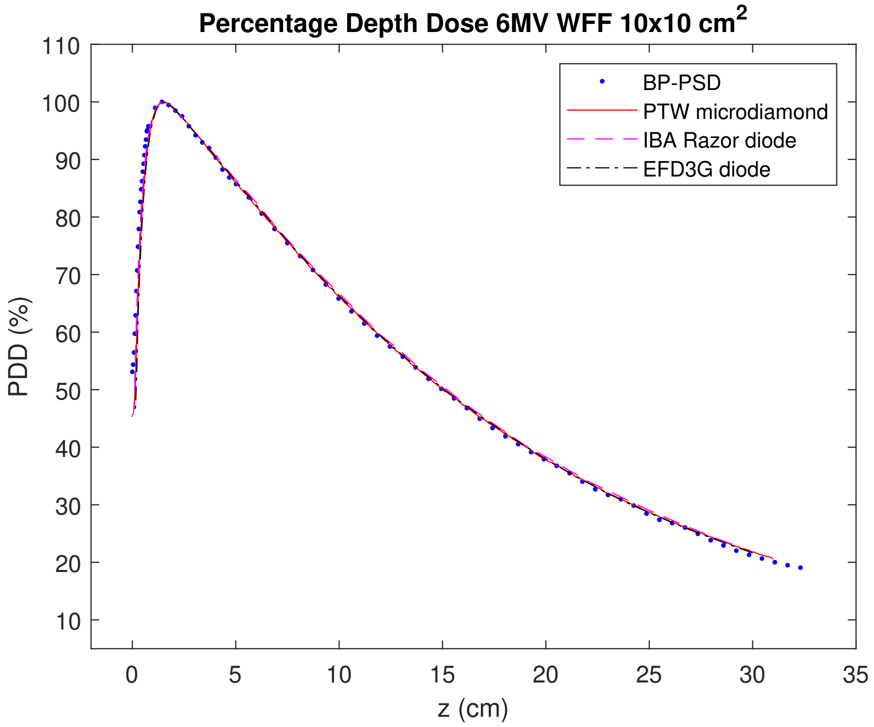

Figure 3.16: PDD comparison of the four detectors for a 10×10 cm^2 square field, with 6 MV WFF energy.

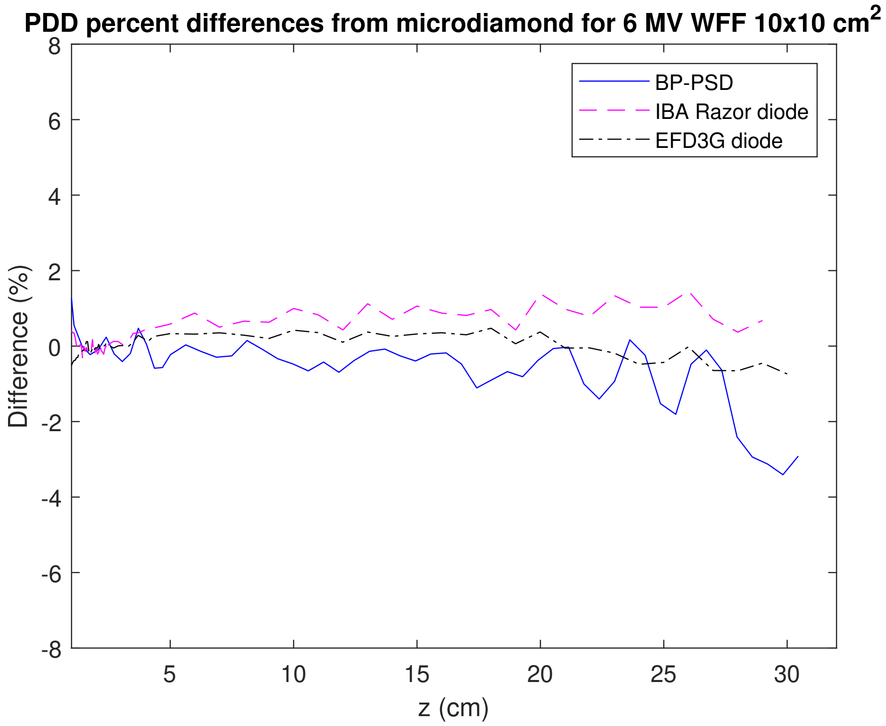

Figure 3.17: Percent differences between each detector PDD output and the microdiamond detector for a 10×10 cm^2 square field, with 6 MV WFF energy.

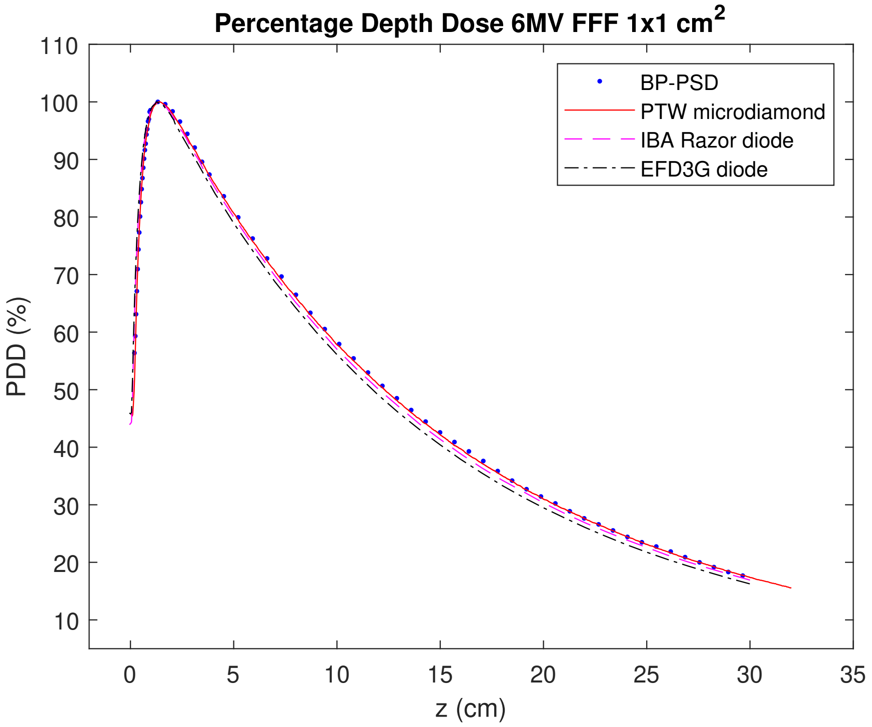

Figure 3.18: PDD comparison of the four detectors for a 1×1 cm^2 square field, with 6 MV FFF energy.

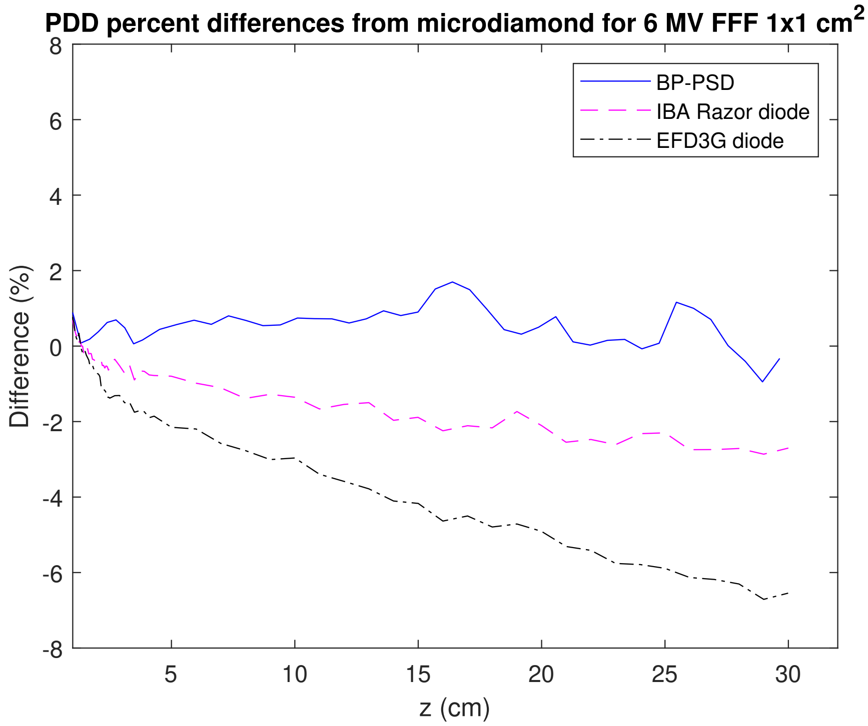

Figure 3.19: Percent differences between each detector PDD output and the microdiamond detector for a 1×1 cm^2 square field, with 6 MV FFF energy.

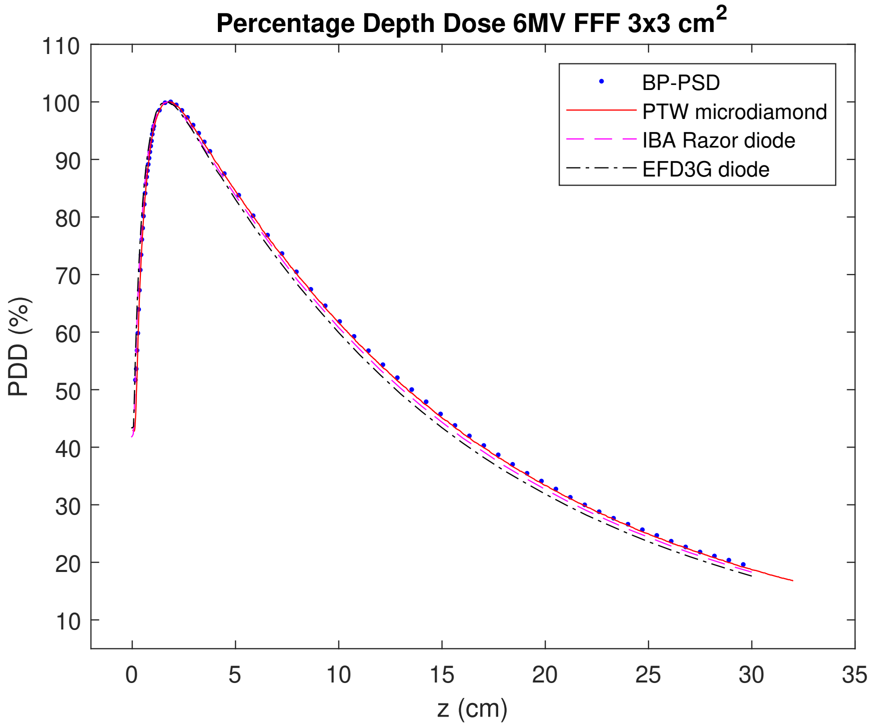

Figure 3.20: PDD comparison of the four detectors for a 3×3 cm^2 square field, with 6 MV FFF energy.

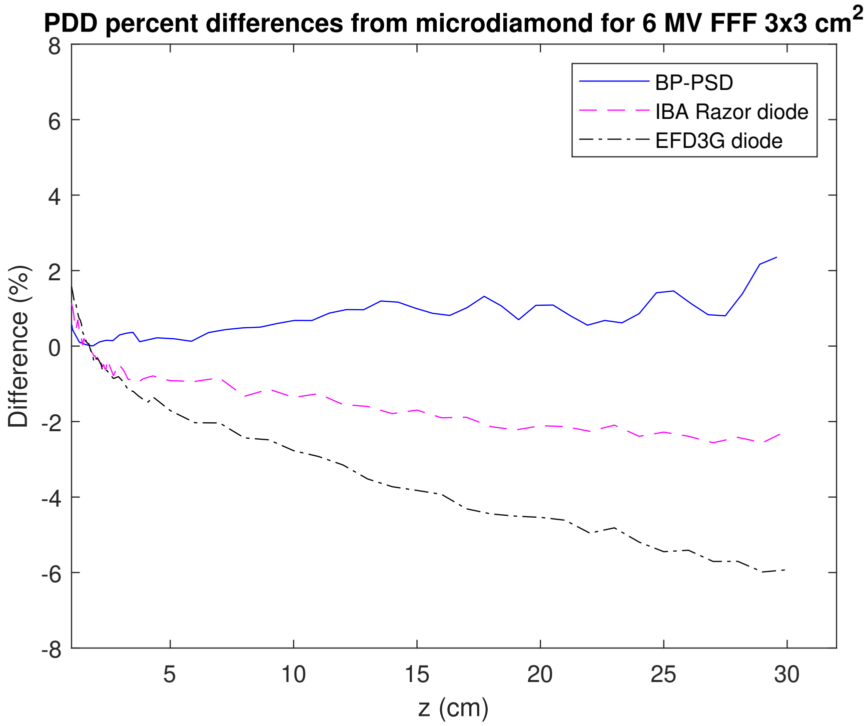

Figure 3.21: Percent differences between each detector PDD output and the microdiamond detector for a 3×3 cm^2 square field, with 6 MV FFF energy.

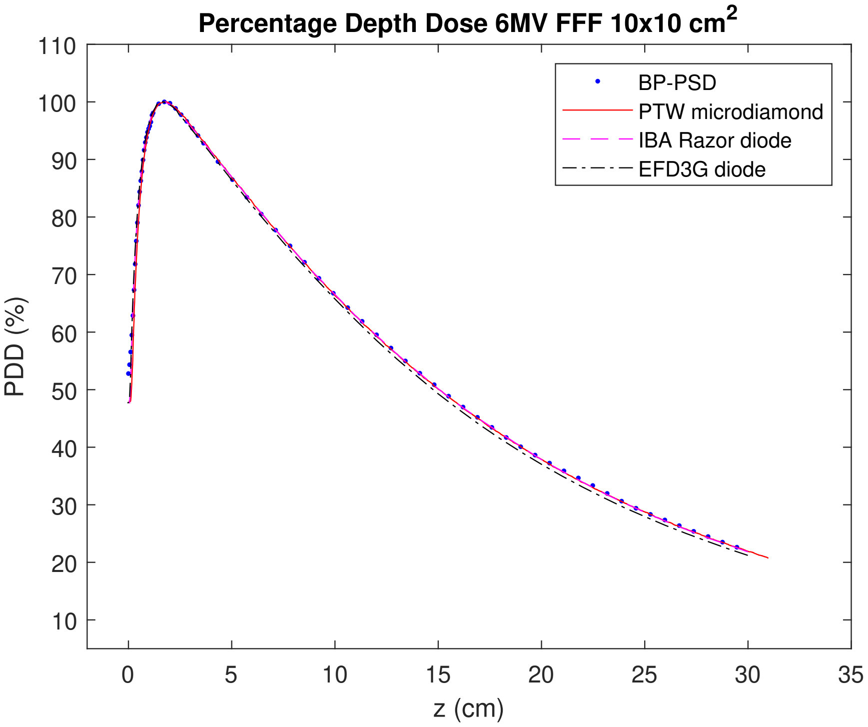

Figure 3.22: PDD comparison of the four detectors for a 10×10 cm^2 square field, with 6 MV FFF energy.

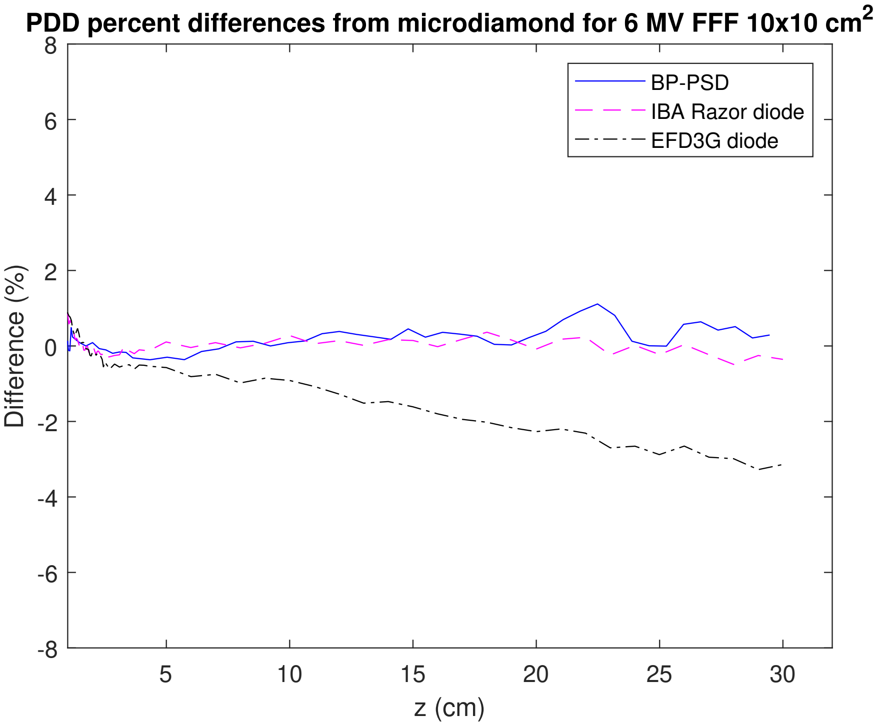

Figure 3.23: Percent differences between each detector PDD output and the microdiamond detector for a 10×10 cm^2 square field, with 6 MV FFF energy.

The percent differences graph are plotted starting from 1 cm. This is done to include a narrow zone around the maximum of the PDD curve and focus the attention on the zones beyond the rise region. In fact, staying in the region near the maximum value of the PDD or going a bit deeper along z with respect to it, the percent differences remain in the ±2.5% range for each detector. However, moving away from the d_{max} abscissa value implies a divergence that grows up to $\sim \pm 6\%$ in the tail region, or even $\sim \pm 20\%$ in the rise region, for some of the detectors. This latter divergence is present in every analyzed situation, but in the majority of the cases it is more pronounced for the BP-PSD rather than for the diodes. The reason for this to happen is the fact that the rise region is the one characterized by the steepest slope in the whole distribution. Because of that, even a slight misalignment along the abscissa axis can lead to huge discrepancies in the ordinate axis. For instance, we can consider that in the rise region the slope of the PDD graphs takes values of ~20 %/mm. By this value, an x displacement of just 0.5 mm would lead to a y gap of ~10%, which is around 10-20% of percent difference between the height of two corresponding points in this region. This is in accordance with the results we obtained in the % graphs. Moreover, an alignment error of 0.5 mm or more is perfectly predictable and consistent with the uncertainties analysis conducted in Section 3.6. These uncertainties are thus inescapable, and for this reason the rise region is not of much interest for the detectors comparison.

Regarding the zone around the maximum, the results are in good agreement with the literature data [3] [11] [12] [21] and with the intrinsic structural differences among the detectors, for which they will inevitably respond in a slightly different way with respect to the others.

From the difference plots we can notice other trends which are worth discussing.

1. Considering the Razor diode, we can notice that its percent variations always stay within 2%, or even 1% for some particular cases and zones, and thus present a better compatibility with the microdiamond than the other two detectors. This is not a surprise for the 1×1 and 3×3 cm^2 fields, since we know that the IBA Razor detector is best suited for small fields [3] [6] [7] [8] [21]. Actually, even if we considered the rise region for the standard fields, the Razor diode is the one that best matches the microdiamond detector. This is justified by the construction characteristics of the diode, such as its active volume [10] [26], which is much smaller than that of the BP-PSD [11] and the EFD3G diode [10], but comparable to that of the microdiamond [9] [25]. Therefore, the Razor diode allows a more accurate reconstruction of this parts of the analyzed curves, similar to that obtained with the microdiamond detector.

2. Considering the EFD3G diode, it shows a tendency to diverge towards negative percent differences. For WFF beams this bias leads to % variations that grow up to 3-4% in the deeper zone of the tail region, but in the FFF case it gets more pronounced, reaching deviations of 6-7%. This may be caused by a different response of the detector when exposed to higher dose rates. In fact, as seen in Table 2.1, EFD3G diode is the one presenting the higher dose per pulse dependence.

3. Considering BP-PSD, it mainly presents oscillating deviations in the ±2%

range, which get larger in some isolated cases (such as the 1×1 cm^2 field in Figure 3.13, since for this specific field size the measurement may be affected by MLC reproducibility issues). That happens more frequently for deeper regions, but this tendency at higher z is shared among all the detectors. An ulterior aspect that can be noticed is that, regarding FFF beams, BP-PSD percent differences start deviating towards the upper side of the plots. This may be caused by an enhanced response of the scintillator at higher dose per pulse.

The construction characteristics details and how they affect the measurements will be discussed in Chapter *Discussion and Conclusions*.

Another yardstick for PDDs comparison is the d_{max} parameter. The following tables report the d_{max} values evaluated for each energy, each detector and each acquired field size during PDD measurements.

d_{max} values (mm) for 6 MV WFF energy							
	Field size (cm×cm)						
Detector	**0.6×0.6**	**1×1**	**2×2**	**3×3**	**5×5**	**10×10**	**30×30**
BP PSD	11.6	13.7	15.9	15.9	16.4	14.3	14.0
PTW microdiamond	11.2	12.9	15.1	16.1	16.0	14.7	14.5
Razor diode	11.5	14.5	15.5	15.5	-	15.0	-
EFD3G diode	12.0	13.0	15.0	15.6	16.0	16.0	-

Table 3.1: d_{max} values for the WFF PDDs. "-" fills the tiles of the cases for which the PDD was not acquired or is missing.

d_{max} values (mm) for 6 MV FFF energy							
	Field size (cm×cm)						
Detector	**0.6×0.6**	**1×1**	**2×2**	**3×3**	**5×5**	**10×10**	**30×30**
BP PSD	12.0	13.2	16.7	18.1	17.5	17.4	-
PTW microdiamond	12.2	14.1	16.5	18.2	17.4	17.3	16.5
Razor diode	11.0	14.0	16.0	17.5	-	18.0	-
EFD3G diode	11.0	12.5	15.5	17.0	16.5	17.0	-

Table 3.2: d_{max} values for the FFF PDDs. "-" fills the tiles of the cases for which the PDD was not acquired or is missing.

For the microdiamond, the Razord diode and the EFD3G diode, d_{max} is calculated by the *My QA-accept* software. On the other hand, in the case of BP-PSD, since it is not integrated with the system and there are too few points around the maximum to properly identify the d_{max} abscissa, a second degree polynomial fit is performed near the maximum of the curve, then the abscissa of the maximum is taken as the best candidate for d_{max}.
The d_{max} values for WFF and FFF beams at 6 MV energies, SSD = 90 cm and 10×10 cm^2 field are respectively 15 mm and 17 mm. From Tables 3.1 and 3.2 it is possible to notice that at some field sizes, in particular the smaller ones, the computed d_{max} value tends to be smaller than the expected value. This happens because for smaller fields partial source occlusion takes place, the fluence of the

beam gets affected and as a result the PDD distribution slightly changes its shape with respect to the standard fields cases. Indeed, this shift in the d_{max} value can be observed for 0.6×0.6 and 1×1 cm^2 square fields, whereas it begins to be negligible from 2×2 field onward. Anyway, this bias seems to be present for all the detectors at those two field sizes, with some isolated deviations, so it is safe to assume that it is not a systematic error affecting only a single detector. Overall, for each field size above the 1×1 cm^2, all the d_{max} values evaluated with the different detectors are compatible within a ±0.5 mm range of maximum semi-dispersion, with few exceptions.

Larger deviations were found for example for BP-PSD and EFD3G diode at 1×1 cm^2 field FFF. Those deviations and the variability that is noticed for the BP-PSD results may again be a consequence of a misalignment of the distributions, arising in particular by the BP-PSD post processing.

3.4.2 Off Axis Ratios results

The comparison for OAR distributions follows a similar route to the one adopted for the PDDs. Here some examples of crossline and inline profiles comparison among the four detectors are presented, followed by the respective percent differences graphs.

Coherently with the PDD case, the 1×1, 3×3 and 10×10 cm^2 field sizes are taken as the representatives, in order to analyze each field category (small, standard and transient between the two). The 10×10 cm^2 field results will be presented just for BP-PSD and the microdiamond detector, since for the others those OAR were not acquired.

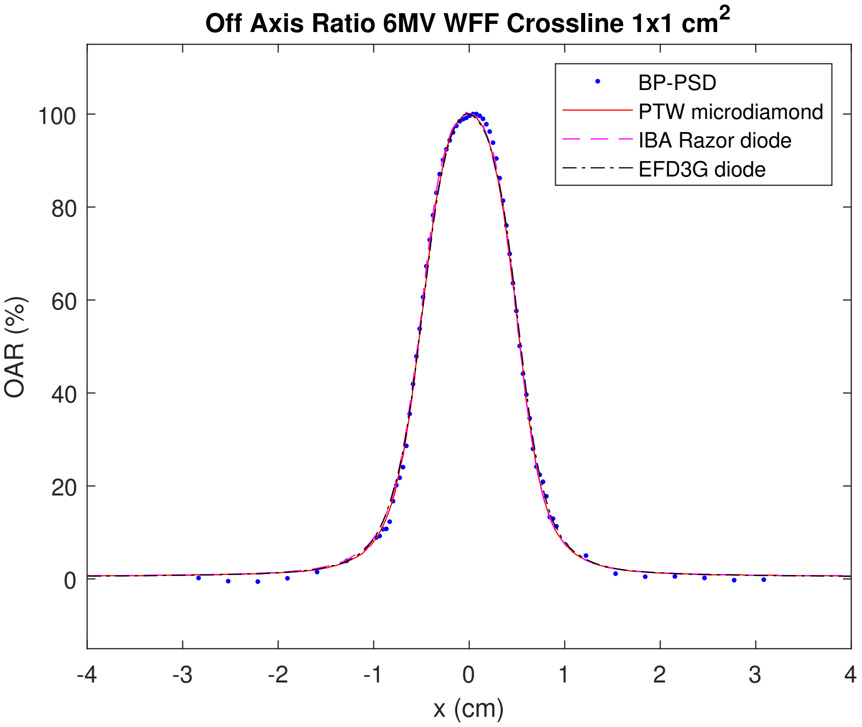

Figure 3.24: Crossline OAR comparison of the four detectors for a 1×1 cm^2 square field at a depth of 10 cm, with 6 MV WFF energy.

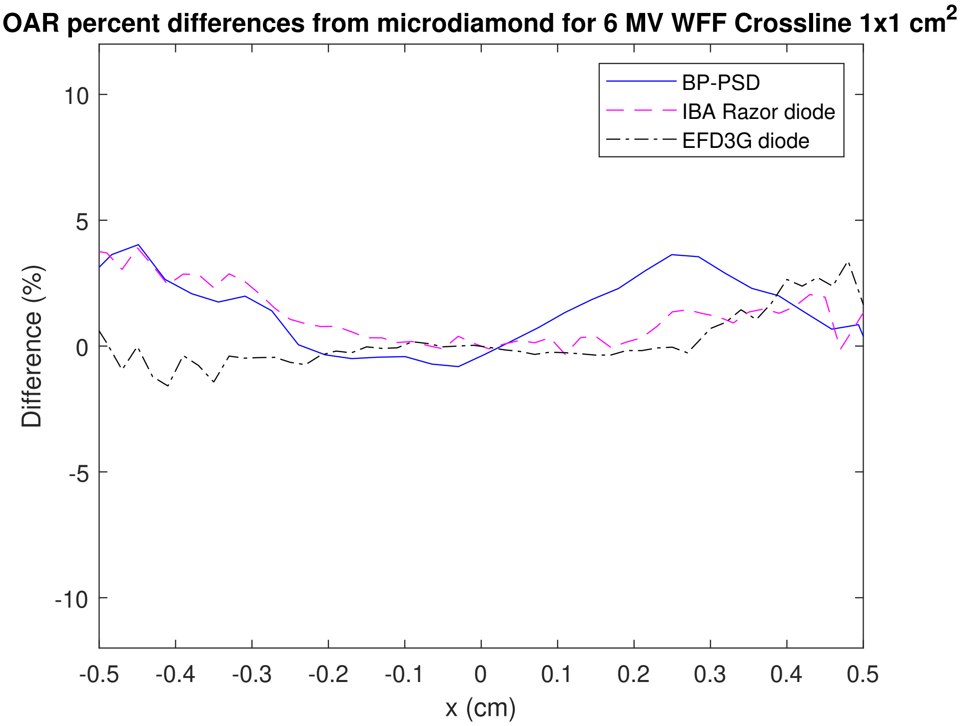

Figure 3.25: Percent differences between each detector crossline OAR output and the microdiamond detector for a 1×1 cm^2 square field at a depth of 10 cm, with 6 MV WFF energy.

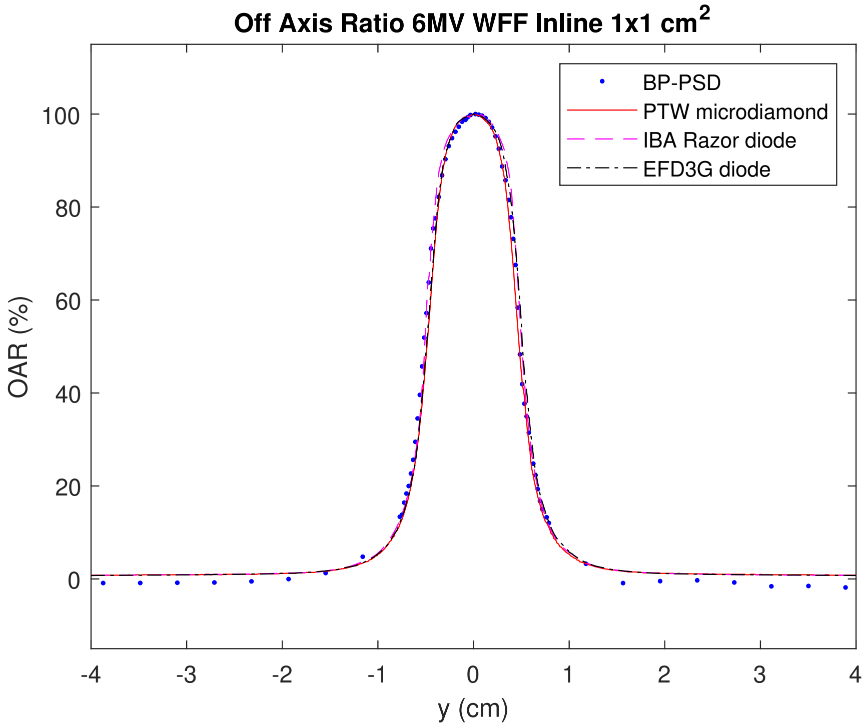

Figure 3.26: Inline OAR comparison of the four detectors for a 1×1 cm^2 square field at a depth of 10 cm, with 6 MV WFF energy.

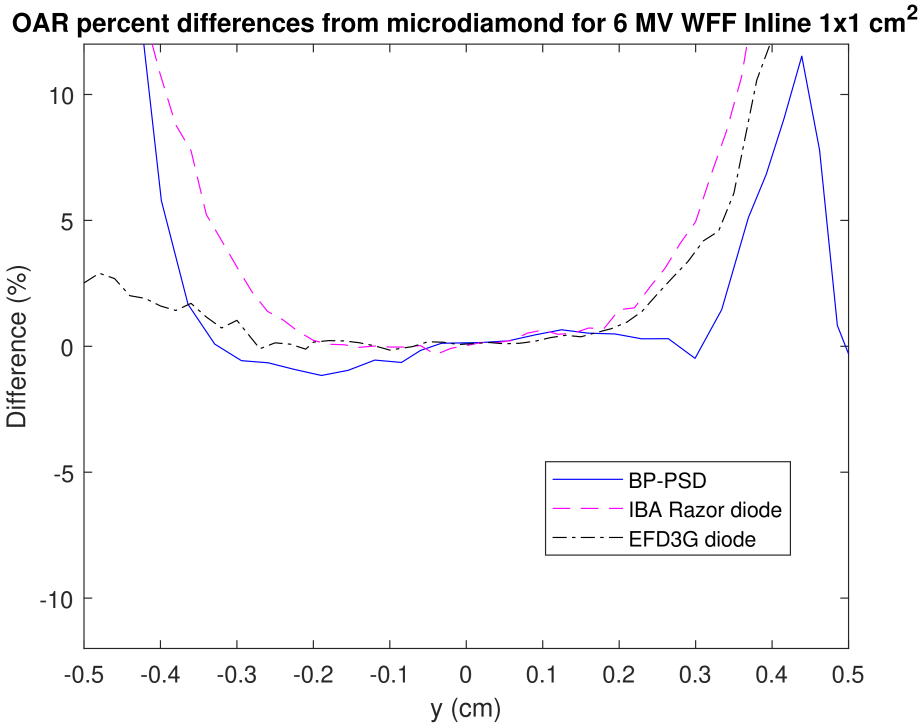

Figure 3.27: Percent differences between each detector inline OAR output and the microdiamond detector for a 1×1 cm^2 square field at a depth of 10 cm, with 6 MV WFF energy.

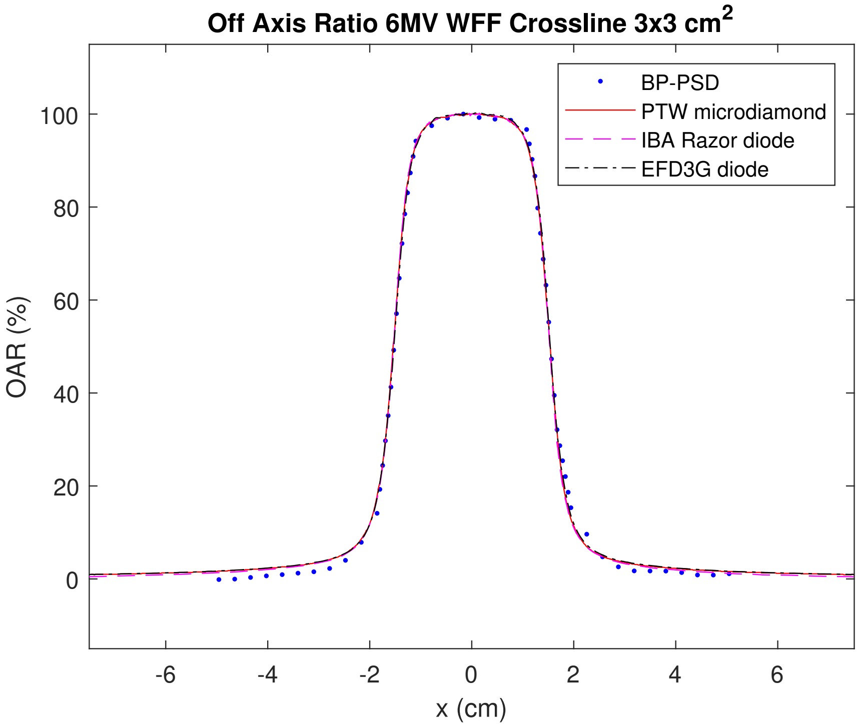

Figure 3.28: Crossline OAR comparison of the four detectors for a 3×3 cm^2 square field at a depth of 10 cm, with 6 MV WFF energy.

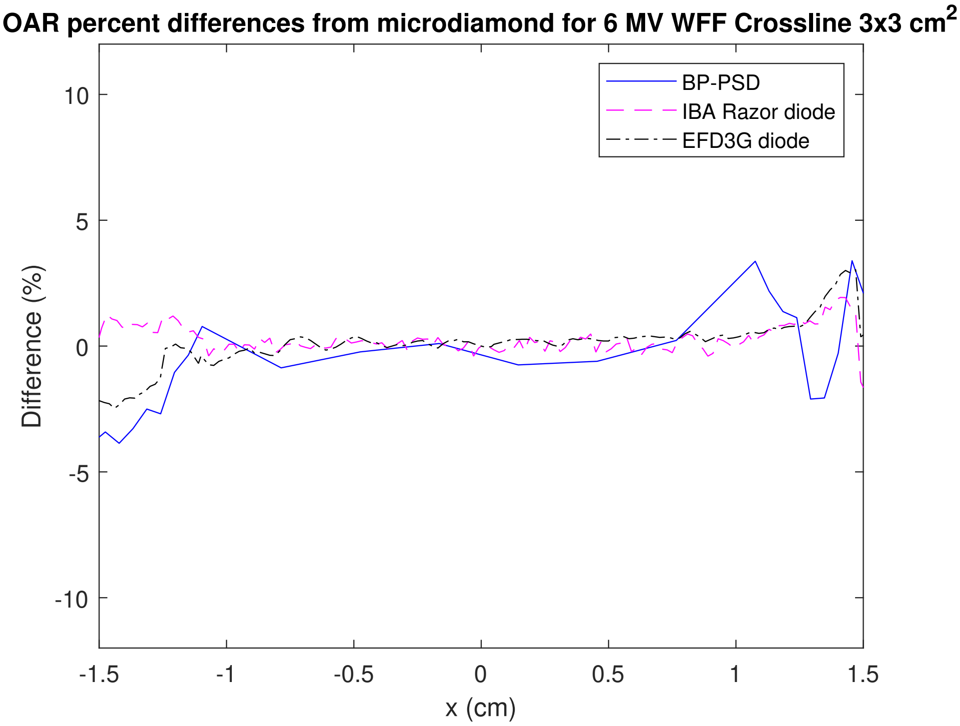

Figure 3.29: Percent differences between each detector crossline OAR output and the microdiamond detector for a 3×3 cm^2 square field at a depth of 10 cm, with 6 MV WFF energy.

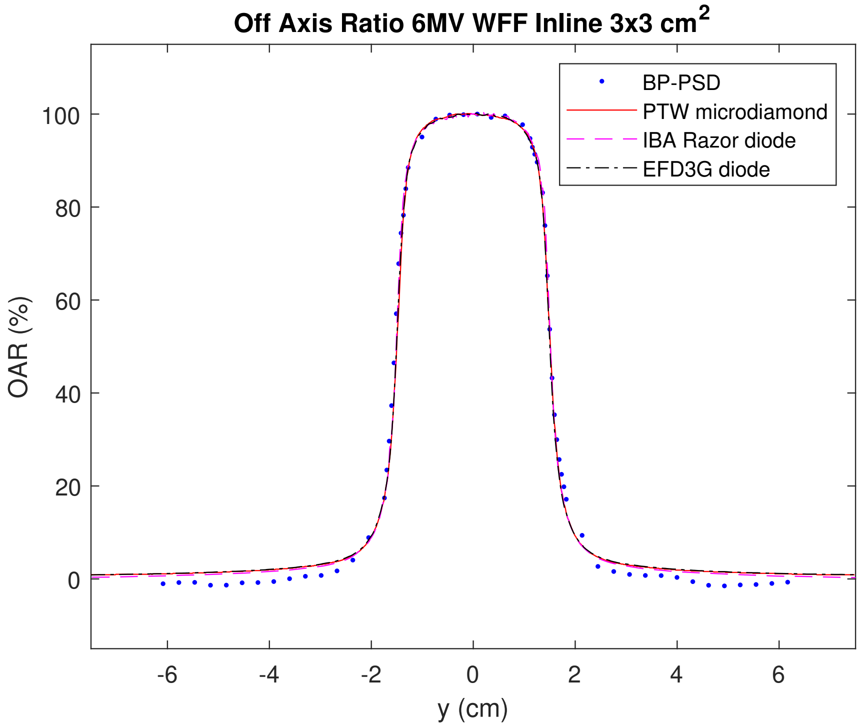

Figure 3.30: Inline OAR comparison of the four detectors for a 3×3 cm^2 square field at a depth of 10 cm, with 6 MV WFF energy.

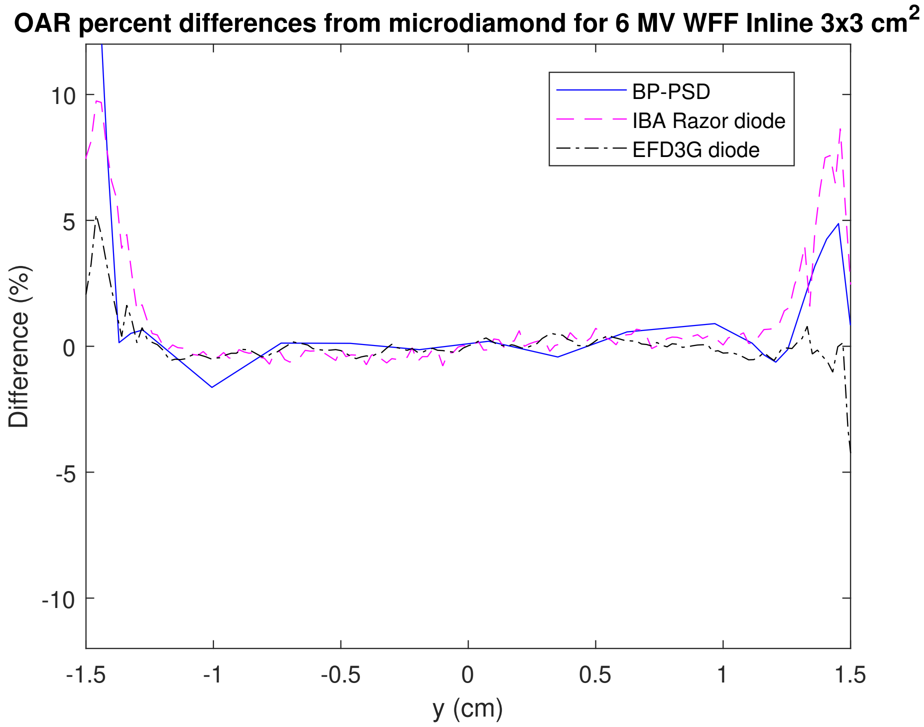

Figure 3.31: Percent differences between each detector inline OAR output and the microdiamond detector for a 3×3 cm^2 square field at a depth of 10 cm, with 6 MV WFF energy.

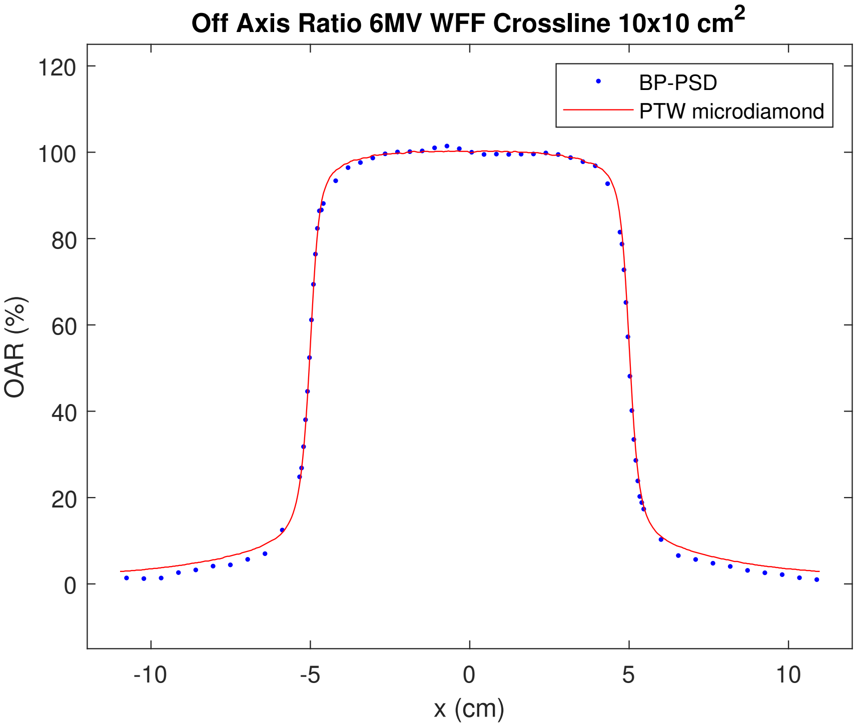

Figure 3.32: Crossline OAR comparison of the four detectors for a 10×10 cm^2 square field at a depth of 10 cm, with 6 MV WFF energy.

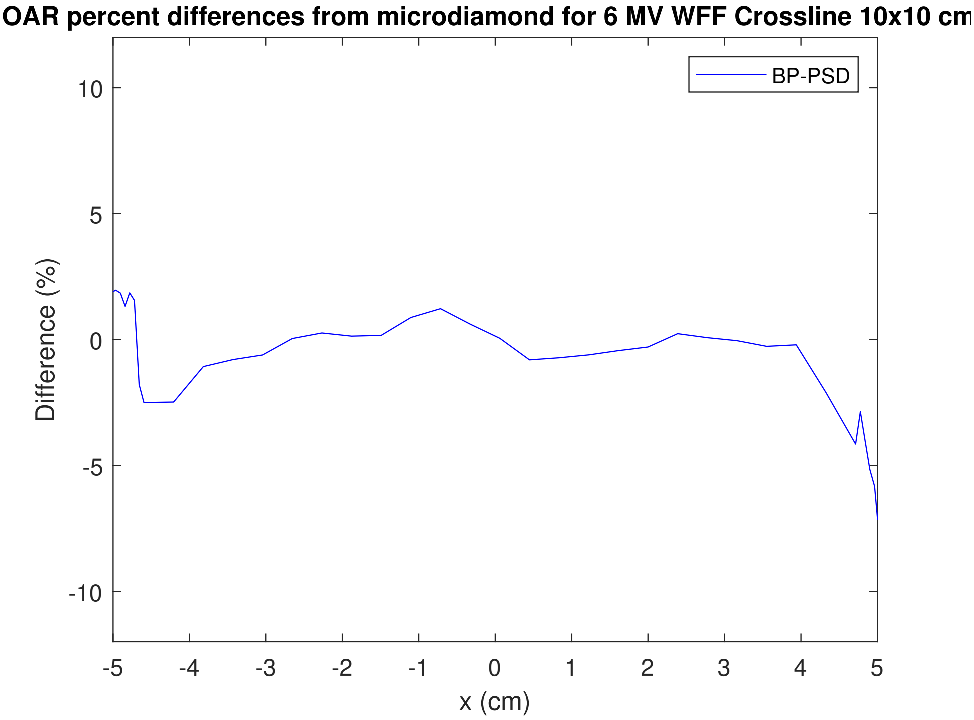

Figure 3.33: Percent differences between each detector crossline OAR output and the microdiamond detector for a 10×10 cm^2 square field at a depth of 10 cm, with 6 MV WFF energy.

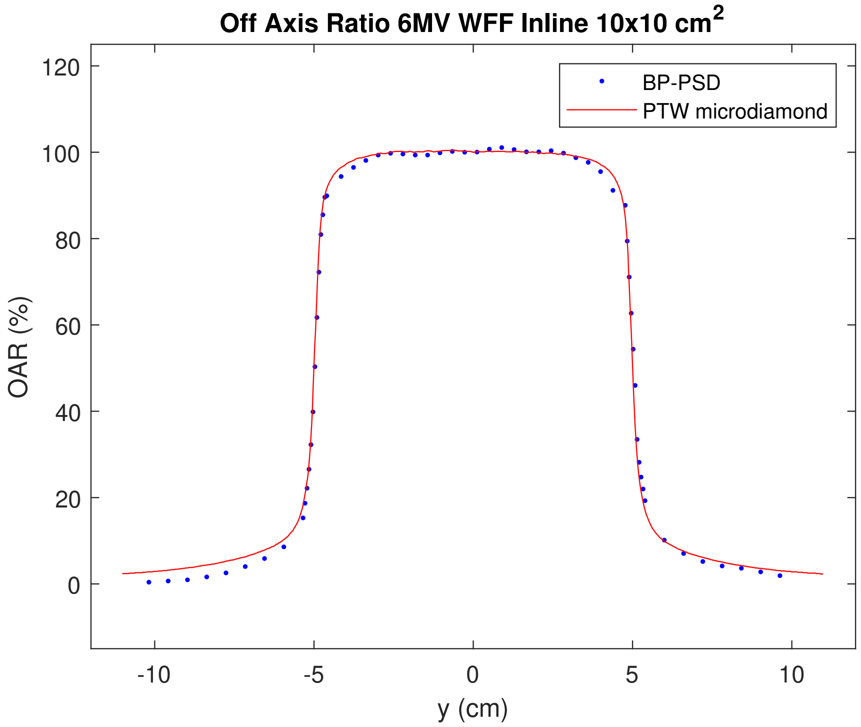

Figure 3.34: Inline OAR comparison of the four detectors for a 10×10 cm^2 square field at a depth of 10 cm, with 6 MV WFF energy.

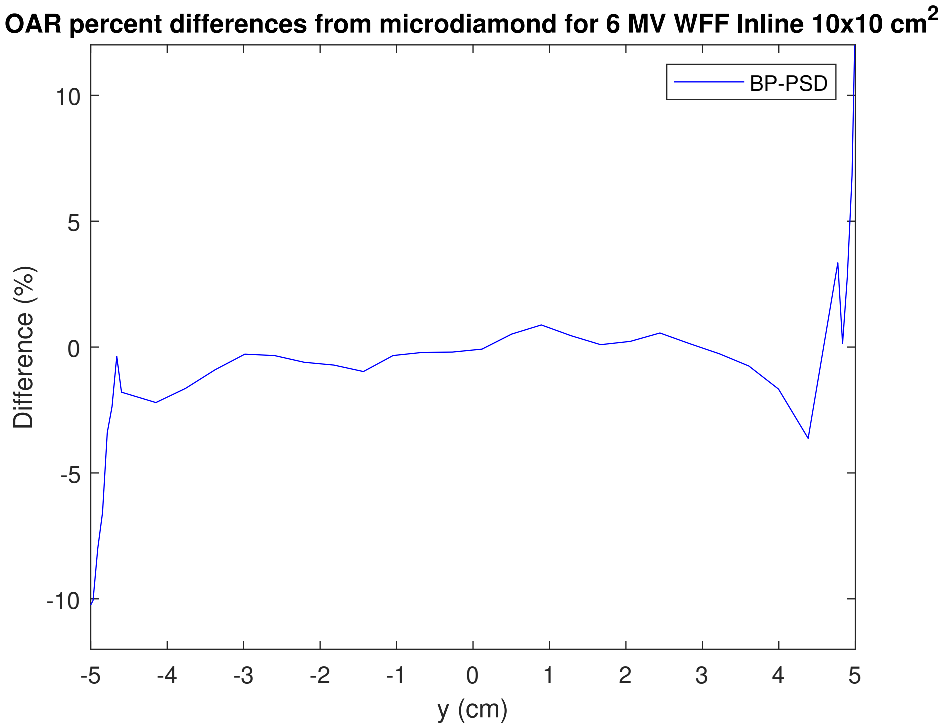

Figure 3.35: Percent differences between each detector inline OAR output and the microdiamond detector for a 10×10 cm^2 square field at a depth of 10 cm, with 6 MV WFF energy.

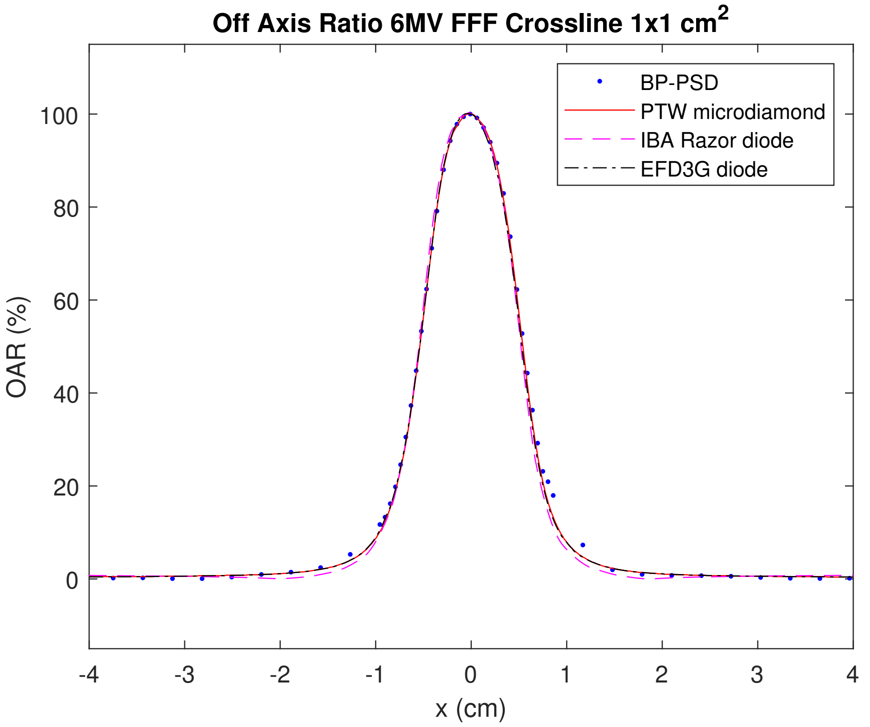

Figure 3.36: Crossline OAR comparison of the four detectors for a 1×1 cm^2 square field at a depth of 10 cm, with 6 MV FFF energy.

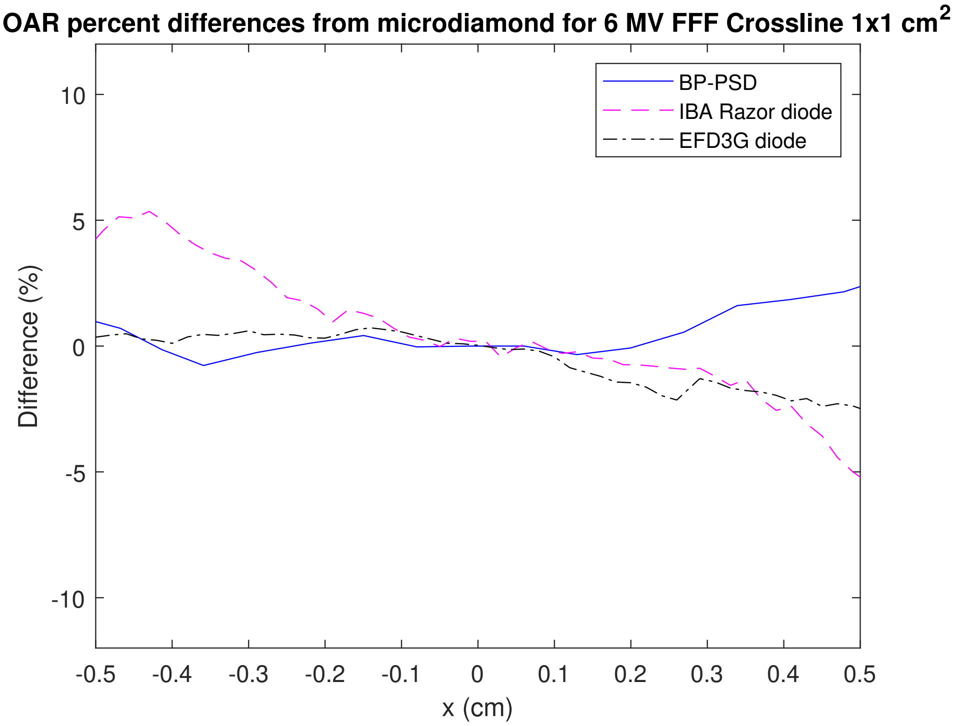

Figure 3.37: Percent differences between each detector crossline OAR output and the microdiamond detector for a 1×1 cm^2 square field at a depth of 10 cm, with 6 MV FFF energy.

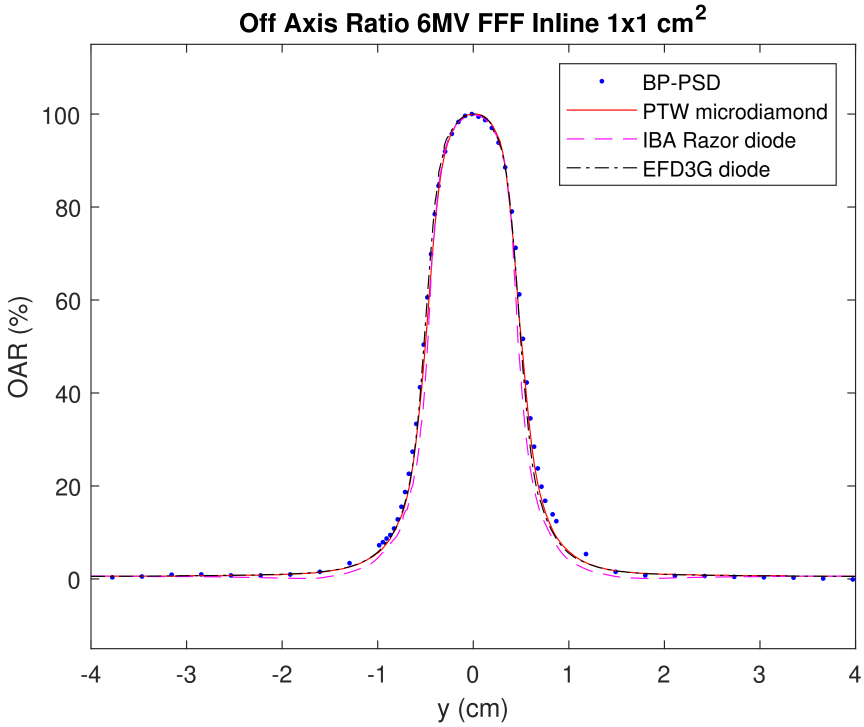

Figure 3.38: Inline OAR comparison of the four detectors for a 1×1 cm^2 square field at a depth of 10 cm, with 6 MV FFF energy.

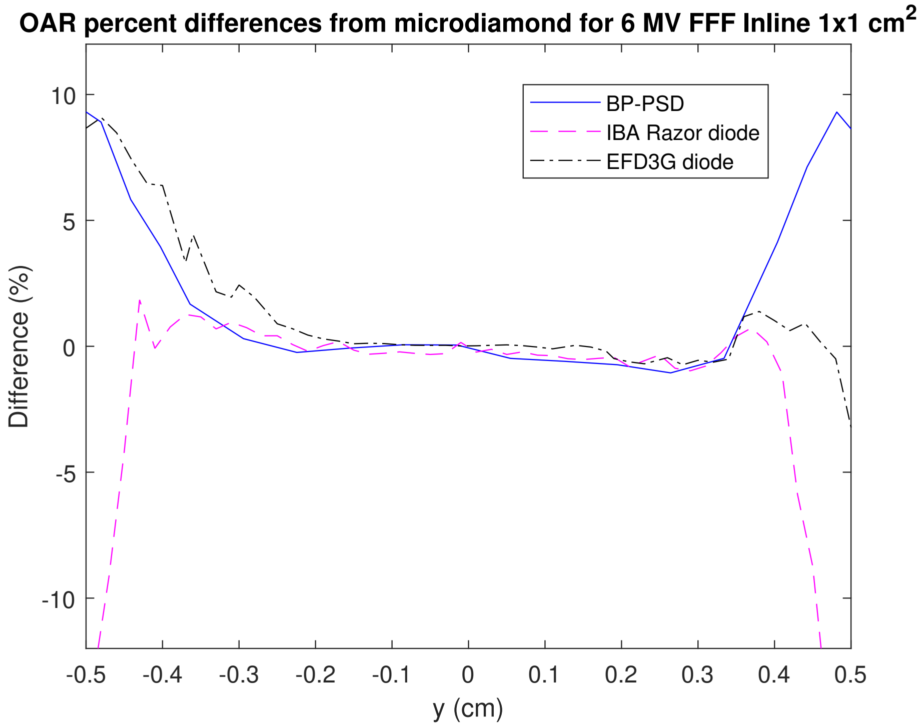

Figure 3.39: Percent differences between each detector inline OAR output and the microdiamond detector for a 1×1 cm^2 square field at a depth of 10 cm, with 6 MV FFF energy.

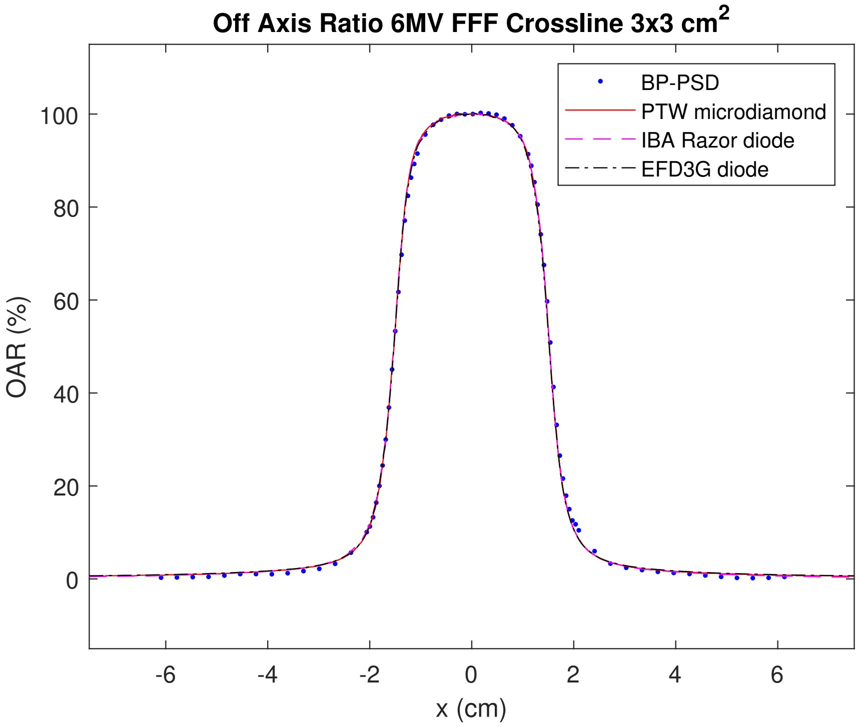

Figure 3.40: Crossline OAR comparison of the four detectors for a 3×3 cm^2 square field at a depth of 10 cm, with 6 MV FFF energy.

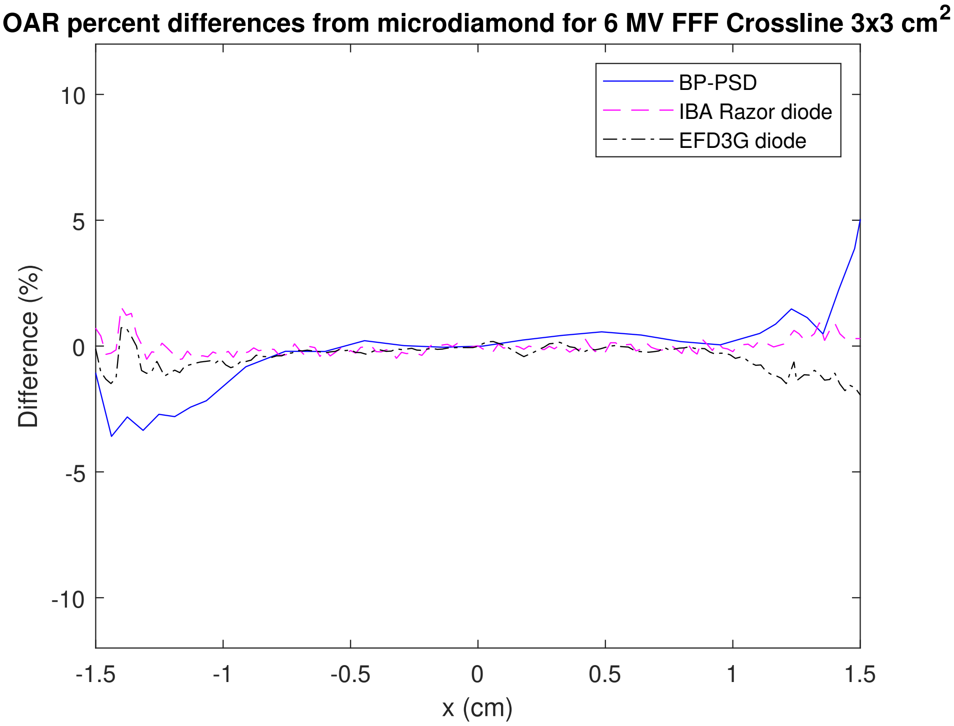

Figure 3.41: Percent differences between each detector crossline OAR output and the microdiamond detector for a 3×3 cm^2 square field at a depth of 10 cm, with 6 MV FFF energy.

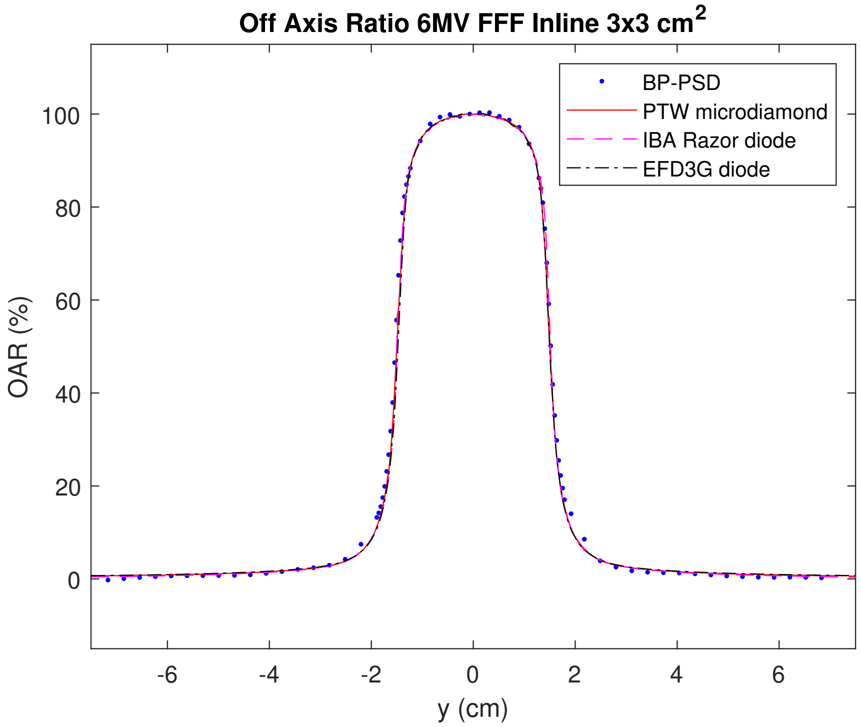

Figure 3.42: Inline OAR comparison of the four detectors for a 3×3 cm^2 square field at a depth of 10 cm, with 6 MV FFF energy.

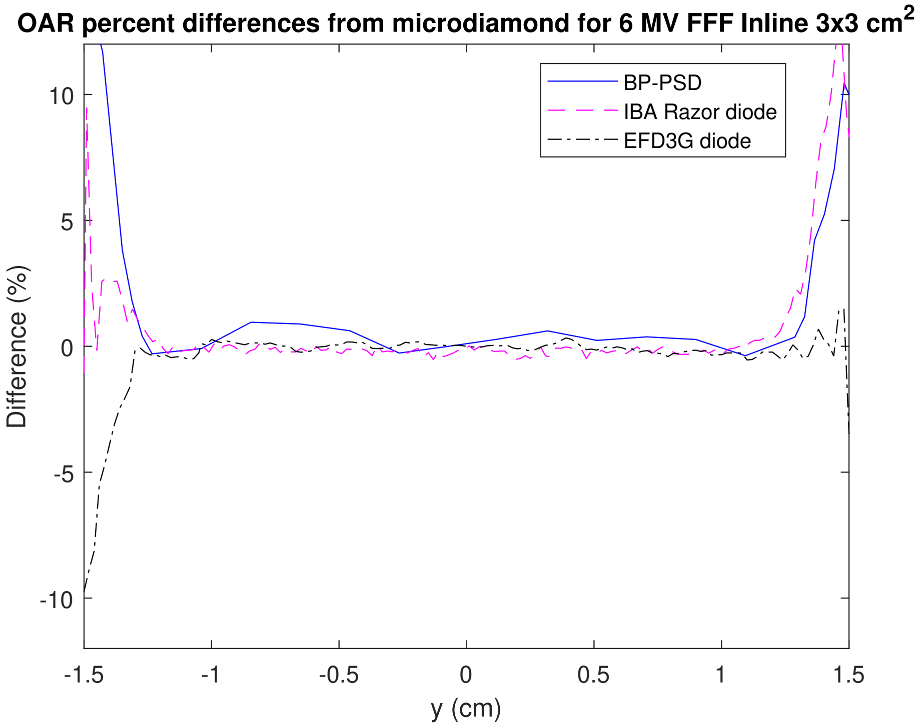

Figure 3.43: Percent differences between each detector inline OAR output and the microdiamond detector for a 3×3 cm^2 square field at a depth of 10 cm, with 6 MV FFF energy.

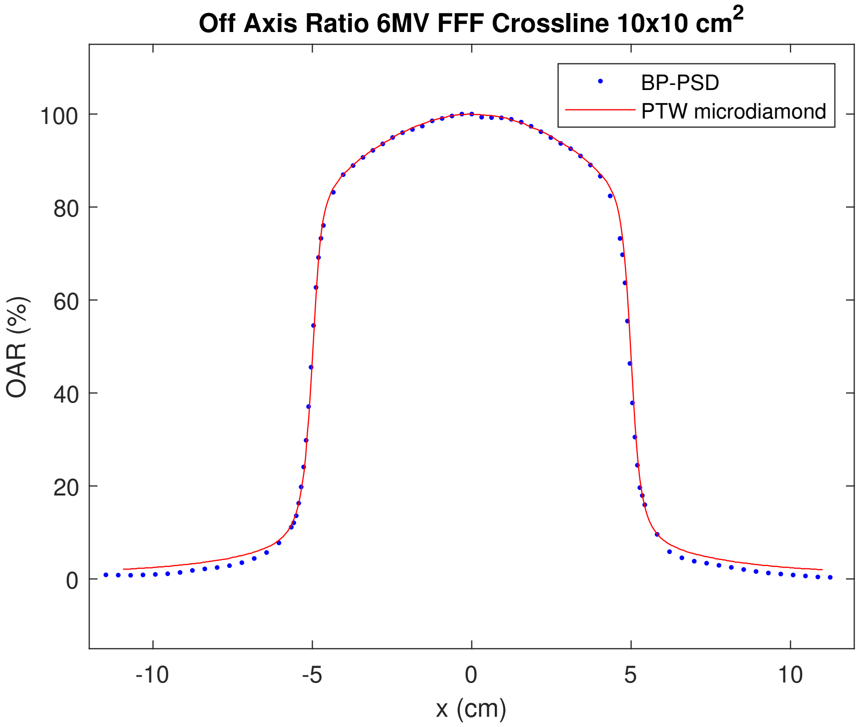

Figure 3.44: Crossline OAR comparison of the four detectors for a 10×10 cm^2 square field at a depth of 10 cm, with 6 MV FFF energy.

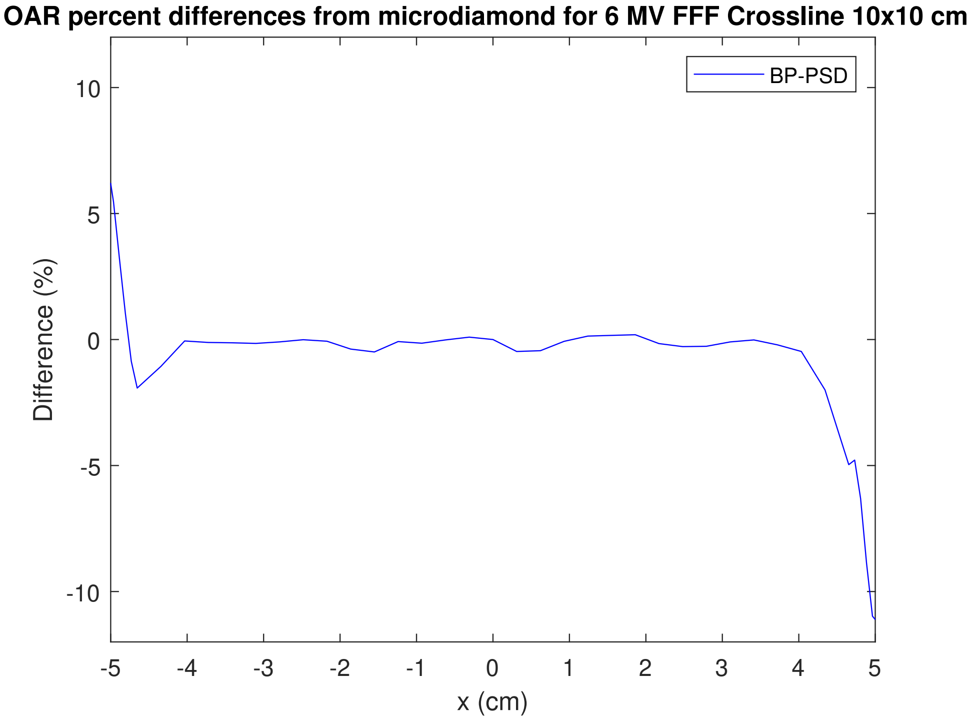

Figure 3.45: Percent differences between each detector crossline OAR output and the microdiamond detector for a 10×10 cm^2 square field at a depth of 10 cm, with 6 MV FFF energy.

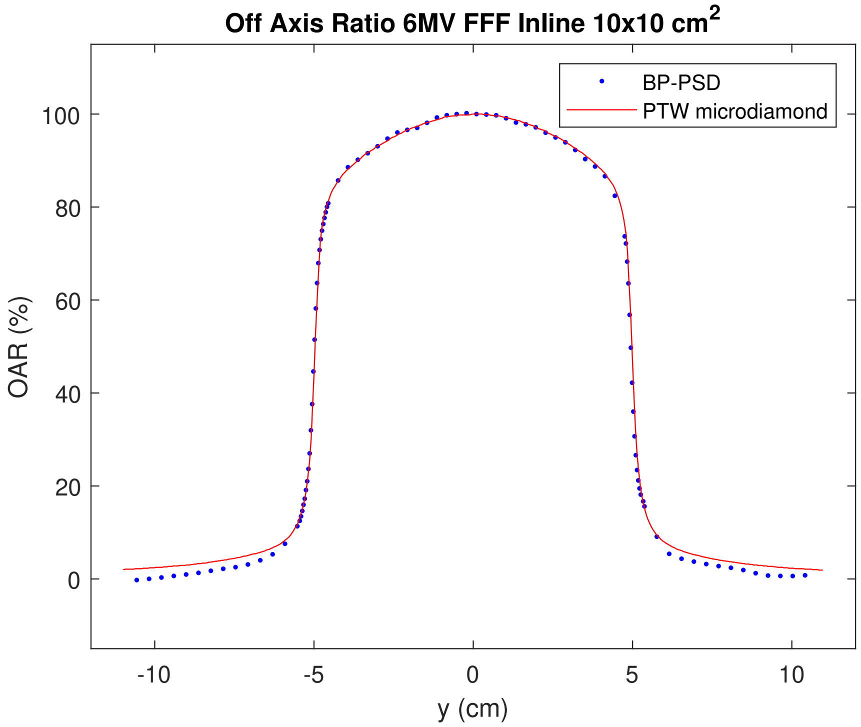

Figure 3.46: Inline OAR comparison of the four detectors for a 10×10 cm^2 square field at a depth of 10 cm, with 6 MV FFF energy.

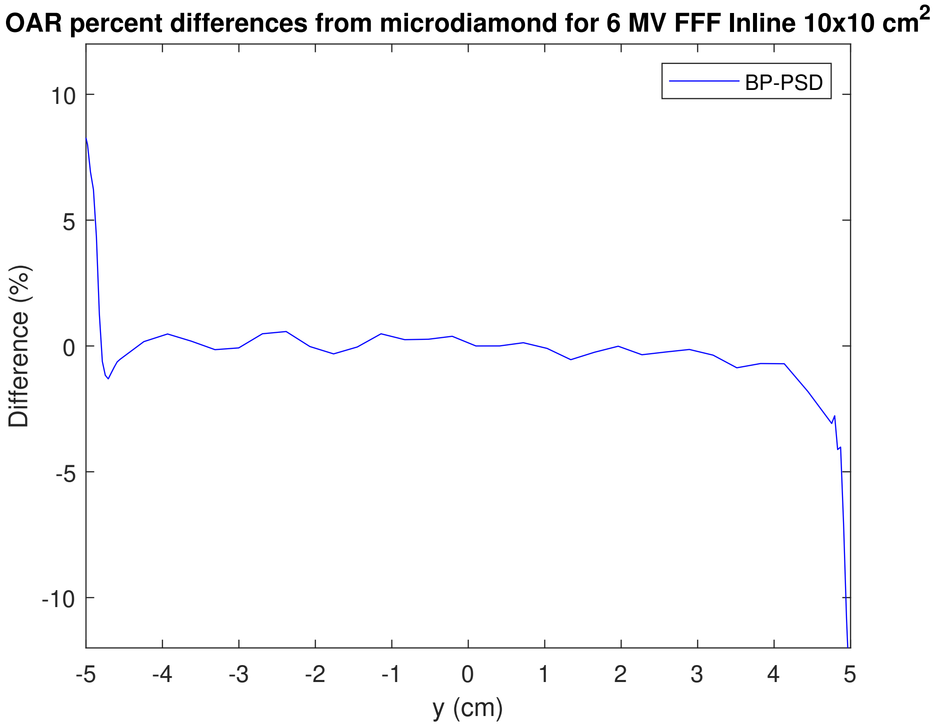

Figure 3.47: Percent differences between each detector inline OAR output and the microdiamond detector for a 10×10 cm^2 square field at a depth of 10 cm, with 6 MV FFF energy.

As happened in the PDD case, the percent differences plots have been restricted to a smaller interval with respect to the full x/y-span of the corresponding profile, in particular they have been confined in a symmetric interval having a width equal to the nominal square field size. This choice has been made since the rise regions are once again affected by extremely high deviations for every single detector. Moreover, the tail zones near the baseline of the OARs are characterized by very large % differences, too (of the order of 40-70%). This happens because in those zones the values to be compared are really low, thus even a small height variation translates in a large % difference. That does not provide us any useful information and therefore the baseline intervals are discarded to allow us to focus on the central part of the profiles. Actually, it is undeniable that the baseline zones present some non-negligible deviations, in particular in the case of the BP-PSD, but for this specific case they may be caused by a bad background subtraction. In fact, it was found that OAR tails collected using the Blue Physics scintillator happen to be systematically lower than the other detectors ones, specifically for the larger field sizes. A probable explanation is that the background subtraction procedure described in Section 3.2 leads to inaccurate results for points that are close to the baseline level when the Cerenkov signal has a considerable magnitude, as happens for standard fields, occasionally causing "disruptions" in the OARs graph reconstruction. For instance, those issues about background subtraction are the reason why the BP-PSD OAR data for the WFF inline 30×30 cm^2 field had to be discarded.
Analyzing the main body of the distributions, some considerations can be made.

1. In the plateau, almost every detector for every analyzed situation agrees with the microdiamond results in a range of ±1%, which gets even better in some portions of the graphs ($\leq \pm 0.5\%$). This is in part due to the opposite condition that was holding for the baseline points, since this time they possess an y coordinate approximately 100 times higher than the previous case. For this reason, their "sensibility" to height variation is considerably lower. However, this is an indicator that the shape of the distribution is not affected in that part of the graphs.

2. The distributions tend to start deviating from the reference one when approaching the "shoulders" zone, just before the effective falling and the penumbrae/tails zones. There, the percent deviations grow to values around 5-10%. For flat plateaus, such as the ones of standard fields, this may be caused by a slope change in the graphs that emphasizes all the misalignment issues, while for smaller fields the slope argument holds even for points near the center of the OAR, thus making them more prone to large deviations apparition.

3. Smaller fields lose the good compatibility of the central body relatively early with respect to standard fields. This can be noticed by observing the graphs about the 1×1 cm^2 field, whose points start deviating from the ±1% range already for distances from the center larger than 3 mm (see Figures 3.27 and 3.39 as an example). 3×3 cm^2 field also shows this tendency, besides being less pronounced. In addition, the deviations at the borders get really large for those field sizes.

Points (2) and (3) are particularly marked for BP-PSD, making it the least compatible detector with the PTW microdiamond in the shoulders, rise and penumbrae/tail regions. Again, the misalignment issues in the BP-PSD post processing concur to this result. This assumption is furthermore reinforced by the fact that, in most of BP-PSD percent differences graphs, deviations from the microdiamond detector in the left and right outer regions take an opposite sign. This is the symptom of a directional shift of the BP-PSD curve with respect to the reference one, which arises a different polarity bias on the two sides. Asymmetries of this kind are also shown by other detectors, nevertheless BP-PSD is the most prone to this type of uncertainties due to its less precise post processing.
As the last consideration, BP-PSD is the detector with the largest active volume among all the others, as can be noticed by Table 2.1, so it is intrinsically less precise in the falls and penumbrae determination due to volume averaging effects.

An important parameter about WFF OAR distributions is their FWHM. We know that in theory it should reflect the nominal field width, apart from the smaller fields which are supposed to have a FWHM that is larger than their nominal field size because of radiation source partial occlusion. The values calculated for all the profiles (both inline and crossline) are written in the tables below.

FWHM values (mm) for crossline OAR WFF							
	Field size (cm×cm)						
Detector	**0.6×0.6**	**1×1**	**2×2**	**3×3**	**5×5**	**10×10**	**30×30**
BP PSD	7.3	10.7	20.4	30.7	50.7	101	301
PTW microdiamond	7.2	10.7	20.6	30.7	50.7	101	302
Razor diode	7.3	10.8	20.6	30.6	-	-	-
EFD3G diode	7.5	10.8	20.5	30.7	-	-	-

Table 3.3: FWHM values (in mm) for the WFF crossline OARs. "-" fills the tiles of the cases for which the OAR was not acquired or is missing.

FWHM values (mm) for inline OAR WFF							
	Field size (cm×cm)						
Detector	**0.6×0.6**	**1×1**	**2×2**	**3×3**	**5×5**	**10×10**	**30×30**
BP PSD	6.5	10.1	20.3	30.6	50.4	100	300
PTW microdiamond	6.2	9.7	19.9	30.1	50.5	100	300
Razor diode	6.1	10.2	20.5	30.3	-	-	-
EFD3G diode	6.0	10.1	20.0	30.1	-	-	-

Table 3.4: FWHM values (in mm) for the WFF inline OARs. "-" fills the tiles of the cases for which the OAR was not acquired or is missing.

All the detectors seem to agree in the FWHM values with a good compatibility (their values have a maximum semi-dispersion of the order of ±0.3% for standard fields, ±4% for smaller fields).This agreement occurs because the width measurement is not affected by the majority of the issues and errors that have been encountered previously. For instance, a misalignment of the distributions during the post processing workflow cannot interfere with the FWHM measurement since all the points get shifted rigidly in the same direction along the abscissa

axis.
A noticeable fact is that the FWHM values, whatever the detector used, are evidently higher in the crossline direction than in the inline direction. This is coherent with our measurement system and our LINAC construction, since the collimators in the two directions are of different types (MLC for the crossline and block collimator for the inline), leading to a slightly different OAR shaping.
From the FWHM it is possible to calculate the S_{clin} value for the various field widths [4]. We remind that they are calculated as the geometrical mean between the crossline and the inline FWHM, so following the formula:

$$S_{clin} = \sqrt{W_{cross} \cdot W_{in}} \tag{3.3}$$

where W_{cross} and W_{in} are indeed the FWHM in the crossline and inline directions. The results are listed in the table below.

S_{clin} **values (mm) for WFF beam**							
	Field size (cm×cm)						
Detector	**0.6×0.6**	**1×1**	**2×2**	**3×3**	**5×5**	**10×10**	**30×30**
BP PSD	6.9	10.4	20.4	30.7	50.6	101	301
PTW microdiamond	6.7	10.2	20.3	30.4	50.6	101	301
Razor diode	6.7	10.5	20.6	30.5	-	-	-
EFD3G diode	6.7	10.4	20.3	30.4	-	-	-

Table 3.5: S_{clin} values for WFF beam. "-" fills the tiles of the cases for which the OARs were not acquired or are missing.

For small fields, we expect the S_{clin} value to result bigger than the nominal field width. This is verified in particular for the smaller field, the 0.6×0.6 cm^2, for which the deviation between the S_{clin} value and the nominal value is of the order of 10%, but is also appreciable for the 1×1 cm^2 field size, having a deviation of ~4% for each detector (apart for the microdiamond whose result is a bit lower). On the other hand, for larger field widths the difference decreases down to a minimum of ~0.3% for the 30×30 cm^2 square field. This is in agreement with our expectations and therefore we can say that this OAR characteristic is respected even by the BP-PSD.

The last comparison is about the penumbrae width. For WFF beams, they are defined as the difference between the abscissa corresponding to an ordinate of 80% of the maximum height and the abscissa corresponding to an ordinate of 20% of the maximum height (those two abscissas are taken on the same side with respect to the central axis of the OAR, arising the distinction between left and right penumbra). This is another parameter that is influenced by small fields features. The left/right penumbrae values are reported in Tables 3.6 and 3.7.

Penumbrae values (mm-mm) for crossline OAR WFF							
	Field size (cm×cm)						
Detector	**0.6×0.6**	**1×1**	**2×2**	**3×3**	**5×5**	**10×10**	**30×30**
BP PSD	3.7-3.8	4.0-4.2	4.9-4.4	5.0-5.8	5.8-5.8	7.5-6.0	8.2-9.2
PTW microdiamond	3.6-3.5	4.1-4.0	4.7-4.6	5.0-4.9	5.5-5.3	6.2-6.1	8.7-8.5
Razor diode	3.7-3.3	4.1-3.9	4.6-4.4	4.8-4.7	-	-	-
EFD3G diode	3.8-3.6	4.3-4.1	4.8-4.7	5.1-4.9	-	-	-

Table 3.6: Left-right penumbrae values for the WFF crossline OARs. "-" fills the tiles of the cases for which the OAR was not acquired or is missing.

Penumbrae values (mm-mm) for inline OAR WFF							
	Field size (cm×cm)						
Detector	**0.6×0.6**	**1×1**	**2×2**	**3×3**	**5×5**	**10×10**	**30×30**
BP PSD	2.5-2.6	3.0-2.9	3.0-3.1	3.7-4.0	4.7-4.9	4.7-5.5	-
PTW microdiamond	2.6-2.6	2.9-2.9	3.3-3.3	3.6-3.5	4.0-4.0	4.8-4.7	6.9-7.1
Razor diode	2.4-2.4	2.6-2.6	3.1-3.0	3.2-3.2	-	-	-
EFD3G diode	2.5-2.5	2.8-2.9	3.2-3.2	3.5-3.5	-	-	-

Table 3.7: Left-right penumbrae values for the WFF inline OARs. "-" fills the tiles of the cases for which the OAR was not acquired or is missing.

Penumbrae are the most detector-dependent parameter, since the characteristics of the detector and its active volume shape and width greatly influence them. Microdiamond detectors and diodes are among the most suitable and precise detectors for penumbrae determination, indeed the values obtained from them do not differ too much (order of few %), although the Razor diode tends to exhibit values systematically lower than the other two detectors ones. Another feature is that among these three detectors there are no major discrepancies for the determination of the larger penumbra (between the left and right penumbrae results). On the other hand, BP-PSD often disagrees for the largest penumbra, and sometimes presents some non-negligible deviations and asymmetries. However, its values are overall coherent with those of the other detectors.

We point out that the FWHM and the penumbra width are defined as shown in this Section only for WFF beams. The esteem for FFF beams would need a dedicated and more complex calculation that falls beyond the scope of this thesis [27].

3.5 Field Output Factors results

3.5.1 Small fields correction factors

In small field dosimetry, one has to take into account all the issues discussed in Section 1.4. In particular, absolute dose measurements and field output factors need to include a factor to account for those divergences [4].
IAEA TRS-483 Code of Practice provides a formalism and a list of correction factors, named $k^{f_{clin},f_{msr}}_{Q_{clin},Q_{msr}}$ [5]. These values depend on the Machine Specific Ref-

erences (msr) and the clinical conditions (clin), and thus vary from detector to detector, from field to field (f) and from beam quality to beam quality (Q).
For conventional radiotherapy machines, the reference field is a 10×10 cm^2 size and the reference condition is to place the detector 100 cm SDD (Source to Detector Distance) or SSD (Source to Surface Distance) and 10 cm underwater (on the central axis of the field).

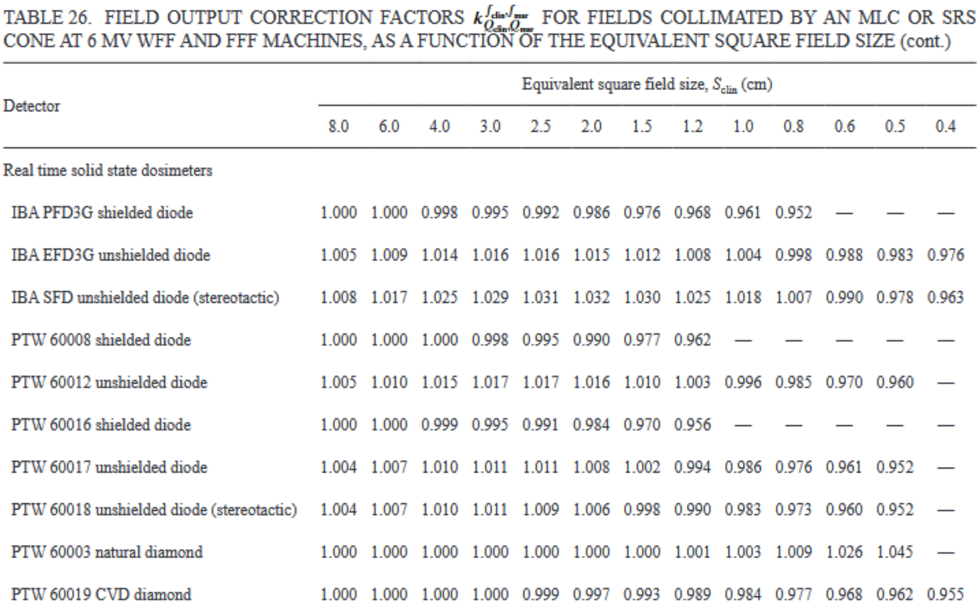

TABLE 26. FIELD OUTPUT CORRECTION FACTORS $k_{Q_{clin},Q_{msr}}^{f_{clin},f_{msr}}$ FOR FIELDS COLLIMATED BY AN MLC OR SRS CONE AT 6 MV WFF AND FFF MACHINES, AS A FUNCTION OF THE EQUIVALENT SQUARE FIELD SIZE (cont.)

Detector	Equivalent square field size, S_{clin} (cm)												
	8.0	6.0	4.0	3.0	2.5	2.0	1.5	1.2	1.0	0.8	0.6	0.5	0.4
Real time solid state dosimeters													
IBA PFD3G shielded diode	1.000	1.000	0.998	0.995	0.992	0.986	0.976	0.968	0.961	0.952	—	—	—
IBA EFD3G unshielded diode	1.005	1.009	1.014	1.016	1.016	1.015	1.012	1.008	1.004	0.998	0.988	0.983	0.976
IBA SFD unshielded diode (stereotactic)	1.008	1.017	1.025	1.029	1.031	1.032	1.030	1.025	1.018	1.007	0.990	0.978	0.963
PTW 60008 shielded diode	1.000	1.000	1.000	0.998	0.995	0.990	0.977	0.962	—	—	—	—	—
PTW 60012 unshielded diode	1.005	1.010	1.015	1.017	1.017	1.016	1.010	1.003	0.996	0.985	0.970	0.960	—
PTW 60016 shielded diode	1.000	1.000	0.999	0.995	0.991	0.984	0.970	0.956	—	—	—	—	—
PTW 60017 unshielded diode	1.004	1.007	1.010	1.011	1.011	1.008	1.002	0.994	0.986	0.976	0.961	0.952	—
PTW 60018 unshielded diode (stereotactic)	1.004	1.007	1.010	1.011	1.009	1.006	0.998	0.990	0.983	0.973	0.960	0.952	—
PTW 60003 natural diamond	1.000	1.000	1.000	1.000	1.000	1.000	1.000	1.001	1.003	1.009	1.026	1.045	—
PTW 60019 CVD diamond	1.000	1.000	1.000	1.000	0.999	0.997	0.993	0.989	0.984	0.977	0.968	0.962	0.955

Figure 3.48: Example of correction factors table from IAEA TRS-483 Code of Practice.

In the table shown in Figure 3.48 it is possible to appreciate that $k_{Q_{clin},Q_{msr}}^{f_{clin},f_{msr}}$ values are given as a function of S_{clin} (called "equivalent square field size"), not the nominal field size.
k values modify the calculations for absolute dosimetry and FOF. The latter appear in dosimetry calculations as:

$$D_{w,Q_{clin}}^{f_{clin}} = D_{w,Q_{msr}}^{f_{msr}} \cdot \Omega_{Q_{clin},Q_{msr}}^{f_{clin},f_{msr}} \tag{3.4}$$

where $D_{w,Q_{clin}}^{f_{clin}}$ is the absorbed dose to water at a reference point in a water phantom for a clinical field f_{clin} of quality Q_{clin} and in the absence of the dosimeter. $D_{w,Q_{msr}}^{f_{msr}}$ is the reference dose in water. $\Omega_{Q_{clin},Q_{msr}}^{f_{clin},f_{msr}}$ is indeed the FOF, which is normally calculated as:

$$\Omega_{Q_{clin},Q_{msr}}^{f_{clin},f_{msr}} = \frac{M_{Q_{clin}}^{f_{clin}}}{M_{Q_{msr}}^{f_{msr}}} \tag{3.5}$$

where M are the readings of the dosimeter.
The correction factor is applied by a simple multiplication:

$$\Omega_{Q_{clin},Q_{msr}}^{f_{clin},f_{msr}} = \frac{M_{Q_{clin}}^{f_{clin}}}{M_{Q_{msr}}^{f_{msr}}} \cdot \left[\frac{D_{w,Q_{clin}}^{f_{clin}} / M_{Q_{clin}}^{f_{clin}}}{D_{w,Q_{msr}}^{f_{msr}} / M_{Q_{msr}}^{f_{msr}}} \right] = \frac{M_{Q_{clin}}^{f_{clin}}}{M_{Q_{msr}}^{f_{msr}}} \cdot k_{Q_{clin},Q_{msr}}^{f_{clin},f_{msr}} \tag{3.6}$$

The term inside the square brackets is usually obtained by Montecarlo simulations and it corresponds to the $k_{Q_{clin},Q_{msr}}^{f_{clin},f_{msr}}$ correction factor provided by the IAEA TRS-483 Code of Practice [5].

During the analysis, correction factors have been taken by the IAEA document for the used detectors (Section 2.2), with the exception of the IBA Razor diode and BP-PSD. The correction factor of the IBA Razor diode is not listed in the IAEA TRS-483 and it was found in the literature [6] [7] [8], while BP-PSD is supposed to have negligible corrections [11] [12].
For each detector apart from BP-PSD, the $k^{f_{clin},f_{msr}}_{Q_{clin},Q_{msr}}$ are calculated with respect to their S_{clin} value written in Table 3.5.
The TRS 483 document and the existing literature provide the correction factors for some specific values of S_{clin}, as seen in the example in Figure 3.48. To obtain $k^{f_{clin},f_{msr}}_{Q_{clin},Q_{msr}}$ for an S_{clin} sitting between two listed values, a third degree polynomial fit has been computed on a certain range of equivalent field sizes, obtaining the correction factor for any S_{clin} needed in that range.
Here a plot of an example fit is provided.

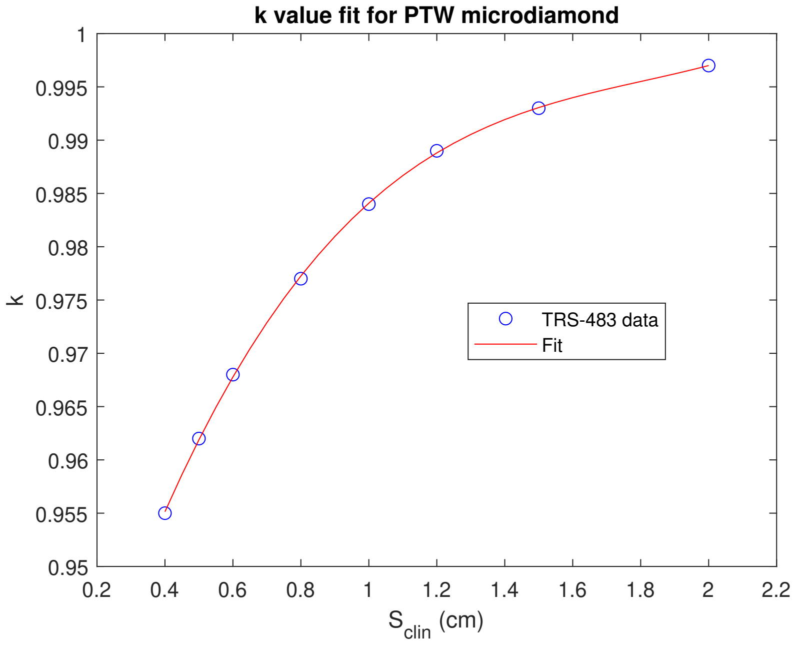

Figure 3.49: k fit plot for PTW microdiamond in the S_{clin} range 0.4-2 cm. The calculated R^2 value is 0.9999.

3.5.2 FOF calculation

For each field and each detector, a series of 4 measurement has been acquired, and then their arithmetic mean has been kept. More sets of reference field $M^{f_{msr}}_{Q_{msr}}$ have been acquired in-between the measurements, and each time the Equation 3.5 ratio has been computed using $M^{f_{clin}}_{Q_{clin}}$ and its time-closest $M^{f_{msr}}_{Q_{msr}}$ acquisition in order to avoid environmental influences as much as possible. Then, the results are corrected by the multiplication with the proper correction factor, found by the procedure described in the previous section.
The corrected FOFs are plotted hereafter, as a function of the nominal field size. The choice not to use $Sclin$ is made because in this way it is easier to compare results from different detectors. Moreover, the S_{clin} values are deeply connected to the LINAC characteristics, specifically to the collimation structure, so to compare

our results with the literature ones it is advisable to maintain the nominal field size dependence.

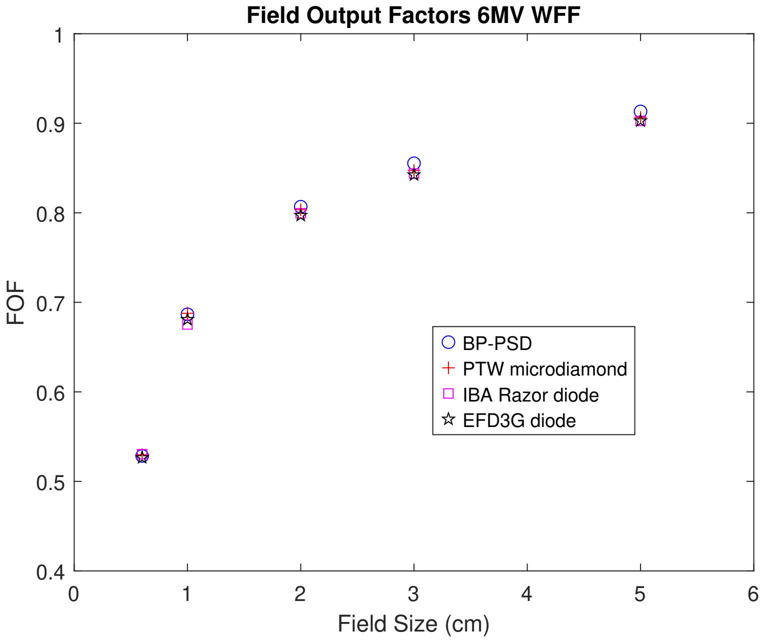

Figure 3.50: 6 MV WFF FOF results for each analyzed detector and field sizes from 0.6×0.6 cm^2 to 5×5 cm^2. The size of the square field in cm is shown in abscissa. The errorbars are not displayed since they would result graphically too small.

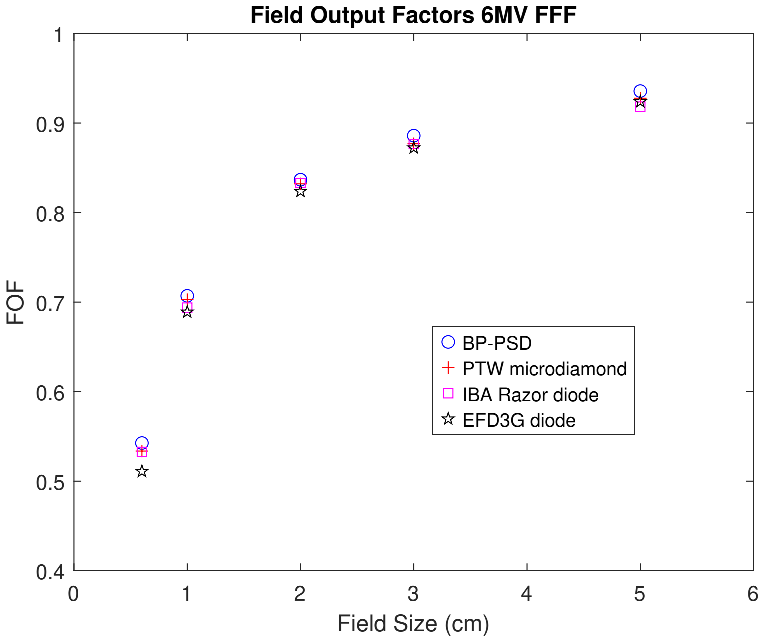

Figure 3.51: 6 MV FFF FOF results for each analyzed detector and field sizes from 0.6×0.6 cm^2 to 5×5 cm^2. The size of the square field in cm is shown in abscissa. The errorbars are not displayed since they would result graphically too small.

As can be appreciated from the figures above, the results are very similar for each considered field and in both energy cases. The worst compatibilities are found in the FFF case, where the values are more widespread, in particular for the 0.6×0.6 cm^2 field (and even in this case the maximum deviation stays within 6%). The BP-PSD FOFs tend to be generically higher than the other ones. In any case, the overall results are lined up with the preexisting literature [11] [12].

3.6 Uncertainties discussion

During data analysis, and in particular during the post processing procedures for BP-PSD raw data, some sources of uncertainties are encountered. By definition, we can distinguish:

- Type A uncertainties, which are the ones connected to the statistic of our system (so for instance coming from the repeated measurements of a specific quantity).
- Type B uncertainties, which refer to other sources of errors, such as systematic errors that may affect the final results.

Regarding this thesis work, the predominant type is certainly the B type. The only instance where A type uncertainties are found is the FOF acquisition, since in that case series of 4 consecutive measures were taken. Furthermore, other measurement sets have been acquired in order to refine those uncertainties (see the final part of Section 3.6.1) [28].

3.6.1 FOF uncertainties

We can esteem the type A errors associated with the FOF calculations by computing the standard deviation of each set of 4 measures. Then, since FOF first computation follows Equation 3.5, we must propagate the errors for the measure of each field with the one of the 10×10 cm^2 field.
Following the notation of Equation 3.5, the numerical results for $M_{Q_{clin}}^{f_{clin}}$ and their standard deviations are shown in the following tables as an example only for the EFD3G case, which is the detector whose results diverge the most from the others.

M results (nC) with associated σ for EFD3G				
	Field size (cm×cm)			
Beam energy	**0.6×0.6**	**10×10**	**1×1**	**10×10**
6 MV WFF	60.5±0.3	114.0±0.1	77.2±0.1	114.0±0.1
6 MV FFF	120.7±0.1	233.9±0.1	160.6±0.3	233.6±0.1

Table 3.8: M results for the EFD3G diode with WFF and FFF beams.

M **results (nC) with associated** σ **for EFD3G** (cont.)				
	Field size (cm×cm)			
Beam energy	**2×2**	**3×3**	**10×10**	**5×5**
6 MV WFF	89.5±0.1	94.4±0.1	113.8±0.1	101.6±0.1
6 MV FFF	189.7±0.1	200.5±0.2	233.6±0.1	213.3±0.1

Table 3.9: Continue of Table 3.8.

Table 3.9 is a continuation of Table 3.8.

We recall that in Table 3.8 and 3.9 multiple 10×10 cm^2 results appear because more reference field acquisitions were carried out. The order of the tables, from left to right, matches the temporal order of the acquisitions. The ratio calculations will be conducted between a field size measure and the closest 10×10 cm^2 measure.

After applying Equation 3.5, we need to propagate the errors on the specific field size measure and on the reference one (which will be called M_{clin} and M_{msr} respectively, to lighten the notation). So, assuming the two measures to be statistically independent, the uncertainty associated with the non-corrected FOF (Ω) given by their ratio is found through the formula:

$$\begin{aligned}\sigma_\Omega &= \sqrt{\left(\frac{\partial\Omega}{\partial M_{clin}}\cdot\sigma_{M_{clin}}\right)^2+\left(\frac{\partial\Omega}{\partial M_{msr}}\cdot\sigma_{M_{msr}}\right)^2}\\ &=\Omega\cdot\sqrt{\left(\frac{\sigma_{M_{clin}}}{M_{clin}}\right)^2+\left(\frac{\sigma_{M_{msr}}}{M_{msr}}\right)^2}\end{aligned} \tag{3.7}$$

We thus get that the relative error on Ω is the quadratic sum of the relative errors on M_{clin} and M_{msr}.

The results for the non-corrected FOF are listed below.

Ω **results with associated** σ **for EFD3G**					
	Field size (cm×cm)				
Beam energy	**0.6×0.6**	**1×1**	**2×2**	**3×3**	**5×5**
6 MV WFF	0.531±0.003	0.678±0.001	0.785±0.001	0.829±0.001	0.893±0.001
6 MV FFF	0.516±0.001	0.687±0.002	0.812±0.001	0.859±0.001	0.913±0.001

Table 3.10: Ω results for the EFD3G diode with WFF and FFF beams. Ω are dimensionless.

To calculate the final FOF uncertainties we need to know the type B errors associated with the correction factors. IAEA TRS-483 provides a directory where all the $k^{f_{clin},f_{msr}}_{Q_{clin},Q_{msr}}$ uncertainties are listed [5]. They are exhibited as percent errors, and in our case of interest they span from ±0.7% for the 0.6×0.6 cm^2 field to ±0.3 for the 5×5 cm^2 field. Since the FOF is found by a simple multiplication, as in the previous propagation the final relative error is the quadratic sum of the $k^{f_{clin},f_{msr}}_{Q_{clin},Q_{msr}}$ and the Ω uncertainties. The final results are listed in the following table.

FOF results with associated σ for EFD3G					
	Field size (cm×cm)				
Beam energy	**0.6×0.6**	**1×1**	**2×2**	**3×3**	**5×5**
6 MV WFF	0.527±0.005	0.681±0.004	0.797±0.003	0.842±0.004	0.903±0.003
6 MV FFF	0.512±0.004	0.690±0.004	0.824±0.003	0.872±0.004	0.924±0.003

Table 3.11: FOF results for the EFD3G diode with WFF and FFF beams. FOF are dimensionless.

We can notice that the uncertainties on those values result very low, of the order of 1% at most, and this is the reason why in Figures 3.50 and 3.51 the error bars are omitted. The other detectors results are similar to these regarding the order of magnitude of the errors. Therefore, we cannot explain the larger differences that we encountered for some field sizes between the detectors couples just by taking into consideration the standard deviation of our samples and the relative errors attached to the k values. It is thus clear that additional sources of uncertainties should be seek in order to refine our calculations, such as: MLC leaves positioning (type A uncertainty), detector positioning and detector alignment angle (type B uncertainties) [28].

- Regarding the MLC leaves positioning reproducibility, a set of repeated measures was performed. In particular, using the microdiamond detector (since this uncertainty is thought to be only machine related), a series of Ω measures have been acquired by repeatedly opening and closing the collimators between the measurements. The chosen field for this procedure is the 0.6×0.6 cm^2, since it is the smallest field analyzed and the MLC reproducibility should affect it the most. The result is interpreted as a maximum error for standard fields.

  We obtained a relative error (calculated by the standard deviation of the collected sample) of 1%.

- For EFD3G, x/y detector positioning is based on the CAX protocol. It consists in the acquisition of four different OAR profiles, in order to correct for the shift that may be present between their centroids, as well as any possible angle.

  We can estimate that the uncertainty associated to each OAR centroid acquisition is of the order of the nominal positioning accuracy of the water phantom (which is 0.1 mm) plus an error due to the "hysteresis" generated by successive command administrations (indeed, the water phantom detector holder tends to bias towards the direction that was imposed by the immediately precedent command, because of motors tolerances). We consider this error to be of the same order of the previous one. Then, we are able to sum all of these errors quadratically (one time for each occurrence in the CAX protocol), and finally, considering the average slope of a PDD at 10 cm depth to be ∼0.5%/mm, we get that the order of magnitude of the relative error committed in the x/y alignment procedure is 0.5% (rounded up to include the angle uncertainty too) (we followed a similar reasoning to the one adopted during the PDDs results discussion, in Section 3.4.1). This is in agreement with other similar studies existing in literature [4].

For the z coordinate, the positioning is performed by a first water surface alignment with the help of a plastic cap with a mark to sign the detector active volume location, and then a rigid shift to the desired depth (which is 10 cm for FOF acquisitions). The total uncertainty will thus be composed by the error committed by the operator (which can be estimated to be of the order of 2 mm) and the water phantom positioning accuracy. In total, also including the hysteresis of the movement, we get a percent error ∼1.1%.
Summing the x/y and the z uncertainties quadratically, we get that the total detector positioning error has a value of approximately 1.2%.

Overall, considering the order of magnitude of those calculated uncertainties and summing them quadratically with the statistical ones obtained in Table 3.11, we get that the total error lays in the range of 2-3%. This is in good agreement with our results, since the maximum deviation obtained in the previous FOF computation (Section 3.5.2) is of the order of 6% (which coincides with two times the maximum estimated error).

3.6.2 PDD and OAR uncertainties

PDDs and OARs uncertainties are more challenging to evaluate, since the procedure to obtain one of those relative dose distributions is much more complex than that for FOFs, expecially for BP-PSD.
Among the analyzed detectors, the post processing applied to BP-PSD measurements is surely the most error-prone, since it relies on various passages that add a lot of uncertainties. This procedure would not be necessary if the detector was integrated with the whole movement/acquisition system, as the other detectors are. In this section we will focus on these passages trying to make an esteem of the magnitude of the errors that may arise from them.

1. **Background subtraction.** As previously said in the case of the WFF inline OAR for the 30×30 cm^2 field, fatal errors may arise from this step if the background is miscalculated. In particular, regarding OARs, the background estimation procedure conducted in this work does not take into account the possibility that the background may vary passing from the left to the right side of the acquisition dataset, with respect to the main OAR profile graph. In fact, all the background subtraction is based on the assumption that the zone from which it is calculated is free from radiation and representative of the whole scanning space, and that the detector is moving at the same speed at which the main acquisition will be conducted. Depending on the shape of the raw data, the background zone was chosen in the proximity of the beginning of the measurement or of its end, when the detector is supposed to be outside the radiation field. However, it is not guaranteed that all the previously listed conditions are met.
   As an example, the raw data plot of the crossline OAR WFF for the 30×30 cm^2 is shown in the following figure.

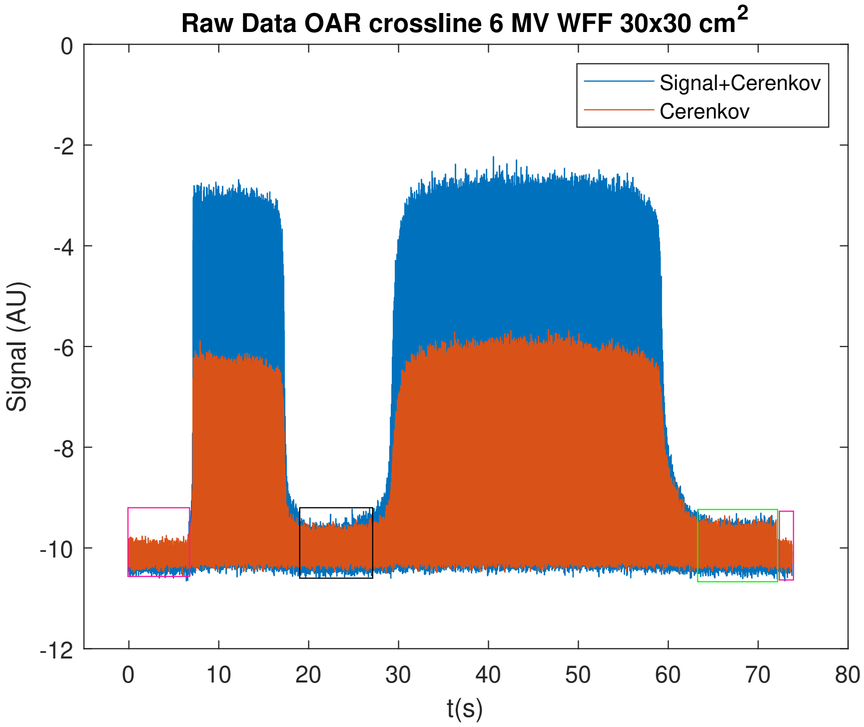

Figure 3.52: Raw data from the BP-PSD detector for a crossline OAR acquisition with 30×30 cm^2 field and 6 MV WFF energy. Notice that the background inside the drawn boxes is different for each color. Black and green are actually near the penumbrae, thus they are on the tails of the OAR and are affected by the radiation of the field, while pinks represent a situation without any radiation (the beam delivery is switched off). Nevertheless, even the black and green boxes slightly differ for the background.

The uncertainty in the case of Figure 3.52 does not lead to the complete disruption of the OAR construction procedure, but severely influences the divergences with respect to the microdiamond OAR, in particular in the tail zones. Furthermore, it is found that the tails divergences tend to become higher for larger field sizes, where Cerenkov spurious signal gets more dominant. Moreover, in general, the detector response to low particle fluxes could also influence its behavior at the tail points.
Referring to the case above, it is found that ACR-corrected background at the right side of the profile is approximately 3 times larger than the left side one. Because of that, the errors of the tail points (which have a value comparable with the background itself) can ideally reach a systematic relative error of the order of 100%.
All of these issues could be solved by performing an empty acquisition, with the radiation turned off. However, this does not count for Cerenkov signal presence (which is found to be relevant for background determination), so it would be advisable to perform background measurements with the radiation turned on. On the other hand, this requires the integration of BP-PSD with the movement and acquisition system, in order to be aware of the system conditions during the background acquisition.

2. **Integration.** This step may lead to minor errors when the integration

window covers a zone with rapid-varying slope. The wider the integration window (to avoid fluctuations due to BP-PSD high time resolution), the more unwanted averaging-effects are collected (for instance, smoothed OAR shoulders or deformed penumbrae).
Considering a time integration width of 50 points, which correspond to ~0.04 s due to BP-PSD time resolution, and the speed of the detector movement as 10 mm/s, the corresponding space interval will be 0.4 mm. This translates in an error due to averaging effects that as first approximation we can consider proportional to the slope variation in that interval multiplied by its width. Supposing a maximum slope rate of change (second derivative) of approximately 2%/mm^2, we thus get an error of the order of 0.3%.

3. **Alignment.** The main phase of alignment occurs when looking for a reference point for the PDD or OAR graph. Without any fixed references, the starting point choice for the curve reconstruction is bound to algorithms such as maximum-likelihood or least-square methods. However, these methods often require an external reference curve, which will make the process not self consistent.
Even with a precise starting point identification, the alignment uncertainty is nourished by the error coming from the detector alignment. Because the CAX protocol is not applicable, BP-PSD alignment is based on the manual process described in Section 2.3.1. By how it works, the operator needs to mark two abscissa values in order to calculate their midpoint, which is an esteem of the shift to be applied to realign the detector with the system isocenter. Each time, the movement system tolerance imposes a position uncertainty of 0.1 mm (nominal value of the water phantom servo control) plus its "hysteresis" error, which we must add to the operator-linked errors when setting the cursors on the BlueSoft software. Considering a lower bound for these errors of the order of 1-1.5 mm and quadratically summing all the errors, we get a minimum x/y displacement error of the order of 2 mm. The z alignment uncertainty is estimated to be of the same order of magnitude, since BP-PSD is not equipped with the plastic cap that helps to align the other detectors. As seen in Section 3.4.1, an abscissa displacement of some mm is more than enough to cause large ordinate percent divergences, specifically in the graph regions characterized by higher slopes. For example, given the 2 mm displacement calculated, a shoulder region characterized by a 5%/mm slope can reach an ordinate displacement of 10%, which corresponds to a similar relative error.

In the end, we found that the background subtraction leads to large uncertainties only in the tail zones, concurring to the large deviations noticeable between the microdiamond and the BP-PSD tails, whereas its contribution gets negligible in the other OAR parts or for the PDDs. Integration width does not play any major role, neither in the OAR plateau (where the averaging effects are close to zero) nor in the zones characterized by higher slope changes (for which the error does not even reach the order of 1%). The alignment seems to be the major contributor to the total uncertainty, with a relative error that can become of the order of 10% for the steepest regions.

Discussion and Conclusions

In this work, we analyzed the characteristics and the properties of the new BP-PSD, comparing it with some other detectors (PTW microdiamond, IBA Razor diode and IBA EFD3G unshielded diode). The results regarding the comparisons of PDDs, OARs and FOFs (conducted in Chapter 3), in addition to the considerations made about the acquisition and post processing procedures, brought to light some positive aspects and some aspects to be improved regarding the BP scintillator.

In particular, the advantages that have been noticed in the use of the BP-PSD are the following:

1. With respect to the other plastic scintillators currently commercially available (whose representatives are the Exradin W1 and W2 plastic scintillators [24]), BP-PSD presents a much simpler method of Cerenkov light subtraction: once it is installed integrally with the whole acquisition apparatus, its ACR calibration exploits very simple formulas and procedures to obtain an efficient Cerenkov subtraction even at higher field dimensions, whereas preexisting scintillators would need a geometrically complex cable setup to obtain the same calibration. Indeed, Cerenkov light calibration for W1 and W2 scintillators is based on the comparison between a configuration in which the fiber cable is completely out of field, and the opposite configuration in which the cable is coiled inside the radiation field, leading to intricate setups [24].

2. Its simple setup and high time resolution allow a quicker and more linear acquisition with respect to traditional dosimeters, which may be useful to perform rapid consecutive measurements spending very little time. This could become particularly useful in a Commissioning circumstance, for which the time required to acquire large sets of measurements is often an issue [1].

3. Its good linear response and stability when exposed to different delivered dose values and dose rates make BP-PSD a versatile choice that can show good performances in a wide range of situations, including small field dosimetry, where its response deviations are limited and controllable.
   Moreover, its hardware frame is configured to guarantee flexibility and adaptability by the exploiting of modular cartridges and the adjustments on the analogical data acquisition components.

4. It possesses an extremely high time resolution, which can make it suitable for modern radiotherapy techniques which are based on high dose delivery

in a short time interval, such as the FLASH radiotherapy (FLASH-RT).

5. Its results regarding the FOFs measurements show that the correction factors needed to adjust its response in a small field circumstance are equal to unity, making it a good reference in this particular frame.

From the discussions in the previous chapter, some improvable aspects have been noticed, too. They refer to the following issues:

1. BP-PSD is not yet integrated with all the commercially available water phantom systems. In our specific case, the fact that it was not possible to rely on the Blue Phantom movement and acquisition system during the measurements with BP-PSD led to problems and uncertainties during the analysis. Moreover, some of the advantages previously described can only be exploited only if the whole system is completely integrated and self-sustaining.

2. The BlueSoft software used for data acquisition of the plastic scintillator is still incomplete and needs some refinements. In fact, to take full advantage of its potentialities (such as its high time resolution) an automatized analysis software would be needed, capable of avoiding all the issues regarding the time-space domain conversion, the background subtraction and all the other drawbacks that have been experienced and discussed in Chapter 3.

Overall, these two difficulties are easily solvable, and just need some development work in order to standardize its hardware acquisition system with the preexisting radiotherapy measurement apparatus. This would also make easier the implementation of an appropriate acquisition and analysis software.
Furthermore, the comparison with existing literature shows a good agreement [11] [12], even considering all the error sources that have been encountered.

In some occasions along the analysis, the comparison with the other detectors carried out with reference to the PDDs, the OARs and the FOFs showed that the response of the BP-PSD has a slightly different behavior. The majority of these divergences are caused by the non-integration of the Blue Physics system, as it was widely discussed before, but in some cases we can attribute them to the structural differences that exist among the detectors.

1. The BP-PSD, the Razor diode and the EFD3G diode tend to have a different response when measuring PDDs and OARs, in particular for FFF beams. Indeed, the PDD plots for 6 MV FFF energy show that BP-PSD tends to over-respond, while EFD3G has the opposite tendency and the Razor diode often sits in the middle. This fact is in agreement with the predictions, since for instance it mirrors the dose per pulse dependence which characterizes each detector (see Table 2.1) [9] [10] [26]. This is even confirmed by the FOF results where BP-PSD and EFD3G divergent responses can be appreciated, specifically for smaller field sizes.

2. OAR analysis, altogether with the penumbrae calculation, showed that the active volume width of each detector plays a relevant role. The microdiamond detector and the Razor diode have the smallest active volume, and

indeed they show good OAR profile shaping, for example in the penumbrae zones [9] [10] [25] [26]. EFD3G is a bit worse in penumbrae determination, alongside the Blue Physics scintillator, which, despite having an almost water equivalent material, has a larger sensitive volume than the other detectors, causing a volume effect perturbation [11]. This effect has an impact on profiles measurements. Nevertheless, their results are overall compatible and aligned with the estimated uncertainties.

3. All the considered detectors manifest almost the same problematic aspects for small fields (2×2 and 3×3 cm^2) and very small fields (0.6×0.6 and 1×1 cm^2) investigations, even though BP-PSD sometimes results as the less compatible detector, again because of its non-integrated system issue. These general problems are reflected, for example, in the FOF determination at small field sizes, where the values obtained among the various detectors are more widespread than in the standard fields case, in particular for FFF beams. However, this may also be caused by the issues that affect the $k_{Q_{clin},Q_{msr}}^{f_{clin},f_{msr}}$ parameters listed in the TRS-483 document [5]. In fact, those values (as declared by IAEA in the same document) are found by mixing results coming from different detectors and/or LINAC measurements, as well as Monte Carlo simulations. Furthermore, there exist no distinction between correction factors regarding WFF or FFF beams. In any case, the correction less condition ($k_{Q_{clin},Q_{msr}}^{f_{clin},f_{msr}} = 1$) makes the Blue Physics scintillator suitable for small field dosimetry measures.

In the end, we can say that the BP-PSD has shown a lot of promising features, making it advisable for a wide extent of different uses.

The main issues encountered are easily solvable, and future research could focus on the development of integrated software/hardware systems that may allow to exploit all of its features (such as the simple Cerenkov signal subtraction and the time resolution), as well as other general ACR calibration methods (since more refined procedures involving rectangular fields are objects of study).

In particular, regarding its time resolution, we mention that it can grant a feasible introduction into modern and advanced radiotherapy techniques, as the FLASH radiotherapy.

Appendix

Here are gathered the plots of all the results obtained for PDDs and OARs, referring to Tables 2.2 and 2.3, subdivided by type and beam energy.

PDD 6 MV WFF

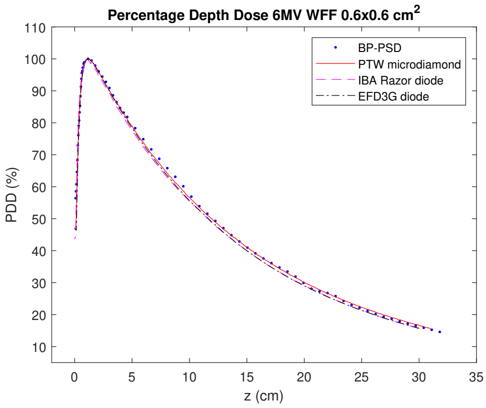

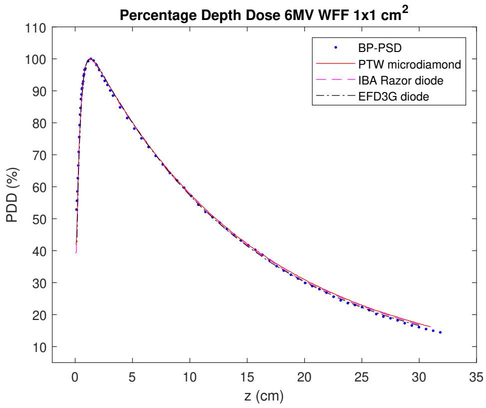

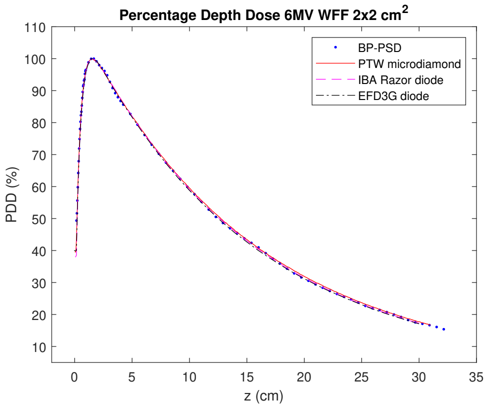

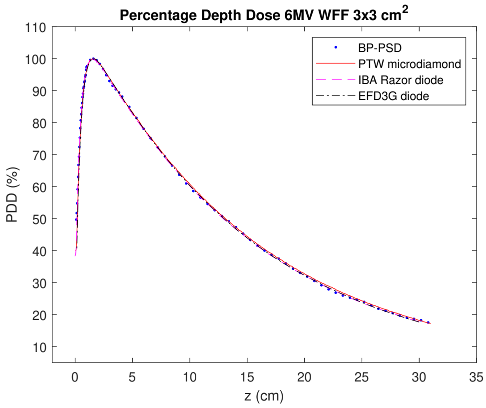

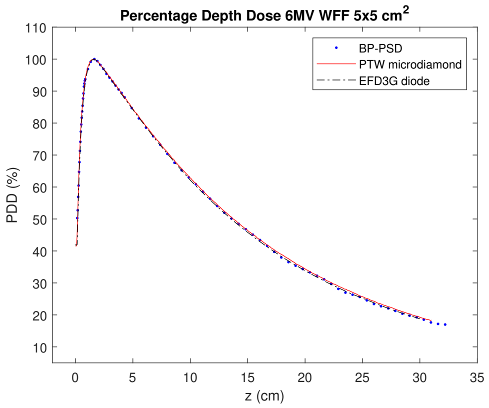
Percentage Depth Dose 6MV WFF 5x5 cm^2
BP-PSD
PTW microdiamond
EFD3G diode
PDD (%)
z (cm)
110
100
90
80
70
60
50
40
30
20
10
0
5
10
15
20
25
30
35

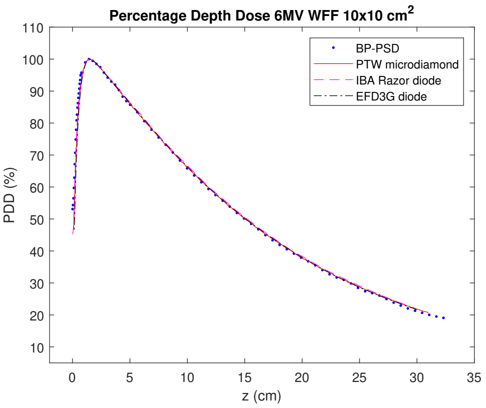
Percentage Depth Dose 6MV WFF 10x10 cm^2
BP-PSD
PTW microdiamond
IBA Razor diode
EFD3G diode
PDD (%)
z (cm)
110
100
90
80
70
60
50
40
30
20
10
0
5
10
15
20
25
30
35

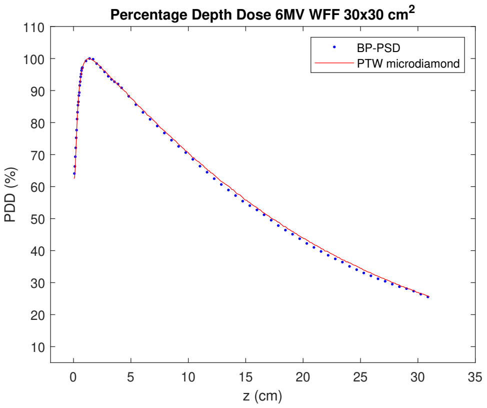
Percentage Depth Dose 6MV WFF 30x30 cm^2
BP-PSD
PTW microdiamond
PDD (%)
z (cm)
110
100
90
80
70
60
50
40
30
20
10
0
5
10
15
20
25
30
35

PDD 6 MV FFF

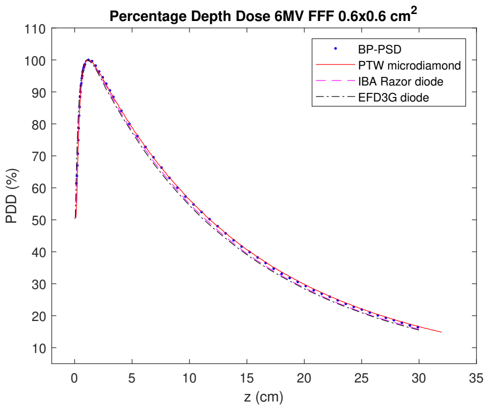
Percentage Depth Dose 6MV FFF 0.6x0.6 cm^2
BP-PSD
PTW microdiamond
IBA Razor diode
EFD3G diode
PDD (%)
z (cm)
110
100
90
80
70
60
50
40
30
20
10
0
5
10
15
20
25
30
35

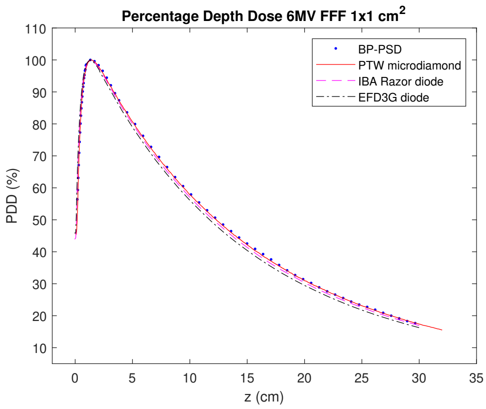
Percentage Depth Dose 6MV FFF 1x1 cm^2
BP-PSD
PTW microdiamond
IBA Razor diode
EFD3G diode
PDD (%)
z (cm)
110
100
90
80
70
60
50
40
30
20
10
0
5
10
15
20
25
30
35

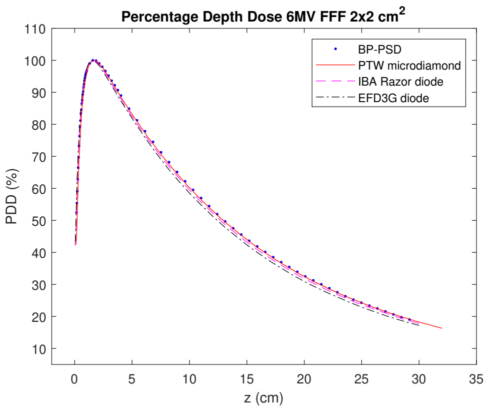
Percentage Depth Dose 6MV FFF 2x2 cm^2
BP-PSD
PTW microdiamond
IBA Razor diode
EFD3G diode
PDD (%)
z (cm)
110
100
90
80
70
60
50
40
30
20
10
0
5
10
15
20
25
30
35

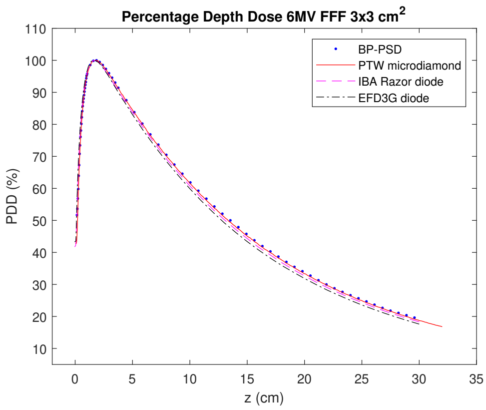
Percentage Depth Dose 6MV FFF 3x3 cm^2
BP-PSD
PTW microdiamond
IBA Razor diode
EFD3G diode
PDD (%)
z (cm)
110
100
90
80
70
60
50
40
30
20
10
0
5
10
15
20
25
30
35

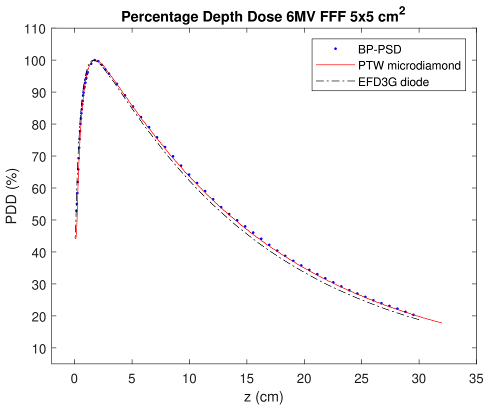
Percentage Depth Dose 6MV FFF 5x5 cm^2
BP-PSD
PTW microdiamond
EFD3G diode
PDD (%)
z (cm)
110
100
90
80
70
60
50
40
30
20
10
0
5
10
15
20
25
30
35

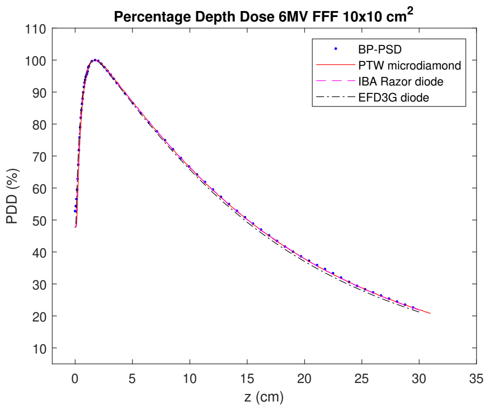
Percentage Depth Dose 6MV FFF 10x10 cm^2
BP-PSD
PTW microdiamond
IBA Razor diode
EFD3G diode
PDD (%)
z (cm)
110
100
90
80
70
60
50
40
30
20
10
0
5
10
15
20
25
30
35

OAR 6 MV WFF

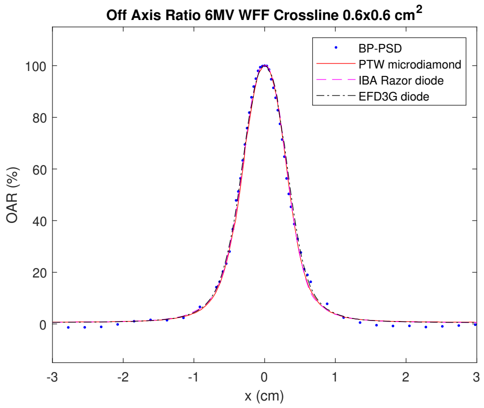
Off Axis Ratio 6MV WFF Crossline 0.6x0.6 cm^2

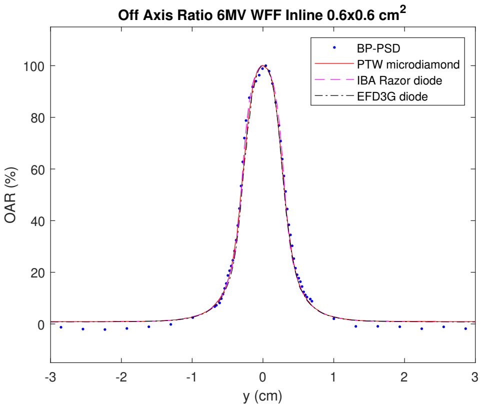
Off Axis Ratio 6MV WFF Inline 0.6x0.6 cm^2

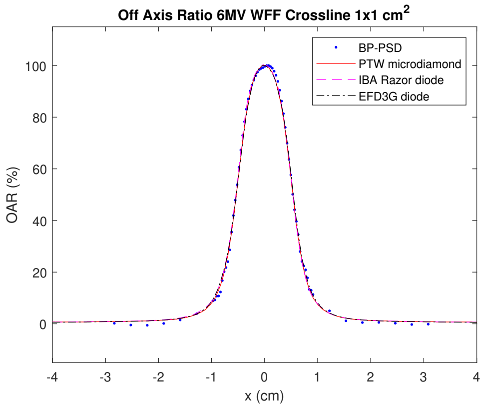
Off Axis Ratio 6MV WFF Crossline 1x1 cm^2

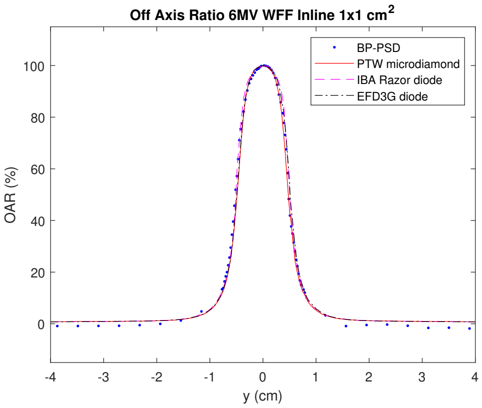
Off Axis Ratio 6MV WFF Inline 1x1 cm^2

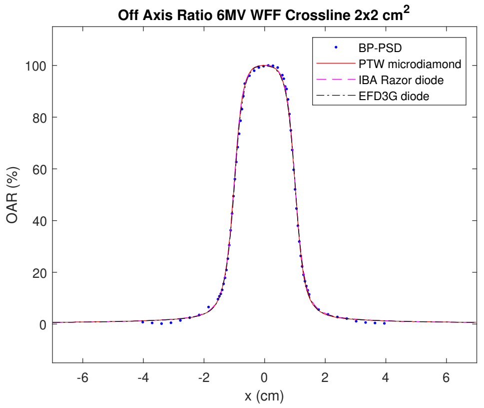
Off Axis Ratio 6MV WFF Crossline 2x2 cm^2

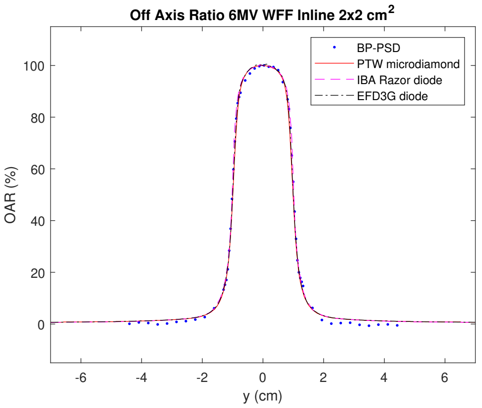
Off Axis Ratio 6MV WFF Inline 2x2 cm^2

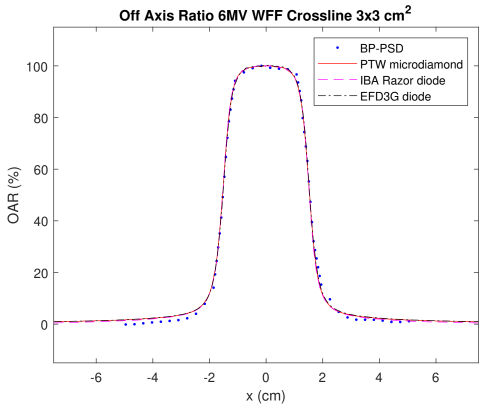
Off Axis Ratio 6MV WFF Crossline 3x3 cm^2
BP-PSD
PTW microdiamond
IBA Razor diode
EFD3G diode
OAR (%)
x (cm)
0
20
40
60
80
100
-6
-4
-2
0
2
4
6

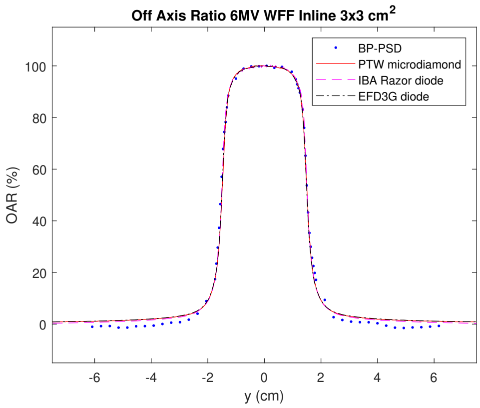
Off Axis Ratio 6MV WFF Inline 3x3 cm^2
BP-PSD
PTW microdiamond
IBA Razor diode
EFD3G diode
OAR (%)
y (cm)
0
20
40
60
80
100
-6
-4
-2
0
2
4
6

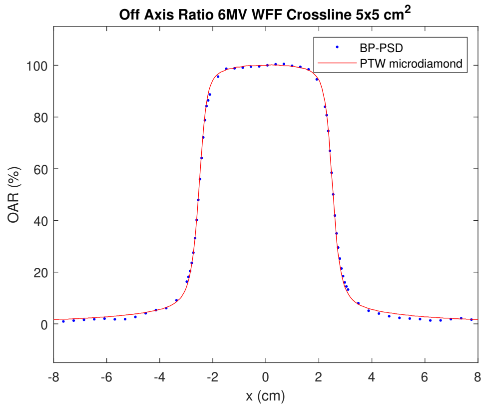
Off Axis Ratio 6MV WFF Crossline 5x5 cm^2
BP-PSD
PTW microdiamond
OAR (%)
x (cm)
0
20
40
60
80
100
-8
-6
-4
-2
0
2
4
6
8

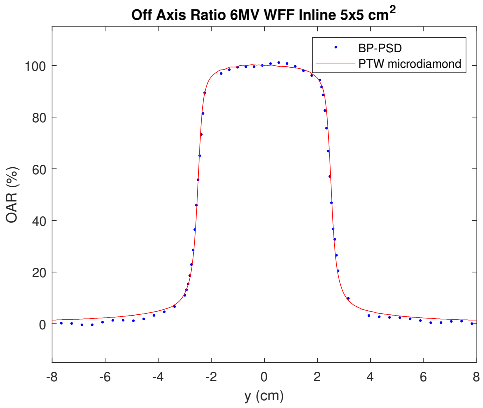
Off Axis Ratio 6MV WFF Inline 5x5 cm^2
BP-PSD
PTW microdiamond
OAR (%)
y (cm)
0
20
40
60
80
100
-8
-6
-4
-2
0
2
4
6
8

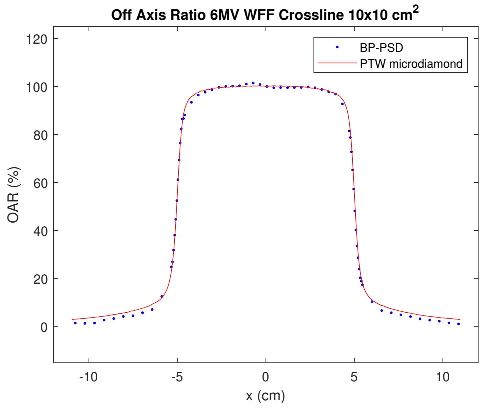
Off Axis Ratio 6MV WFF Crossline 10x10 cm^2
BP-PSD
PTW microdiamond
OAR (%)
x (cm)
0
20
40
60
80
100
120
-10
-5
0
5
10

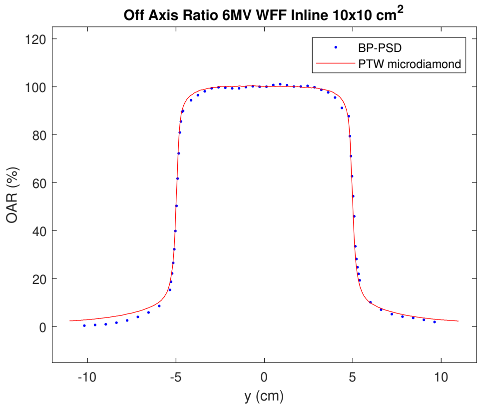
Off Axis Ratio 6MV WFF Inline 10x10 cm^2
BP-PSD
PTW microdiamond
OAR (%)
y (cm)
0
20
40
60
80
100
120
-10
-5
0
5
10

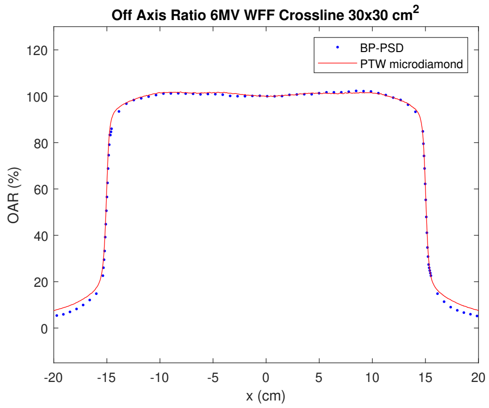
Off Axis Ratio 6MV WFF Crossline 30x30 cm^2
BP-PSD
PTW microdiamond
OAR (%)
x (cm)
0
20
40
60
80
100
120
-20
-15
-10
-5
0
5
10
15
20

OAR 6 MV FFF

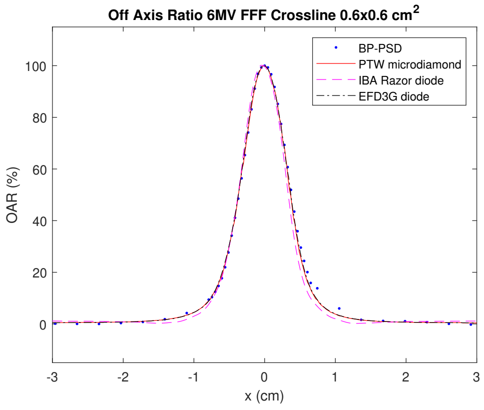

Off Axis Ratio 6MV FFF Crossline 0.6x0.6 cm^2

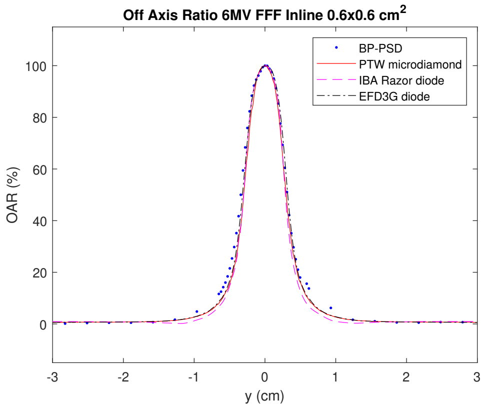

Off Axis Ratio 6MV FFF Inline 0.6x0.6 cm^2

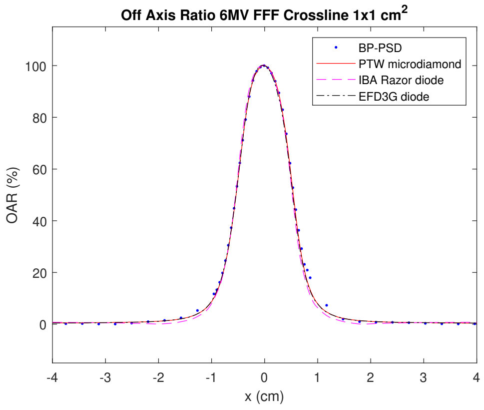

Off Axis Ratio 6MV FFF Crossline 1x1 cm^2

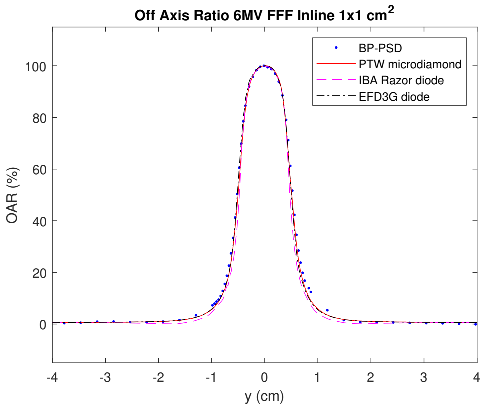

Off Axis Ratio 6MV FFF Inline 1x1 cm^2

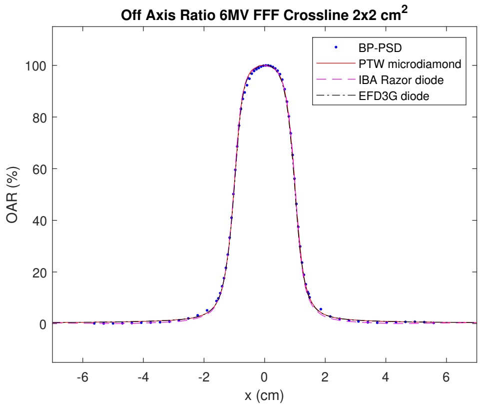

Off Axis Ratio 6MV FFF Crossline 2x2 cm^2

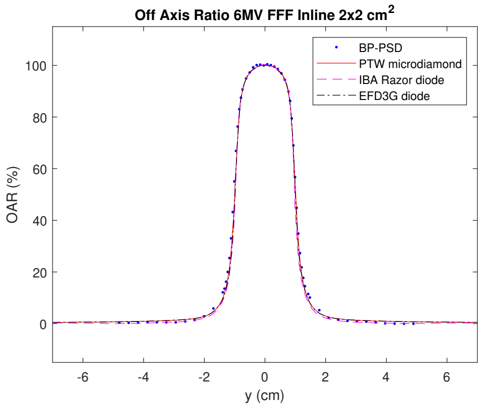

Off Axis Ratio 6MV FFF Inline 2x2 cm^2

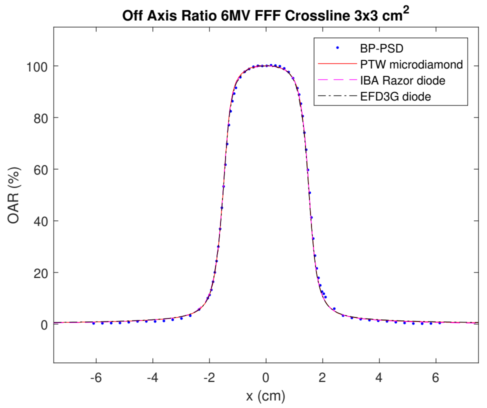
Off Axis Ratio 6MV FFF Crossline 3x3 cm^2

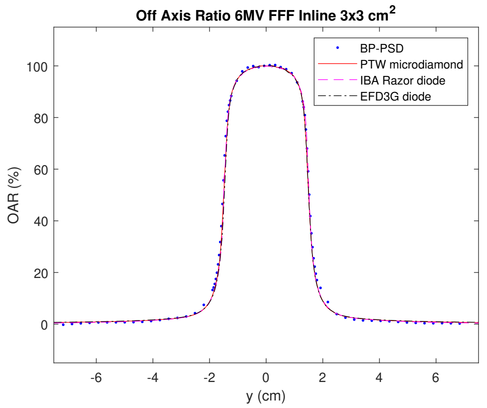
Off Axis Ratio 6MV FFF Inline 3x3 cm^2

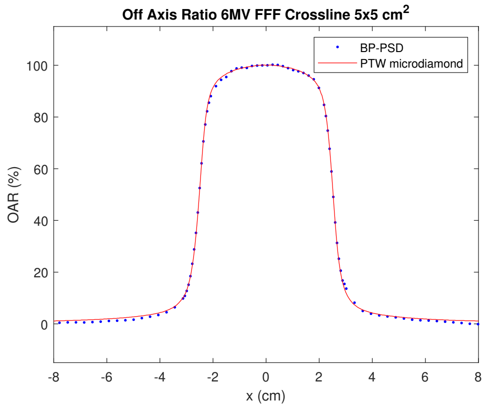
Off Axis Ratio 6MV FFF Crossline 5x5 cm^2

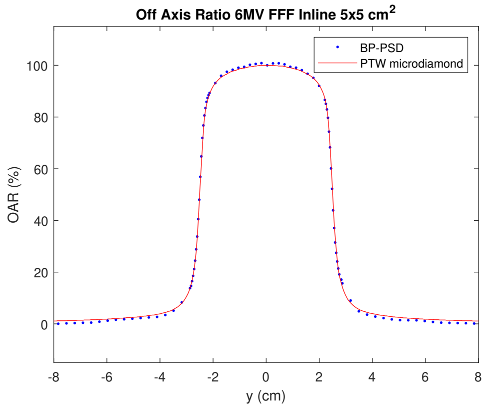
Off Axis Ratio 6MV FFF Inline 5x5 cm^2

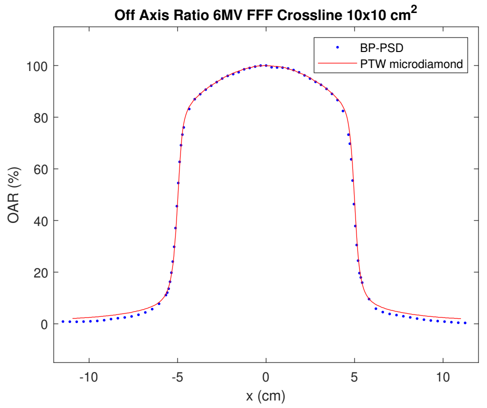
Off Axis Ratio 6MV FFF Crossline 10x10 cm^2

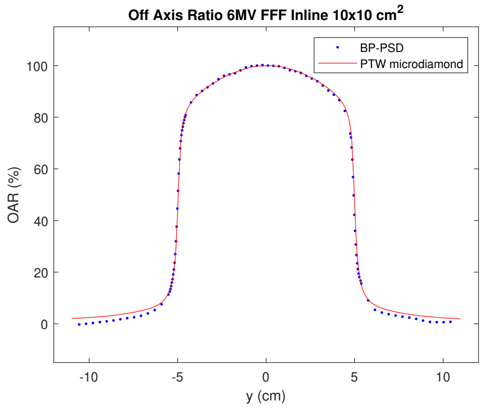
Off Axis Ratio 6MV FFF Inline 10x10 cm^2

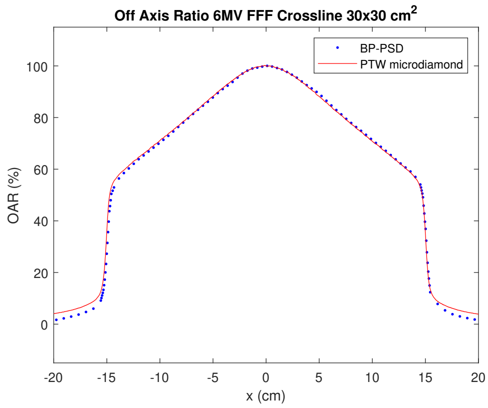
Off Axis Ratio 6MV FFF Crossline 30x30 cm^2

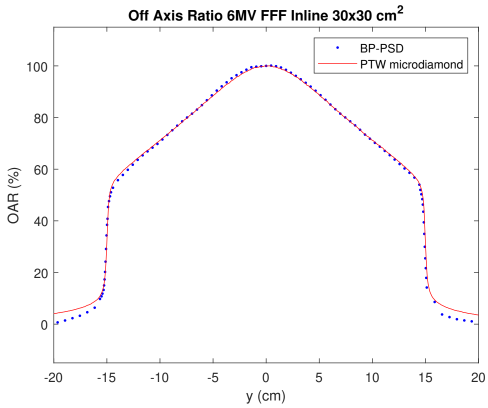
Off Axis Ratio 6MV FFF Inline 30x30 cm^2

Bibliography

[1] Ganesh Narayanasamy, Daniel Saenz, Wilbert Cruz, Chul S Ha, Niko Papanikolaou, and Sotirios Stathakis. Commissioning an elekta versa hd linear accelerator. *Journal of applied clinical medical physics*, 17(1):179–191, 2016.

[2] International Atomic Energy Agency. Absorbed dose determination in external beam radiotherapy: an international code of practice for dosimetry based on standards of absorbed dose to water. Technical Report TRS-398, IAEA, Vienna, 2000. Technical Reports Series No. 398.

[3] Attia Gul, Shigekazu Fukuda, Hideyuki Mizuno, Nakaji Taku, M Basim Kakakhel, and Sikander M Mirza. Feasibility study of using stereotactic field diode for field output factors measurement and evaluating three new detectors for small field relative dosimetry of 6 and 10 mv photon beams. *Journal of Applied Clinical Medical Physics*, 21(11):23–36, 2020.

[4] Antonella Fogliata, Antonella Stravato, Marco Pelizzoli, Francesco La Fauci, Pasqualina Gallo, Andrea Bresolin, Luca Cozzi, and Giacomo Reggiori. Small elongated mlc fields: Novel equivalent square field formula and output factors. *Medical Physics*, 2025.

[5] International Atomic Energy Agency. Dosimetry of small static fields used in external beam radiotherapy: an international code of practice for reference and relative dose determination. Technical Report TRS-483, IAEA, Vienna, 2017. Technical Reports Series No. 483.

[6] Andrew N McGrath, Samane Golmakani, and Timothy J Williams. Determination of correction factors in small mlc-defined fields for the razor and microsilicon diode detectors and evaluation of the suitability of the iaea trs-483 protocol for multiple detectors. *Journal of Applied Clinical Medical Physics*, 23(7):e13657, 2022.

[7] Božidar Casar, Eduard Gershkevitsh, Ignasi Mendez, Slaven Jurković, and M Saiful Huq. A novel method for the determination of field output factors and output correction factors for small static fields for six diodes and a microdiamond detector in megavoltage photon beams. *Medical physics*, 46(2):944–963, 2019.

[8] Paul ZY Liu, Giacomo Reggiori, Francesca Lobefalo, Pietro Mancosu, Stefano Tomatis, David R McKenzie, and Natalka Suchowerska. Small field correction factors for the iba razor. *Physica Medica*, 32(8):1025–1029, 2016.

[9] PTW Freiburg GmbH. Ptw dosimetry – global market leader in dosimetry solutions for radiation therapy, diagnostic radiology, metrology and radiation monitoring. `https://www.ptwdosimetry.com/`, 2025.

[10] IBA Dosimetry. Iba dosimetry – innovative quality assurance solutions for radiation therapy and medical imaging. `https://www.iba-dosimetry.com/`, 2025.

[11] Indra J Das, Jooyoung J Sohn, Sara N Lim, Bishwambhar Sengupta, Marcos Feijoo, and Poonam Yadav. Characteristics of a plastic scintillation detector in photon beam dosimetry. *Journal of Applied Clinical Medical Physics*, 25(1):e14209, 2024.

[12] Carlos Ferrer, Concepción Huertas, David García, and Moisés Sáez. Dosimetric characterization of a novel commercial plastic scintillation detector with an mr-linac. *Medical Physics*, 50(4):2525–2539, 2023.

[13] AIRC Foundation for Cancer Research. Official airc website. `https://www.airc.it/`, 2025.

[14] Varian Medical Systems. Official varian website. `https://www.varian.com/`, 2025.

[15] Elekta AB. Official elekta website. `https://www.elekta.com/`, 2025.

[16] Elena Pierpaoli. Commissioning e dosimetria clinica di un acceleratore synergy agility per trattamenti vmat. Master's thesis, Università di Pisa, Pisa, Italia, 2013. Tesi di specializzazione in Fisica Medica, A.A. 2012/2013.

[17] Ying Xiao, Stephen F Kry, Richard Popple, Ellen Yorke, Niko Papanikolaou, Sotirios Stathakis, Ping Xia, Saiful Huq, John Bayouth, James Galvin, et al. Flattening filter-free accelerators: a report from the aapm therapy emerging technology assessment work group. *Journal of applied clinical medical physics*, 16(3):12–29, 2015.

[18] Raffaele Fedele Laitano. *Fondamenti di dosimetria delle radiazioni ionizzanti.* ENEA, Roma, 4 edition, 2015. Quarta edizione.

[19] Saeed Ahmad Buzdar, Muhammad Afzal Rao, and Aalia Nazir. An analysis of depth dose characteristics of photon in water. *Journal of Ayub Medical College Abbottabad*, 21(4):41–45, 2009.

[20] Xiao-Jun Li, Yan-Cheng Ye, Yan-Shan Zhang, and Jia-Ming Wu. Empirical modeling of the percent depth dose for megavoltage photon beams. *Plos one*, 17(1):e0261042, 2022.

[21] Giacomo Reggiori, Pietro Mancosu, Natalka Suchowerska, Francesca Lobefalo, Antonella Stravato, Stefano Tomatis, and Marta Scorsetti. Characterization of a new unshielded diode for small field dosimetry under flattening filter free beams. *Physica Medica*, 32(2):408–413, 2016.

[22] IBA Dosimetry GmbH. *Blue Phantom2 User's Guide, Version 6*. IBA Dosimetry, Schwarzenbruck, Germany, 2013. Document number: PW-04-002-510-003 06.

[23] Ivan Veronese, Norberto Chiodini, Simone Cialdi, Eduardo d'Ippolito, Mauro Fasoli, Salvatore Gallo, Stefano La Torre, Eleonora Mones, Anna Vedda, and Gianfranco Loi. Real-time dosimetry with yb-doped silica optical fibres. *Physics in Medicine & Biology*, 62(10):4218, 2017.

[24] Paulina E Galavis, Lei Hu, Shannon Holmes, and Indra J Das. Characterization of the plastic scintillation detector exradin w2 for small field dosimetry. *Medical physics*, 46(5):2468–2476, 2019.

[25] Marco Marinelli, G Prestopino, C Verona, and G Verona-Rinati. Experimental determination of the ptw 60019 microdiamond dosimeter active area and volume. *Medical physics*, 43(9):5205–5212, 2016.

[26] IBA Dosimetry. *High Performance Diode Detector for Small Field Dosimetry in RT: RAZOR Detector*, 2014. Technical Flyer, Rev.1-1014.

[27] Min-Geon Choi, Martin Law, Do-Kun Yoon, Mikoto Tamura, Kenji Matsumoto, Masakazu Otsuka, Moo-Sub Kim, Shih-Kien Djeng, Hajime Monzen, and Tae Suk Suh. Simplified sigmoidal curve fitting for a 6 mv fff photon beam of the halcyon to determine the field size for beam commissioning and quality assurance. *Radiation Oncology*, 15:1–9, 2020.

[28] Saba Hussain. Commissioning of versa hd linear accelerator for ff and fff beams. evaluation of the performances of various detectors in relative small field dosimetry. Master's thesis, University of Trieste, Trieste, Italy, 2020. Master of advanced studies in Medical Physics.

Acknowledgments

Vorrei ringraziare tutte le persone a cui devo la realizzazione di questa tesi.
Ringrazio la professoressa Laura De Nardo dell'Università di Padova per avermi permesso l'entrata in tesi, e la dottoressa Sonia Reccanello direttrice della UOC di Fisica Sanitaria dell'Ospedale dell'Angelo per avermi fornito questa opportunità di tirocinio nel mondo della fisica medica.
Ringrazio tutta la Fisica Sanitaria di Mestre, in particolare Mariaconcetta Longo, per avermi seguito pazientemente e affiancato lungo tutto il periodo di tirocinio, mostrandosi sempre disponibile e accogliente; Marina Piovesan, per avermi aiutato durante le misurazioni e fornito preziosi consigli durante l'analisi dati; ma anche Lara Gallo, Francesco Guerriero, Serena Cargnel, Luca Binotto, Simonetta Salviato e Marco Brollo.
Un grazie anche a tutti i tecnici della radioterapia dell'Ospedale dell'Angelo di Mestre, con un ringraziamento speciale a Stefano Bellato e Patrizia Pitteri, con cui ho condiviso l'ufficio durante il periodo di tirocinio, che mi hanno sempre supportato e saputo strappare una risata anche nei momenti più duri.

Ringrazio la mia famiglia per essermi stata di supporto durante tutto questo periodo, e tutti i miei amici che mi hanno regalato molti momenti di spensieratezza.
In particolare ringrazio la mia fidanzata Gaia, che mi ha sostenuto e rincuorato in ogni momento.

Ringrazio infine la mia Staff scout del branco Chiaro di Luna, per tutto il supporto e la grinta che sono riusciti a infondermi, permettendomi di fare ciò che in gergo chiamiamo "del nostro meglio".